Reduced graphene oxide supported cobalt catalysts for hydroformylation and Fischer-Tropsch synthesis

by

Jianli Chang

submitted in accordance with the requirements for the degree of

Doctor of Philosophy

in the subject

Science, Engineering and Technology

at

UNIVERSITY OF SOUTH AFRICA

SUPERVISOR: Prof. Xinying Liu

CO-SUPERVISOR: Prof. Diane Hildebrandt
Prof. Yali Yao

December 2021

DECLARATION

Name: Jianli Chang

Student number: 57588686

Degree: PhD Philosophy

Exact wording of the title of the thesis as it appears on the electronic copy submitted for examination:

Reduced graphene oxide supported cobalt catalysts for hydroformylation and Fischer-Tropsch synthesis

I declare that the above thesis is my own work and that all the sources that I have used or quoted have been indicated and acknowledged by means of complete references.

I further declare that I submitted the thesis to originality checking software and that it falls within the accepted requirements for originality.

I further declare that I have not previously submitted this work, or part of it, for examination at Unisa for another qualification or at any other higher education institution.

SIGNATURE DATE

Abstract

Reduced graphene oxide (RGO) supported cobalt based catalysts with or without rhodium promotion, Rh-Co/RGO (RCG) and Co/RGO (CG), were successfully synthesized and evaluated in both Fischer-Tropsch synthesis (FTS) and ethene hydroformylation (EH).

The morphology, particle size and reducibility were different for the CG and RCG catalysts. (1) With the fresh catalysts, after calcination, CoO nanoparticles were present in the CG catalyst, while CoO nanorods were formed in the Rh promoted RCG catalyst. (2) With H_2 reduction, the reducibility of RCG was much higher than with the CG catalyst. (3) When exposing both the catalysts in syngas or syngas co-fed with ethene, a multi-phase of Co-Co_2C (or CoO) with smaller nanoparticles were presented in spent CG, while a pure Co_2C with a larger flat plane structure was formed in spent RCG. It was concluded that the small amount of Rh changed the interaction between the cobalt species and RGO, which enhanced the density of Co_2C on the surface of RGO during the FTS and EH reactions. The catalyst with a Co-Co_2C phase exhibited low FT activity with mainly short chain hydrocarbons and oxygenates. However, the catalyst with the Rh-Co_2C phase was completely inactive for FTS. Co_2C/RGO derived from CoO/RGO was highly active for heterogeneous EH and offers potential for use in industrial hydroformylation processes, especially with the catalyst promoted with Rh. It was concluded that Co_2C could suppress the CO from attending the chain growth reaction, while it promoted the CO insertion reaction to form oxygenates.

As the RCG catalyst showed outstanding performance for heterogeneous EH, optimization of reaction conditions was carried out. The influence of the feedgas ratio, pressure, space velocity and temperature on the EH over a Rh-Co/RGO catalyst was investigated in a tubular fixed bed reactor (TFBR). A higher CO partial pressure and a lower H_2 partial pressure with a temperature range of 210 °C to 230 °C increased the selectivity of the C_3 oxygenates, and decreased the selectivity of the C_2H_6 (the main by-product of C_2H_4 hydrogenation).

The mechanisms of hydroformylation and chain growth reaction for the RCG catalyst were studied. The potential reaction pathways are discussed based on a comparison of the changes in the product spectrum at different reaction temperature rates (140-290 °C). The C-C bond formed between CO and C_2H_4 was assumed to be the fastest elementary step, and it may be even faster than C-H bond formation. C_2H_4 induced the reaction of CO and C_2H_4 to form C-C coupling with an intermediate of $*C_2H_4CO$, which could further react with H_2 to form oxygenates and hydrocarbons. When the reaction temperature was higher than 210 °C, CO could induce the formation of ethylidyne ($\equiv C\text{-}CH_3$), which was a very important intermediate that triggered the chain growth reaction to form normal FT products. This work is of guiding the design of the heterogeneous catalysts for conversion of syngas to oxygenates by combining the FTS reaction and the olefin hydroformylation reaction.

Keywords: Reduced graphene oxide, Fischer-Tropsch synthesis, hydroformylation, cobalt carbide, oxygenate, syngas conversion, ethylidyne, CO insertion

Okungaqondakali (Abstract in Zulu)

Ama-catalyst asekelwe ku-graphene oxide (RGO) asekelwe ku-cobalt noma ngaphandle kokukhuthazwa kwe-rhodium, i-Rh-Co/RGO (RCG) ne-Co/RGO (CG), ahlanganiswe ngempumelelo futhi ahlolwa kukho kokubili i-Fischer-Tropsch synthesis (FTS) ne-ethene hydroformylation.

I-morphology, usayizi wezinhlayiya kanye nokuncipha kwe-reducibility kwakuhlukile kuma-catalysts e-CG kanye ne-RCG: (1) kuma-catalysts amasha ngemva kokubala, ama-nanoparticles e-CoO spherical anikezwe ku-catalyst ye-CG, kuyilapho ama-nanorods e-CoO akhiwa ku-Rh ekhuthaza i-RCG catalyst; (2) ngokunciphisa kwe-H_2, ukunciphisa kwe-RCG kwakuphakeme kakhulu kunalokho kwe-CG catalyst; (3) ukuveza womabili ama-catalysts ku-syngas noma kuma-syngas e-co-feeding ne-ethene, izigaba eziningi ze-Co-Co_2C (noma i-CoO) ezinama-nanoparticles amancane zethulwe ku-CG yokuchitha, kuyilapho i-Co_2C ehlanzekile enesakhiwo esikhulu sendiza eyisicaba. yakhelwe ekusetshenzisweni kwe-RCG. Kwaphethwa ngokuthi inani elincane le-Rh lishintshe ukusebenzisana phakathi kwezinhlobo ze-cobalt ne-RGO, okuthuthukise ukuminyana kwe-Co_2C ebusweni be-RGO ngesikhathi se-FTS kanye nokusabela kwe-ethene hydroformylation. I-catalyst enesigaba se-Co-Co_2C ibonise umsebenzi ophansi we-FT onama-hydrocarbon amaketango amafushane kanye nama-oxygen. Nokho, i-catalyst enesigaba se-Rh-Co_2C ayisebenzi ngokuphelele ku-FTS. Ngaphezu kwalokho, i-Co_2C/RGO ethathwe ku-CoO/RGO ibisebenza kakhulu ku-ethene hydroformylation ehlukahlukene futhi inikeza amathuba okusetshenziswa ezinqubweni ze-industrial hydroformylation, ikakhulukazi i-catalyst ekhuthazwa nge-Rh. Kwaphethwa ngokuthi i-Co_2C ingacindezela i-CO ekuhambeleni ukusabela kokukhula kweketango, kuyilapho ikhuthaza ukusabela kokufakwa kwe-CO ukwenza ama-oxygen.

Njengoba i-RCG catalyst ibonise ukusebenza okuvelele kwe-ethene hydroformylation ehlukahlukene, ukuthuthukiswa kwezimo zokusabela kwenziwa. Umthelela wesilinganiso se-feedgas, ingcindezi, isivinini sesikhala nezinga lokushisa ku-ethene hydroformylation phezu kwe-Rh-Co/RGO catalyst iye yaphenywa ku-rector yombhede ongaguquki weshubhu. Ukucindezela kwengxenye ye-CO

ephakeme kanye nokucindezela okuncane kwe-H_2 okuphansi ngebanga lokushisa elingu- 210°C, 230 °C kungase kukhulise ukukhethwa kwama-oxygen e-C_3, futhi kwehlise ukukhethwa kwe-C_2H_6 (okuyinhloko ngomkhiqizo ovela ku-C_2H_4 hydrogenation) .

Izindlela ze-hydroformylation kanye ne-chain growth reaction ye-RCG catalyst yafundwa. Izindlela zokusabela ezingaba khona kwakuxoxiwe ngazo ngokusekelwe ekuqhathaniseni izinguquko ze-spectrum yomkhiqizo emazingeni okushisa ahlukene okusabela (140-290 °C). Ukwakhiwa kwebhondi ye-C-C phakathi kwe-CO ne-C_2H_4 kwakuyisinyathelo sokuqala esilula ukwenzeka kulesi simiso esilula nakakhulu kunokwakheka kwebhondi ye-C-H. I-C_2H_4 iyenge ukusabela kwe-CO ne-C_2H_4 ukuze kwakheke i-C-C ukuhlangana nokuphakathi kwe-*C_2H_4CO, okungase kuqhubeke kusabela nge-H_2 ukuze kwakhe ama-oxygen nama-hydrocarbon. Lapho izinga lokushisa lokusabela liphakeme kune-210 ℃, i-CO ingabangela ukwakheka kwe-ethylidyne (≡C-CH_3), okwakuyindawo ebaluleke kakhulu ephakathi eyabangela ukusabela kokukhula kweketango ukuze kwakhiwe imikhiqizo evamile ye-FT. Lo msebenzi ungowokuqondisa ukwakheka kwama-catalysts ahlukahlukene okuguqulwa kwama-syngas abe ama-oxygen ngokuhlanganisa ukusabela kwe-FTS kanye nokusabela kwe-olefin hydroformylation.

Amagama angukhiye: Yehlisiwe i-graphene oxide, i-Fischer-Tropsch synthesis, i-hydroformylation, i-cobalt carbide, i-oxygen, ukuguqulwa kwe-syngas, i-ethylidyne, ukufakwa kwe-CO

ACKNOWLEDGEMENTS

I would like to show my gratefulness to the following people and institutions for their help and support which make me complete this thesis.

First I would like to express my gratitude to my supervisors, Professor Xinying Liu, Professor Diane Hildebrandt and Professor Yali Yao. It is their guidance and support that inspire me to fulfil the study. It is a privilege for me to work under their supervision.

I want to give thanks to the staff at IDEAS for their assistance and caring. Thanks to Dr Xiaojun Lu, Dr Joshua Gorimbo and Dr Mahluli Moyo for their management of our laboratory, advice and discussions. I also want to thanks to Mr. Mbatha Mpumelelo and Mr Mandla Mngomezulu for technical support in the laboratory. I am grateful to our group members for providing a stimulating and fun environment in which to learn and grow.

I really appreciate Juliet Gillies editing my thesis and papers.

I would like to thank South Africa National Research Foundation (NRF) and the University of the South Africa for financial support and facilities.

Finally, I wish to thank my family who have always been supporting and encouraging me. Especially, I feel very joyful that my lovely daughter was born and came to me in 2020.

List of Publications and Presentations

Publications:

1) J. Chang, Y. Zhang, X. Lu, Y. Yao, X. Liu, D. Hildebrandt, Insight into the role of Co_2C supported on reduced graphene oxide in Fischer-Tropsch synthesis and ethene hydroformylation, Appl. Catal. A Gen. 614 (2021) 118050. https://doi.org/https://doi.org/10.1016/j.apcata.2021.118050.
2) Y. Zhang, M. Tshwaku, Y. Yao, J. Chang, X. Lu, X. Liu, D. Hildebrandt, Reaction of ethylene over a typical Fischer-Tropsch synthesis Co/TiO_2 catalyst, Eng. Reports. 2 (2020) e12232. https://doi.org/https://doi.org/10.1002/eng2.12232.
3) Y. Zhang, Y. Yao, J. Chang, J. Gorimbo, X. Liu, D. Hildebrandt, The interaction of CO, H2 and ethylene over a typical cobalt-based Fischer-Tropsch synthesis catalyst, Appl. Catal. A Gen. 614 (2021) 118024. https://doi.org/https://doi.org/10.1016/j.apcata.2021.118024.
4) Y. Zhang, Y. Yao, J. Shen, J. Chang, J. Gorimbo, X. Liu, D. Hildebrandt, Effect of ethylene co-feeding in Fischer-Tropsch synthesis: A study of reaction equilibrium and competition, Fuel. 302 (2021) 121146. https://doi.org/10.1016/j.fuel.2021.121146.
5) Y. Zhang, Y. Yao, J. Chang, X. Lu, X. Liu, D. Hildebrandt, Fischer–Tropsch synthesis with ethene co-feeding: Experimental evidence of the CO-insertion mechanism at low temperature, AIChE J. 66 (2020) e17029. https://doi.org/https://doi.org/10.1002/aic.17029.
6) J. Chang, Y. Zhang, Y. Yao, X. Liu, D. Hildebrandt, Rh/Co/rGO catalyst for heterogenous ethylene hydroformylation: Bimetallic species - support interaction. (Submitting to journal.)

International Conference:

1) 3rd International Conference on Catalysis and Chemical Engineering, 2019 (CCE-2019)

Poster presentation: Cobalt supported on reduced graphene oxide as catalyst for the hydroformylation of ethylene with syngas.

National conference:

1) Catalysis Society of South Africa (CATSA) 2015:

Flash presentation (oral): Phase-adjusted synthesis of homogeneous nickel based graphene composites and electrochemical catalysis as counter electrode.

2) CATSA 2016:

Poster presentation: Application of titanium dioxide parcelled with graphene in dye-sensitized solar cells on counter electrodes.

3) CATSA 2017:

Poster presentation: Cobalt supported on graphene as catalyst for the synthesis of higher alcohols from syngas.

4) CATSA 2018:

Oral presentation: Cobalt supported on reduced graphene oxide as catalyst for the hydroformylation of ethylene with syngas.

5) CATSA 2021:

Poster presentation: Rh/Co/rGO catalyst for heterogenous ethylene hydroformylation: Bimetallic species – support interaction.

CONTENTS

LIST OF FIGURES

LIST OF TABLES

LIST OF SCHEMES

ABBREVIATIONS AND ACRONYMS

α	chain growth probability
AC	activated carbon
ASF	Anderson-Schultz-Flory
CG	20%Co/RGO
DFT	Density functional theory
EDS	energy dispersive spectrometer
EH	ethene hydroformylation
FBR	fixed bed reactor
FID	flame ionization detector
FTO	Fischer-Tropsch to olefins
FTS	Fischer-Tropsch Synthesis
FWHM	full width at half maximum
g	gram
GC	gas chromatograph
g·cat	per gram catalyst
GHSV	gas hourly space velocity
H_2-TPR	hydrogen temperature programmed reduction
hcp	hexagonal close packed
ID	internal diameter
JCPDS	Joint Committee on Powder Diffraction Standards
MSI	metal-supported interactions
NTP	normal temperature and pressure
P	pressure
RGO	reduced graphene oxide
RCG	0.5%Rh-20%Co/RGO
SEM	scanning electron microscopy
SFT	syngas feed Fischer-Tropsch Synthesis

T	temperature
TCD	thermal conductivity detector
TEM	transmission electron microscope
TFBR	tubular fixed bed reactor
TPR	temperature-programmed reduction
UHP	ultra-high purity
Wn	weight fraction of hydrocarbon product containing n atoms
XRD	X-ray diffraction

Calculations:

$A_{x,gas}$	integrated area of the peak from GC detector corresponding to the component x in the analysed gas
$A_{x,cal}$	integrated area of the peak from GC detector corresponding to the component x in the calibration gas
$A_{y,cal}$	integrated area of the peak from GC detector corresponding to the reference component y in the calibration gas
F_{in}	total molar flow rate of the feed-gas, mmol/h
F_{out}	total molar flow rate of the reactor tail-gas, mmol/h
$F_{x,in}$	molar flow rate of component x in feed-gas, mmol/h
$F_{x,out}$	molar flow rate of component x in tail-gas, mmol/h
m_{cat}	mass of catalyst loaded into reactor
n	carbon number in products x
$P_{x,gas}\%$	molar percentage of component x in the analysed gas
$P_{x,cal}\%$	molar percentage of component x in the calibration gas
$P_{y,cal}\%$	molar percentage of component y in the calibration gas.
$P_{N_2,in}$	molar percentage of N_2 in the feed-gas
$P_{N_2,out}$	molar percentage of N_2 in the tail-gas
$P_{x,in}$	molar percentage of component x in feed-gas, mmol/h

$P_{x,out}$	molar percentage of component x in tail-gas, mmol/h
$RF_{x,y}$	relative response factor of component x in analysed gas based on the reference component y in calibration gas
r_x	reaction rate of component x
$S_{x,out}$	selectivity of product x based on converted CO, %
S_{other}	total selectivity of C_{5+} hydrocarbons and C_{6+} alcohols, %
$S_{Hydrocarbons}$	selectivity of hydrocarbons, %
$S_{Alcohols}$	the selectivity of alcohols, %
S_{x,C_2H_4}	selectivity of product x based on converted C_2H_4
$S_{x,carbon}$	selectivity of product x based on total converted carbon from CO and C_2H_4
x_{conv}	conversion of component x, %

Chapter 1: Introduction

1.1 Overall Introduction

Fischer-Tropsch synthesis (FTS) is a catalytic reaction that can produce synthetic hydrocarbon fuels and chemicals from syngas (CO and H_2) obtained via the gasification of any carbon-containing feedstock like coal, natural gas or biomass.[1] Hydroformylation is a reaction caused by the addition of CO and H_2 across a C=C double bond in olefins to form aldehyde, which was discovered by Otto Roelen in 1938 when co-feeding olefinic FTS products with CO and H_2 on cobalt catalysts heterogeneously.[2–5] Studies on the relationship between the FTS and hydroformylation reactions are scarce,[6–8] therefore, it is important to study the topic, which can aid to understanding the reaction mechanisms for FTS and hydroformylation and catalysis on the catalyst surface, as well as tuning reactions and product selectivity in syngas conversion.

Due to its unique properties, graphene has wide application in adsorption, sensors and catalysis.[9–11] Cobalt and rhodium have been applied to both FTS and hydroformylation.[12–15] However, much more research needs to be done on graphene-supported cobalt and cobalt-rhodium bimetallic catalysts for FTS and hydroformylation. In particular, there is a lack of research on the cobalt active species for each reaction, tuning products that vary from hydrocarbons to oxygenates and metal-support interaction.

1.2 Aims of the Study

Although both FTS and hydroformylation have been developed industrially for decades, more insight is required into the relationship between FTS and hydroformylation, including: changes in catalyst active sites; reaction regime shift from FTS to hydroformylation; mechanisms for FTS and hydroformylation. The heterogenization of hydroformylation has been attracting attention in an attempt to overcome the intrinsic drawbacks of the current homogeneous industrial process.

The aim of this thesis is to reveal the relationship between FTS and hydroformylation in terms of catalysis and mechanisms. Ethene hydroformylation (EH) was selected for comparison with FTS in this study and reduced graphene oxide (RGO) supported cobalt-based catalysts were prepared for FTS and EH. The optimization of reaction conditions for heterogeneous EH was also investigated.

1.3 Overview of the Thesis

Except for Chapter 2 - Literature Review and Chapter 3 - Experimental, each chapter was written in the style required for publication, i.e. abstract, introduction, experimental, discussion and conclusion. The outline of the thesis is as follows:

- In Chapter 2, a summary of the review of the literature regarding to FTS and EH is provided. Attention was paid to the catalyst active sites, the supports used in this study and the mechanisms involved.
- In Chapter 3, all the materials, instruments and procedures that were used to carry out the experiments are described in detail. The methodology for experimental data processing is also provided.
- Chapter 4 reports on the two catalysts - cobalt supported by RGO (CG) and Rh promoted cobalt supported by RGO (RCG) - that were used for both the FTS reaction and the EH reaction. Both catalysts were evaluated with a syngas and a syngas co-fed with ethene. The changes in the cobalt species and the effect on catalyst performance were investigated. The role of Co_2C and the metal support interaction are discussed
- Chapter 5 details the investigation into the metal-support interaction between cobalt and RGO. Cobalt supported by RGO (CG) and Rh-promoted cobalt supported by RGO (RCG) were tested for heterogeneous EH. With the addition of rhodium, the tuned metal-supported interactions (MSI) shows many differences in terms of: morphology of the nanoparticles; particle size; active phase of cobalt.
- Chapter 6 and 7 detail the study of the optimized reaction conditions of EH. The influence of feed-gas ratios on EH over a Rh-Co bimetallic catalyst supported by RGO was investigated and is reported on in Chapter 6. The investigation into the influence of pressure, space velocity and temperature on EH over a Rh-Co/RGO catalyst is reported on in Chapter 7.

- In Chapter 8, mechanisms and reaction pathways for both FTS and EH are proposed. The reaction of $CO/C_2H_4/H_2$ on a CO non-dissociation cobalt catalyst was carried out under FTS conditions. The CO direct dissociation mechanism and CO inversion mechanism are discussed to explain the reaction behavior. C-C band coupling and the formation of the ethylidene intermediate are also discussed.

References

[1] A.C. Vosloo, Fischer-Tropsch: A futuristic view, Fuel Process. Technol. 71 (2001) 149–155. https://doi.org/10.1016/S0378-3820(01)00143-6.

[2] O. Roelen, United states Patent Office 2327,066, (1943).

[3] B. Breit, Recent Advances in Alkene Hydroformylation, (2007) 139–172.

[4] K. Wiese, D. Obst, Hydroformylation, Catal. Carbonylation React. 18 (2006) 1–33. https://doi.org/10.1007/3418_015.

[5] R. Franke, D. Selent, A. Borner, Applied hydroformylation, Chem. Rev. 112 (2012) 5675–5732. https://doi.org/10.1021/cr3001803.

[6] G. Henrici-Olivé, S. Olivé, Hydroformylation and Fischer-Tropsch Reaction - Analogies and discrepancies, J. Mol. Catal. 3 (1978) 443–446.

[7] H. Schulz, Major and minor reactions in Fischer-Tropsch synthesis on cobalt catalysts, Top. Catal. 26 (2003) 73–85. https://doi.org/10.1023/B:TOCA.0000012988.86378.21.

[8] B.H. Davis, M.L. Occelli, Advances in Fischer-Tropsch Synthesis, Catalysts and Catalysis, 1st Edition, CRC Press, 2010. https://doi.org/https://doi.org/10.1201/9781420062571.

[9] J. Xu, R.S. Ruoff, H. Zhu, The physics and chemistry of graphene-on-surfaces, Chem. Soc. Rev. 46 (2017) 4417–4449. https://doi.org/10.1039/C7CS00256d.

[10] Y. Cheng, Y. Fan, Y. Pei, M. Qiao, Graphene-supported metal/metal oxide nanohybrids: Synthesis and applications in heterogeneous catalysis, Catal. Sci. Technol. 5 (2015) 3903–3916. https://doi.org/10.1039/C5CY00630A.

[11] V. Singh, D. Joung, L. Zhai, S. Das, S.I. Khondaker, S. Seal, Graphene based materials: Past, present and future, Prog. Mater. Sci. 56 (2011) 1178–1271. https://doi.org/10.1016/j.pmatsci.2011.03.003.

[12] Z. Yan, D.B. Bukur, D.W. Goodman, Silica-supported rhodium-cobalt catalysts for Fischer–Tropsch synthesis, 160 (2011) 39–43. https://doi.org/10.1016/j.cattod.2010.06.023.

[13] G. Jacobs, T.K. Das, Y. Zhang, J. Li, G. Racoillet, B.H. Davis, Fischer-Tropsch synthesis: Support, loading, and promoter effects on the reducibility of cobalt catalysts, Appl. Catal. A Gen. 233 (2002) 263–281. https://doi.org/10.1016/S0926-860X(02)00195-3.

[14] L. Huang, Y. Xu, G. Piao, A. Liu, Enhancement of olefin hydroformylation related to supported bimetallic Rh-Co clusters, Catal. Letters. 23 (1994) 87–95.

[15] N. Huang, B. Liu, X. Lan, T. Wang, Insights into the bimetallic effects of a RhCo catalyst for ethene hydroformylation: Experimental and DFT investigations, Ind. Eng. Chem. Res. 59 (2020) 18771–18780. https://doi.org/10.1021/acs.iecr.0c03437.

Chapter 2: Literature Review

2.1 Introduction to Fischer-Tropsch Synthesis and Hydroformylation

2.1.1 Fischer-Tropsch Synthesis

Since its discovery in Germany about 90 years ago, Fischer-Tropsch synthesis (FTS) has continued to attract the attention of researchers all over the world, as it is one of the key technologies for producing transportation fuel.[1,2] FTS is a catalytic reaction that can produce synthetic hydrocarbon fuels and chemicals from natural gas or syngas (CO and H_2) via gasification of any carbon-containing feedstock like coal or biomass.[3] Heterogeneous catalysts containing group VIII metals such as iron, cobalt, ruthenium and nickel, are used for FTS, with CO and H_2 being dissociated on the surface and converted to CH_x species to form long chain hydrocarbons.[4] Because of the cost and reaction performance, only cobalt- and iron-based catalysts have been applied in commercial FTS plants.[2,5–7] Cobalt-based catalysts are important for FTS to produce waxes with a high molecular weight that can subsequently be hydrocracked to lubricants and diesel fuel.[8] Therefore, the study of cobalt-based FTS catalysts is still a popular field in both academic and industrial research.[9] The topics of these studies include: active sites; the effect of particle size on activity and selectivity; support effects; the effect of promoters and the deactivation mechanism; regeneration.[5,8,10–15]

Although the concept of a stepwise chain growth process is generally accepted, the details of the FTS mechanism are still being debated [16,17] and the FTS mechanisms continue to receive attention.[18–24] The combination of surface science and co-feeding probe molecules with syngas such as H_2O, CO_2 and C_2H_4 makes it clear and helps with further understanding the FTS mechanisms.[25–27] Ethene is one of the most important probe molecules studied that keeps refreshing the cognition of FTS mechanisms.[28–35] The most important homogeneous industrial process is hydroformylation (also known as the OXO process). It was discovered by Otto Roelen in 1938 when co-feeding olefinic FTS products with CO and H_2 on cobalt catalysts heterogeneously.[36–38]

2.1.2 Hydroformylation

Hydroformylation is a reaction caused by the addition of CO and H_2 across a C=C double bond in olefins to form aldehyde.[37,39] Although it was discovered with a heterogeneous catalysis process,[36] it was found that high performance was achieved in a homogeneous system.[40] The aldehydes formed are useful products and important intermediates in the production of valuable products such as alcohols, carboxylic acids, amines and diols.[39] Hydroformylation is currently widely used in the fine chemical and pharmaceutical industries for the production of drugs, vitamins, herbicides and perfumes.[41]

The share of various products in the overall alkene hydroformylation capacity approximate the following: C_2 - 2%; C_3 - 70%; C_4 - 20%; >C_{12} - 8%.[42] The metals in the neighbourhood of rhodium on the periodic table are active for hydroformylation and a generally accepted order of activity is as follows: Rh >> Co > Ir, Ru > Os > Pt > Pd >> Fe > Ni.[38–40] Rhodium and cobalt are used as homogeneous complexes with the form $[HM(CO)_xL_y]$ in industrial process; except with some special applications, other metals are only studied in academic research due to their low activity.[38,39] The two main types of ligands are phosphanes PR_3 and phosphites $P(OR)_3$ (R = alkyl, aryl).[38] The influence of ligands and modified ligands on the regioselectivity (*n/iso* ratio), solvents, side reactions, kinetics and mechanisms, are the aspects most studied in homogeneous hydroformylation.[43,44] Several studies have also focused on price, and long-term stability and recycling of the ligands, in order to lower the overall cost of an industrial process.[38,39,45]

2.1.3 The relationship between FTS and hydroformylation

As mentioned, the reaction of $CO/H_2/C_2H_4$ is usually studied as ethene co-feeding FTS to investigate the mechanisms of FTS.[28–35] In a heterogeneous reaction system, hydroformylation is normally considered a secondary reaction of olefins that produces alcohols in FTS.[29,46–48] However, the relationship between FTS and hydroformylation is rarely reported on. The analogies and discrepancies between FTS and hydroformylation in terms of reaction mechanisms was reported in 1977.[49] The conclusion of the study was that insertion of a CO molecule into a metal-carbon bond and the formation of an acyl-metal species is a common step in both reactions.[49] The difference is that aldehyde was produced and immediately terminated from the cobalt complex without further chain

growth in hydroformylation, while in FTS the aldehydes remained on the surface of the cobalt catalyst and hydrogenated to participate in further chain growth.[49] It has been reported that with increasing pressure and decreasing temperature cobalt carbonyl complexes form metallic cobalt, which leads to the FTS regime shifting to the hydroformylation regime.[46,50]

The key difference between the FTS mechanism and hydroformylation is whether or not chain growth can be initiated.[49] Metallic cobalt is active for long chain hydrocarbon formation, while cobalt carbonyl complexes are active for hydroformylation and shut down chain growth and prevent long chain hydrocarbons forming.[46,50] Therefore, the questions that need to be addressed are: (1) Can transferring metallic cobalt to cobalt carbonyl complexes lead to a shift in the reaction regime from FTS to hydroformylation? (2) Are there other cobalt species that can also shut down the chain growth reaction? The answer to these questions lies in the conversion of syngas to mixed alcohols with different chain lengths, which involves both the FTS chain growth reaction and the hydroformylation reaction simultaneously.[48,51]

The catalysts used in the production of mixed alcohols include single metal species, bimetallic catalysts and even triple metals catalysts, such as Mo_2S, Mo_2C, Cu-Co, Rh-Fe, Pt-Fe, Cu-Zn-Al and Zn-Cr-K.[51–53] With cobalt-based catalysts, an interface of Co/Co_2C was reported to be active for the synthesis of oxygenates via FTS.[54–57] A concept of dual site or bi-function on Co/Co_2C was proposed and that metallic Co was active for CO dissociation and chain growth, while Co_2C was active for CO insertion to hydrocarbon to form oxygenates.[54] Furthermore, Co/Co_2C was active for 1-Hexene hydroformylation in a fixed-bed continuous-flow stainless microreactor; and the bi-function was reported as metallic Co was used for olefin adsorption and activation, while Co_2C was used for CO adsorption, activation and insertion.[58]

Therefore, it can be deduced that Co_2C plays a vital role in the formation of oxygenates in cobalt-based catalysts, which may possibly lead to a shift in the reaction regime from FTS to hydroformylation besides cobalt carbonyls complexes. The role of Co_2C in the formation of oxygenates is reviewed in the next section.

2.2 Role of Co_2C in syngas to hydrocarbons and oxygenates

There is some debate about certain aspects of cobalt carbide, such as its roles and effect on FTS. In 1939, it was proposed that the formation and reduction of cobalt carbide led to the formation of CH_2, which is the first step in FTS.[59] However, in 1948, it was reported that bulk cobalt carbide was neither an intermediate nor catalytically active for FTS, and that it severely suppressed FTS activity.[60] Therefore, it is crucial to understand the role of cobalt carbide in syngas conversion. The conclusions in the literature need to be analyzed and investigated in order to obtain a deeper understanding of cobalt carbide and to guide the experiments that are done.

2.2.1 Formation and stability of cobalt carbide

It seems that cobalt carbides are easier to form at a low H_2/CO ratio and lower temperature.[61,62] Claeys et al. [61] reported that cobalt carbide formation was inversely proportional to the H_2/CO ratio and the reaction temperature on a 20 wt% Co/Al_2O_3 catalyst promoted with 0.05 wt% platinum. The results reported by Lin et al. [62] indicated that Co_2C cannot be formed at an H_2/CO of 2, when testing 20 wt% cobalt/silicon dioxide (20%Co/SiO_2), because of the lower carbon diffusion rate compared to that of an iron catalyst. However, a low H_2/CO of 0.5 led to Co_2C formation, but required a high reaction temperature (>280 °C).[62]

The formation of cobalt carbide can be accelerated by some promoters. Pei et al. [63] studied the effect of alkali promoters on the formation of cobalt carbide using a mechanically mixed Co_3O_4 with alkali promoters. It was found that the formation of cobalt carbide could be significantly accelerated by the promoter Li due to the enhanced ability of the precursor to react with CO.[63] La_2O_3 can promote the formation of cobalt carbide on cobalt-based catalysts supported on activated carbon (AC) and Al_2O_3. [64] Du et al. [65] reported that the addition of CaO promoted the formation of hexagonal close-packed (hcp) metallic cobalt (Co-hcp) on a Co–CaO/AC catalyst, which was also prone to convert into Co_2C species. Singh et al. [66] reported that ZnO could act as a dual promoter by facilitating Co_2C formation and by modifying the resulting Co_2C. The Co_2C formed from the ZnO-promoted Co catalysts

displayed improved thermal stability and selectivity compared with similar Co_2C catalysts without Zn.[66]

It was reported that carbon supports promote the formation of cobalt carbide and also act as the carbon source to form cobalt carbide.[64,67,68] It has also been reported that AC supports promote carbide formation, whereas oxides supports, such as alumina, inhibit it.[64] Co_3O_4 supported by graphene oxide can be converted to Co_2C under a H_2/N_2 mixture at 200 °C, which indicates that graphene oxide was the carbon source for the formation of Co_2C.[67] Cobalt carbide can be formed during the activation of 15Co/AC catalysts by H_2, which proves that the AC was the carbon source for the formation of cobalt carbide.[68]

There is some debate about the stability of cobalt carbide under typical FTS conditions.[61,69] Claeys et al. reported that cobalt carbide is relatively stable at typical reaction conditions, but rapid decomposition into Co-hcp occurs in the treatment with hydrogen at above 150 °C[61]. Mohandas et al. reported that bulk cobalt carbide appears to be unstable under FTS conditions, especially at higher reaction temperatures.[69] Therefore, it seems that hydrogen and temperature significantly influence the stability of carbide under FTS conditions. Co_2C can be easily decomposed to metallic cobalt in an H_2 environment.[70,71] With hydrogen treatment, due to carbide formation, the deactivated FTS cobalt catalyst can regain the initial activity through the decomposition of bulk cobalt carbide to the Co-hcp structure.[13] At a low chemical potential of carbon, cobalt carbide is prone to decompose to metallic cobalt.[72] Cobalt carbide decomposition is slow in an inert atmosphere; however, it decomposes to metallic cobalt and graphitic carbon at a high temperature, i.e. between 300–350 °C.[72] But in a hydrogen atmosphere, cobalt carbide decomposes fast at a low temperature, i.e. between 150-200 °C.[72] Therefore, compared to temperature, a hydrogen environment plays a more decisive role in the stability of cobalt carbide.

2.2.2 Effect of cobalt carbide on CO conversion and product selectivity

The formation of cobalt carbide in FTS can lead to the deactivation of cobalt-based catalysts and a decrease in CO conversion.[61,68] Furthermore, bulk cobalt carbide has no activity for FTS.[73] But

the hcp phase metallic cobalt transformed from cobalt carbide exhibited higher catalytic activity in FTS compared with cobalt metal formed by the reduction of cobalt oxide.[70,74] Recently, Dai et al. studied the particle size effects of cobalt carbide for FTS and showed that, below 7 nm, the increase of Co_2C particle size resulted in enhanced intrinsic activity; however, when the Co_2C particles were larger than 7 nm, the intrinsic activity was independent of the particle size.[75]

Several studies have reported that the existence of Co_2C can lead to an increase in the selectivity of methane, CO_2 and isohydrocarbons.[61,62] Zhong et al. [76] reported that cobalt carbide nanoprisms formed from a CoMn catalyst exhibited high performance for Fischer-Tropsch to olefins (FTO) (conversion of syngas with high selectivity for lower olefins). Also, the cobalt carbide nanoprisms led to a significantly high selectivity to CO_2 because cobalt carbide was found to be active for the water-gas shift reaction, of which CO_2 is the one of the main products ($CO+H_2O \rightarrow CO_2+ H_2$).[76,77] Therefore, the effect of cobalt carbide on increasing the selectivity of CO_2 was confirmed. But the effect of cobalt carbide on increasing the olefin/paraffin ratio is still uncertain because a high olefin/paraffin ratio can be obtained on a metallic cobalt catalyst as well and is probably due to the promotion of Mn.[78–80]

Co-Co_2C derived from metallic cobalt carburization showed remarkable activity and selectivity for higher alcohols.[73,81] Moreover, with the promoters such as Li and La, single phase cobalt carbide also showed considerable activity and selectivity for higher alcohols.[63,82] In addition, Co-Co_2C has proved to be active for hydroformylation of 1-hexene experimentally and hydroformylation of ethene theoretically.[58]

2.2.3 CO activation mechanisms and DFT calculation results for cobalt carbide

In FTS, the surface metallic cobalt is considered to be responsible for the formation of hydrocarbons, and surface Co_2C is considered to be responsible for the formation of alcohols.[73] Density functional theory (DFT) calculations showed that the barrier for CO direct dissociation is significantly high on the carbon-rich surface of Co_2C, so that CO was non-dissociatively adsorbed on the Co_2C surface, whereas metallic cobalt was highly active for CO dissociative adsorption and the subsequent

hydrocarbon chain growth.[81,83,84] The conclusions provided by Li et al. and Sun et al. explained that with CO non-dissociation adsorption on cobalt carbide: the C–O bond is less weakened on the carburized cobalt because of the depletion of Co-d electrons; Co_2C is efficacious of CO adsorption, whereas is weaker for H adsorption than Co.[85,86] Moreover, non-dissociative adsorption of CO led to the CO insertion mechanism forming oxygenates.[81,84,87,88] Therefore, the interface of Co-Co_2C functioned as a dual active site for both hydrocarbon chain growth through CO dissociation on metallic cobalt, and the formation of oxygenates through CO non-dissociation adsorption on Co_2C.[73,81] However, the DTF results showed the interface of Co-Co_2C was also found to play a vital role in ethane hydroformylation (EH).[58] Metallic cobalt was considered to be active for olefin adsorption and activation to form surface carbonaceous species, while Co_2C was used for CO adsorption, activation and insertion. [58] However, EH has not been demonstrated experimentally.

DFT calculations also provide the properties of different crystal facets of cobalt carbide, and the exposure of different facets of cobalt carbide varies under different conditions.[83] At a higher chemical potential of carbon, the carbon-rich facets of cobalt carbide (e.g. (110) and (111)) are exposed, while at a lower chemical potential of carbon stoichiometric surfaces may appear (e.g. the (011) facet).[83] Cobalt-rich surfaces such as the (101) and (010) facets could be exposed because of the kinetics hindrance under carbon-poor or hydrogen-rich conditions.[83]

Different facets of cobalt carbide being exposed can result in differences in catalysis performance. Even for the same facets, (101) of Co_2C, CH_3 is the main form of CH_x species on a carbon-terminated surface, while CH is the main form of CH_x species on a cobalt-terminated surface.[90] Co_2C (111) exhibited the highest selectivity toward CH_4, owing to its valley-type surface structure and strong binding energy for CH_2 species, which inhibits C−C coupling.[91] Thus, the selectivity of FTS can be tuned by adjusting the exposure of the cobalt carbide facets and the termination of cobalt carbide.

2.3 Heterogenization of Hydroformylation

The hydroformylation process is the most commonly used homogeneous process in industry, with high selectivity (well in excess of 95%) to oxygenates using an optimal choice of reaction parameters

and process conditions.[40] The aldehydes can be manufactured stoichiometrically by adding carbon monoxide and hydrogen to olefins in one step with 100% atom efficiency.[92] However, the homogeneous process has intrinsic deficiencies, such as catalyst loss, catalyst separation and recycling, high cost of rhodium-based catalyst and metal species contamination in the aldehyde products.[38] It is for these reasons that much effort has been made to achieve hydroformylation in a heterogeneous process with solid catalysts.[92–94] One type of solid catalyst is homogeneous metal complex catalyst immobilized on various organic polymers and inorganic materials by physical adsorption, hydrogen bonding or chemical anchoring, using SiO_2,Al_2O_3, MgO, ZnO, clays, AC and zeolites.[94] The other type is a supported metal catalyst prepared by reduction or decomposition of a precursor (metal salt, oxide or complex) on a carrier (SiO_2, Al_2O_3, carbon, etc.).[95]

Although the homogeneous catalytic system with a metal complex has been applied in industrial OXO processes, hydroformylation over a supported metal catalyst is still worth studying for both academic and industrial purposes.[95] As rhodium and cobalt are widely used in industrial process, mono or bimetallic cobalt and rhodium in form of nanoparticles, clusters and complexes have been studied.[38,39,96–103] One disadvantage of Rh is that it is too expensive.[39] Therefore it would be interesting to investigate the catalytic performance of a cobalt catalyst promoted by a trace amount of Rh in terms of hydroformylation reactions.

2.4 Graphene Supported Catalysts in FTS and Hydroformylation

Graphene has become a well-known material in the past 16 years, since it was experimentally discovered in 2004 by Novoselov et al. [104] Many researchers have investigated the unique properties of graphene, and it has wide application in many fields, such as heterogeneous catalysis, electrochemical catalysis, adsorption and sensors.[105,106] Graphene has many unique properties, including: high electron mobility at room temperature (250,000 cm^2/Vs); exceptional thermal conductivity (5000 $Wm^{-1}K^{-1}$); superior mechanical properties, with a Young's modulus of 1 TPa; and a high theoretical specific surface area (2600 m^2/g). This means it is potentially an ideal substrate for use as a catalyst support.[107]

Graphene-supported iron and cobalt catalysts have been used in FTS. Furthermore, iron oxide nanoparticles supported on pyrolytic graphene oxide as a catalyst for FTS has proved effective for activity and selectivity tuning, particularly for C_{5+} hydrocarbons, and offers a new strategy to control the selectivity of iron-based FTS catalysts.[108] Qiao et al. [109] reported a one-pot hydrothermal hydrolysis–reduction method to synthesise a Fe/rGO nanohybrid. The resulting γ-Fe_2O_3 NPs were sub-3 nm in size and highly dispersed on RGO. The hybrid exhibited impressively high thermal stability and catalytic stability, as evidenced by the supported NPs remaining highly dispersed after reduction at 723 K for 16 h, and after subsequent FTS reaction at 543 K for 120 h.[109] However, with cobalt supported on graphene, the dispersion of cobalt particles increased greatly, and the average size of the cobalt crystal decreased. Furthermore, the graphene supported cobalt catalyst is more active and more stable than a CNTs-supported catalyst with the same cobalt loading, which leads to a decrease in the industrial-scale reactor volume (about 25–35%) and improves the cost of the process significantly.[110] Graphene-supported worm-like ruthenium was used as a catalyst for a photocatalytic FTS, which can catalyze the FT reaction at mild conditions (150 °C, 2.0 MPa H_2, and 1.0 MPa CO) under irradiation of visible light and achieve a catalytic activity as high as 14.4 mol $_{CO}\cdot mol_{Ru}^{-1}\cdot h^{-1}$.[111]

In recent years, graphene has been used as a support in hydroformylation due to its properties.[112–115] Tan et al. reported that an organic ligand of organic ligand triphenylphosphine (PPh_3) was used as a reducing agent to reduce graphene oxide, and as a functional group to fabricate a PPh_3 functionalized Rh/RGO heterogeneous catalyst simultaneously for 1-olefin hydroformylation.[116] It exhibited excellent catalytic performance.[116] Ioni et al. reported that methylated graphene oxide was used as a support for the formation of rhodium nanoparticles (2-3 nm) on the surface.[114] The prepared catalyst showed moderate and high substrate conversion as well as regioselectivity in hydroformylation of various olefins in the "green" medium of $scCO_2$ (supercritical CO_2).[114] A reduced graphene oxide (RGO) supported rhodium nanoparticle (Rh/RGO) catalyst was successfully prepared via the one-pot liquid phase reduction method and first applied in 1-hexene hydroformylation.[117] However, to the best of my knowledge, graphene-supported cobalt based catalysts or bimetallic catalysts have not been tested for hydroformylation of an olefin.

2.5 Metal Support Interaction Using Graphene as a Support in FTS and Hydroformylation

Metal heterogeneously dispersed on a support plays a vital role in the catalysis of a wide range of industrial reactions. Metal-supported interactions (MSI) in catalysts have received much attention in recent years because of its strong impact on catalysis.[118–121] The catalysis can be influenced by MSI through charge transfer, the interfacial perimeter, nanoparticle morphology, chemical composition or strong MSI.[122,123] Furthermore, the intermetallic compounds formed through MSI are highly active for the corresponding reactions.[124,125] Therefore, strategies for tuning the MSI to enhance the performance of catalysts has been well studied for commercial supports, especially metal oxide supports.[122,123,126] The discovery and tuning of MSI is of great significance in obtaining target products from complex products of FTS and ethylene hydroformylation, including hydrocarbons and oxygenates.[101,119,120,127,128]

Carbon materials have been applied in the fields of syngas conversion for decades because of the relative weak MSI which is easy to tailor the catalyst properties.[129] Likewise, carbon materials were also used as support for the heterogeneous hydroformylation such as nanotube [130–132], AC [133–135], graphite nanofiber [136] and other carbon materials.[137] In recent years, graphene - the basic building block of graphitic materials with unique properties - has been used as a support in hydroformylation.[112–115] However, these studies only focused on the catalytic performance and MSI was not discussed.[113–115] Hence, there is a need to investigate and develop tuning strategies for MSI in graphene-based hydroformylation catalysts, which is of great importance for heterogenization of the industrial hydroformylation process.

2.6 Relationship Between FTS and EH: Mechanisms and Reaction Pathways

The C-C bond formation is a key elementary step in the FTS reaction producing long chain hydrocarbons from syngas.[138] C-H bond formation is another key elementary step for CO dissociation to form intermediate for chain growth, as reported for various FTS mechanisms,[34,139–142] and for the termination of chain growth.[138] C-C bond formation and C-H bond formation are also involved in EH, which was discovered by Otto Roelen when he attempted to recycle olefins in

FTS. [36,38,143] These were considered to be secondary reactions of ethene during FTS.[29,31,34] Although industrial hydroformylation is usually carried out through a homogeneous process,[38,40] the reaction of $CO/C_2H_4/H_2$ is still receiving attention as a model reaction to study the mechanism of hydroformylation [39,144] and as an ethene co-feeding FTS reaction to study the mechanism of FTS.[28–31,34,145,146]

Much work has been reported on the reaction of $CO/C_2H_4/H_2$ on cobalt-based catalysts, which helps with understanding the FTS mechanisms and the effect of ethene on FTS. Co-feeding ethene to FTS leads to a decrease in methane selectivity,[147] an increase in selectivity of C_{5-6} products [147] and an increase in the O/P ratio of C_{3-6} hydrocarbons.[31] In terms of the mechanism, isotopic labeled experiments were done and it was found that the C_1 species can be generated from ethene to form methane and long chain hydrocarbons.[28,31] Recently, the surface reactions of chemisorbed ethene on Co(0001) with CO spectators have been extensively studied by Weststrate through near-ambient pressure XPS.[138,148] An alkylidyne intermediates mechanism was proposed for FTS chain growth.[138,148] However, all these findings were observed on metallic cobalt, on which CO can be dissociated directly or with the assistance of H. Although the alkylidyne intermediates mechanism provides a compelling explanation for FTS chain growth, the mechanisms for propionaldehyde and alcohols are still in ‘the black box’ awaiting investigation.

References

[1] V. Navarro, M.A. van Spronsen, J.W.M. Frenken, In situ observation of self-assembled hydrocarbon Fischer–Tropsch products on a cobalt catalyst, (2016) 1–6. https://doi.org/10.1038/NCHEM.2613.

[2] H. Schulz, Short history and present trends of Fischer–Tropsch synthesis, Appl. Catal. A Gen. 186 (1999) 3–12. https://doi.org/10.1016/S0926-860X(99)00160-X.

[3] A.C. Vosloo, Fischer-Tropsch: A futuristic view, Fuel Process. Technol. 71 (2001) 149–155. https://doi.org/10.1016/S0378-3820(01)00143-6.

[4] E.W. Kuipers, C. Scheper, J.H. Wilson, I.H. Vinkenburg, H. Oosterbeek, Non-ASF product distributions due to secondary reactions during Fischer–Tropsch Synthesis, J. Catal. 158 (1996) 288–300.

[5] J. van de Loosdrecht, F.G. Botes, I.M. Ciobica, A. Ferreira, P. Gibson, D.J. Moodley, A. M. Saib, J.L. Visagie, C.J. Westrate, J.W. (Hans) Niemantsverdriet, K. Binnemans, Comprehensive inorganic chemistry: Fischer-Tropsch Synthesis: Catalysts and chemistry, Elsevier Ltd., 7,2013, 525-557. https://doi.org/10.1016/B978-0-08-097774-4.00729-4.

[6] M. Dry, The Fischer–Tropsch process: 1950–2000, Catal. Today. 71 (2002) 227–241. http://www.sciencedirect.com/science/article/pii/S0920586101004539 (Accessed August 14, 2015).

[7] B.H. Davis, Fischer-Tropsch synthesis: Comparison of performances of iron and cobalt catalysts, Ind. Eng. Chem. Res. 46 (2007) 8938–8945. https://doi.org/10.1021/ie0712434.

[8] G. Jacobs, T.K. Das, Y. Zhang, J. Li, G. Racoillet, B.H. Davis, Fischer-Tropsch synthesis: Support, loading, and promoter effects on the reducibility of cobalt catalysts, Appl. Catal. A Gen. 233 (2002) 263–281. https://doi.org/10.1016/S0926-860X(02)00195-3.

[9] J. Loosdrecht, F. Botes, Fischer-Tropsch synthesis: Catalysts and chemistry, Compr. Inorg. Chem. II. (2013) 525–557. http://dx.doi.org/10.1016/8978-0-08-097774-4.00729-4 (accessed August 19, 2015).

[10] Ø. Borg, P.D.C. Dietzel, A.I. Spjelkavik, E.Z. Tveten, J.C. Walmsley, S. Diplas, S. Eri, A. Holmen, E. Rytter, Fischer-Tropsch synthesis: Cobalt particle size and support effects on intrinsic activity

and product distribution, J. Catal. 259 (2008) 161–164. https://doi.org/10.1016/j.jcat.2008.08.017.

[11] S. Iqbal, T.E. Davies, J.S. Hayward, D.J. Morgan, K. Karim, J.K. Bartley, S.H. Taylor, G.J. Hutchings, Fischer-Tropsch Synthesis using promoted cobalt-based catalysts, Catal. Today. 272 (2016) 74–79. https://doi.org/10.1016/j.cattod.2016.04.012.

[12] Q. Zhang, W. Deng, Y. Wang, Recent advances in understanding the key catalyst factors for Fischer-Tropsch synthesis, J. Energy Chem. 22 (2013) 27–38. https://doi.org/10.1016/S2095-4956(13)60003-0.

[13] N.E. Tsakoumis, M. Rønning, Ø. Borg, E. Rytter, A. Holmen, Deactivation of cobalt based Fischer-Tropsch catalysts: A review, Catal. Today. 154 (2010) 162–182. https://doi.org/10.1016/j.cattod.2010.02.077.

[14] A.M. Saib, D.J. Moodley, I.M. Ciobîc, M.M. Hauman, B.H. Sigwebela, Fundamental understanding of deactivation and regeneration of cobalt Fischer–Tropsch synthesis catalysts, Catal. Today. 154 (2010) 271–282. https://doi.org/10.1016/j.cattod.2010.02.008.

[15] D. Moodley, M. Claeys, E. van Steen, P. van Helden, D. Kistamurthy, K. Weststrate, H. Niemantsverdriet, A. Saib, W. Erasmus, J. van de Loosdrecht, Sintering of cobalt during FTS : Insights from industrial and model systems, Catal. Today. (2019) 0–1. https://doi.org/10.1016/j.cattod.2019.03.059.

[16] M. Catalysis, H. Monsanto, S. Olivti, R. January, Mechanism of Fischer-Tropsch Synthesis: CH_2 polymerization versus CO insertion, 16 (1982), 111-115.

[17] D. Glasser, D. Hildebrandt, X. Liu, X. Lu, C.M. Masuku, Recent advances in understanding the Fischer-Tropsch Synthesis (FTS) reaction, Curr. Opin. Chem. Eng. 1 (2012) 296–302. https://doi.org/10.1016/j.coche.2012.02.001.

[18] B.H. Davis, Fischer-Tropsch synthesis: Current mechanism and futuristic needs, Fuel Process. Technol. 71 (2001) 157–166. https://doi.org/10.1016/S0378-3820(01)00144-8.

[19] H. Mahmoudi, M. Mahmoudi, O. Doustdar, H. Jahangiri, A review of Fischer-Tropsch synthesis process, mechanism, surface chemistry and catalyst formulation, Biofuels Eng. 2 (2017) 11–31.

[20] J. Gaube, H. Klein, Studies on the reaction mechanism of the Fischer–Tropsch synthesis on

iron and cobalt, J. Mol. Catal. A Chem. (2008). http://www.sciencedirect.com/science/article/pii/S1381116907006711 (accessed August 19, 2015).

[21] M. Ojeda, R. Nabar, A.U. Nilekar, A. Ishikawa, M. Mavrikakis, E. Iglesia, CO activation pathways and the mechanism of Fischer-Tropsch synthesis, J. Catal. 272 (2010) 287–297. https://doi.org/10.1016/j.jcat.2010.04.012.

[22] A.W. Chen, B. Zijlstra, R. Pestman, E. Hensen, W. Chen, B. Zijlstra, R. Pestman, E.J.M. Mechanism of CO dissociation on a cobalt Fischer–Tropsch catalyst,10, 2018, 1-1,. https://doi.org/10.1002/cctc.201701203.

[23] M. Ojeda, R. Nabar, A.U. Nilekar, A. Ishikawa, M. Mavrikakis, E. Iglesia, CO activation pathways and the mechanism of Fischer–Tropsch synthesis, J. Catal. 272 (2010) 287–297. https://doi.org/10.1016/j.jcat.2010.04.012.

[24] J. Yang, Y. Qi, J. Zhu, Y.A. Zhu, D. Chen, A. Holmen, Reaction mechanism of CO activation and methane formation on Co Fischer-Tropsch catalyst: A combined DFT, transient, and steady-state kinetic modeling, J. Catal. 308 (2013) 37–49. https://doi.org/10.1016/j.jcat.2013.05.018.

[25] C.J. Weststrate, I.M. Ciobîc, A.M. Saib, D.J. Moodley, J.W. Niemantsverdriet, Fundamental issues on practical Fischer–Tropsch catalysts : How surface science can help, 228 (2014) 106–112.

[26] V. Sage, N. Burke, Use of probe molecules for Fischer–Tropsch mechanistic investigations : A short review, 178 (2011) 137–141. https://doi.org/10.1016/j.cattod.2011.09.013.

[27] F. Tropsch, S.A. Review, C.M. Masuku, Effect of co-feeding inorganic and organic molecules in the Fe and Co catalyzed Fischer–Tropsch Synthesis: A Review, Catal. Rev. 9 (2019) 746.

[28] G.J. Hutchings, R.G. Copperthwaite, M. van der Riet, Low methane selectivity using Co/MnO catalysts for the Fischer-Tropsch reaction: Effect of increasing pressure and Co-feeding ethene, Top. Catal. 2 (1995) 163–172. https://doi.org/10.1007/BF01491964.

[29] L. Espinoza, Secondary reactions of primary products of the Fischer-Tropsch synthesis, Part 1. The role of ethene, J. Mol. Catal. 43 (1987) 237–247.

[30] E.S.P.B. V, R.R. Hudgins, P.L. Silveston, Effect of ethene addition during the Fischer- Tropsch

reaction, 62 (1990) 295–308.

[31] J. Yang, C. Ledesma Rodriguez, Y. Qi, H. Ma, A. Holmen, D. Chen, The effect of co-feeding ethene on Fischer-Tropsch synthesis to olefins over Co-based catalysts, Appl. Catal. A Gen. 598 (2020) 117564. https://doi.org/10.1016/j.apcata.2020.117564.

[32] Y. Zhang, M. Tshwaku, Y. Yao, X. Liu, D. Hildebrandt, J. Chang, Reaction of ethylene over a typical Fischer-Tropsch synthesis Co / TiO 2 catalyst, Eng. Reports. (2020) 1–18. https://doi.org/10.1002/eng2.12232.

[33] M. Zhang, H. Huang, Y. Yu, Insight into the mechanism of ethylene decomposition over Co (0001) Surface : Formation of carbon species, Catal. Letters. 149, (2019), 744-752. https://doi.org/10.1007/s10562-019-02676-z.

[34] Y. Zhang, Y. Yao, J. Chang, X. Lu, X. Liu, D. Hildebrandt, Fischer–Tropsch synthesis with ethene co-feeding: Experimental evidence of the CO-insertion mechanism at low temperature, AIChE J. n/a (2020) e17029. https://doi.org/10.1002/aic.17029.

[35] C.J.K. Weststrate, D. Sharma, D.G. Rodriguez, H.O.A. Fredriksson, J.W.H. Niemantsverdriet, M.A. Gleeson, Mechanistic insight into carbon-carbon bond formation on cobalt under simulated Fischer-Tropsch synthesis conditions, Nat. Commun. 11 (2020) 750. https://doi.org/10.1038/s41467-020-14613-5.

[36] O. Roelen, United States Patent Office 2327,066, (1943).

[37] B. Breit, Recent advances in alkene hydroformylation, Top Curr Chem (2007) 279: 139–172.

[38] K. Wiese, D. Obst, Hydroformylation, Catal. Carbonylation React. 18 (2006) 1–33. https://doi.org/10.1007/3418_015.

[39] R. Franke, D. Selent, A. Borner, Applied hydroformylation, Chem. Rev. 112 (2012) 5675–5732. https://doi.org/10.1021/cr3001803.

[40] H.-W. Bohnen, B. Cornils, Hydroformylation of alkenes: An industrial view of the status and importance, Adv. Catal. 17 (2002) 1–64. https://doi.org/10.1016/S0360-0564(02)47005-8.

[41] E. V. Gusevskaya, J. Jiménez-Pinto, A. Börner, Hydroformylation in the realm of scents, ChemCatChem. 6 (2014) 382–411. https://doi.org/10.1002/cctc.201300474.

[42] H.-W. Bohnen, B.B.T.-A. in C. Cornils, Hydroformylation of alkenes: An industrial view of the status and importance, in: Academic Press, 2002: pp. 1–64.

https://doi.org/https://doi.org/10.1016/S0360-0564(02)47005-8.

[43] G.G. Stanley, Hydroformylation (OXO) Catalysis, Kirk-Othmer Encycl. Chem. Technol. 1 (2017) 1–19. https://doi.org/10.1002/0471238961.1524150209121.a01.pub2.

[44] L.T. Mika, F. Ungváry, Hydroformylation - Homogenous, Encycl. Catal. 2011 (2011).

[45] H.-U. Blaser, A. Indolese, A. Schnyder, Applied homogeneous catalysis, Curr. Sci. 78 (2000) 1336–1344. https://doi.org/10.1002/anie.201208808.

[46] H. Schulz, Major and minor reactions in Fischer-Tropsch synthesis on cobalt catalysts, Top. Catal. 26 (2003) 73–85. https://doi.org/10.1023/B:TOCA.0000012988.86378.21.

[47] I. Edition, T.E. Kron, O.G. Karchevskaya, S.N. Rush, D. V Marochkin, G.A. Korneeva, M.N. Mikhailov, I.M. Bedrina, A.E. Bessudnov, D. Centre, Hydroformylation of olefins produced in the Fischer—Tropsch synthesis, Russ. Chem. Bull., Int. Ed. 68 (2019) 1662–1668.

[48] G.M. Torres, R. Frauenlob, R. Franke, A. Börner, Production of alcohols via hydroformylation, Catal. Sci. Technol. 5 (2015) 34–54. https://doi.org/10.1039/C4CY01131G.

[49] G. Henrici-Olivé, S. Olivé, Hydroformylation and Fischer-Tropsch reaction - Analogies and discrepancies, J. Mol. Catal. 3 (1978) 443–446.

[50] B.H. Davis, M.L. Occelli, Advances in Fischer-Tropsch Synthesis, Catalysts, and Catalysis, 1st Edition, CRC Press, 2010. https://doi.org/https://doi.org/10.1201/9781420062571.

[51] K. Fang, D. Li, M. Lin, M. Xiang, W. Wei, Y. Sun, A short review of heterogeneous catalytic process for mixed alcohols synthesis via syngas, Catal. Today. 147 (2009) 133–138. https://doi.org/10.1016/j.cattod.2009.01.038.

[52] A. Fukuoka, T. Kimura, N. Kosugi, H. Kuroda, Y. Minai, Y. Sakai, T. Tominaga, M. Ichikawa, Bimetallic promotion of alcohol production in CO hydrogenation and olefin hydroformylation on RhFe, PtFe, PdFe, and IrFe cluster-derived catalysts, J. Catal. 126 (1990) 434–450. https://doi.org/10.1016/0021-9517(90)90010-H.

[53] K. Xiao, Z. Bao, X. Qi, X. Wang, L. Zhong, K. Fang, M. Lin, Y. Sun, Advances in bifunctional catalysis for higher alcohol synthesis from syngas, Chinese J. Catal. 34 (2013) 116–129. https://doi.org/10.1016/S1872-2067(11)60496-8.

[54] Y.P. Pei, J.X. Liu, Y.H. Zhao, Y.J. Ding, T. Liu, W. Da Dong, H.J. Zhu, H.Y. Su, L. Yan, J.L. Li, W.X. Li, High alcohols synthesis via Fischer-Tropsch reaction at cobalt metal/carbide interface,

ACS Catal. 5 (2015) 3620–3624. https://doi.org/10.1021/acscatal.5b00791.

[55] Z. Zhao, W. Lu, R. Yang, H. Zhu, W. Dong, F. Sun, Z. Jiang, Y. Lyu, T. Liu, H. Du, Y. Ding, Insight into the formation of Co@Co2C catalysts for direct synthesis of higher alcohols and olefins from syngas, ACS Catal. 8 (2018) 228–241. https://doi.org/10.1021/acscatal.7b02403.

[56] Y. Xiang, N. Kruse, Tuning the catalytic CO hydrogenation to straight and long-chain aldehydes/alcohols and olefins/paraffins, Nat. Commun. 7 (2016) 1–6. https://doi.org/10.1038/ncomms13058.

[57] R. Zhang, G. Wen, H. Adidharma, A.G. Russell, B. Wang, M. Radosz, M. Fan, C2 oxygenate dynthesis via Fischer–Tropsch Synthesis on Co_2C and Co/Co_2C interface catalysts: How to control the catalyst crystal facet for optimal selectivity, ACS Catal. 7 (2017) 8285–8295. https://doi.org/10.1021/acscatal.7b02800.

[58] W. Dong, J. Liu, H. Zhu, Y. Ding, Y. Pei, J. Liu, H. Du, M. Jiang, T. Liu, H. Su, W. Li, Co–Co_2C and Co–Co_2C/AC catalysts for hydroformylation of 1-Hexene under low pressure: Experimental and theoretical studies, J. Phys. Chem. C. 118 (2014) 19114–19122. https://doi.org/10.1021/jp504215y.

[59] S.R. Craxford, The Fischer-Tropsch synthesis of hydrocarbons, and some related reactions, Trans. Faraday Soc. 35 (1939) 946–958. https://doi.org/10.1039/TF9393500946.

[60] S. Weller, L.J.E. Hofer, R.B. Anderson, The role of bulk cobalt carbide in the Fischer—Tropsch Synthesis , J. Am. Chem. Soc. 70 (1948) 799–801. https://doi.org/10.1021/ja01182a108.

[61] M. Claeys, M.E. Dry, E. van Steen, E. Du Plessis, P.J. van Berge, A.M. Saib, D.J. Moodley, In situ magnetometer study on the formation and stability of cobalt carbide in Fischer-Tropsch synthesis, J. Catal. 318 (2014) 193–202. https://doi.org/10.1016/j.jcat.2014.08.002.

[62] Q. Lin, B. Liu, F. Jiang, X. Fang, Y. Xu, X. Liu, Assessing the formation of cobalt carbide and its catalytic performance under realistic reaction conditions and tuning product selectivity in a cobalt-based FTS reaction, Catal. Sci. Technol. 9 (2019) 3238–3258. https://doi.org/10.1039/C9CY00328B.

[63] Y. Pei, Y. Ding, H. Zhu, Study on the effect of alkali promoters on the formation of cobalt carbide (Co_2C) and on the performance of Co_2C via CO hydrogenation reaction, (2014) 505–520. https://doi.org/10.1007/s11144-013-0663-1.

[64] V.M. Lebarbier, D. Mei, D.H. Kim, A. Andersen, J.L. Male, J.E. Holladay, R. Rousseau, Y. Wang, Effects of La_2O_3 on the mixed higher alcohols synthesis from syngas over co catalysts: A combined theoretical and experimental study, J. Phys. Chem. C. 115 (2011) 17440–17451. https://doi.org/10.1021/jp204003q.

[65] H. Du, H. Zhu, X. Chen, W. Dong, W. Lu, W. Luo, M. Jiang, T. Liu, Y. Ding, Study on CaO-promoted Co/AC catalysts for synthesis of higher alcohols from syngas, Fuel. 182 (2016) 42–49. https://doi.org/10.1016/j.fuel.2016.05.089.

[66] J.A. Singh, A.S. Hoffman, J. Schumann, A. Boubnov, A.S. Asundi, S.S. Nathan, J. Nørskov, S.R. Bare, S.F. Bent, Role of Co2C in ZnO-promoted Co catalysts for alcohol synthesis from syngas, ChemCatChem. 11 (2019) 799–809. https://doi.org/https://doi.org/10.1002/cctc.201801724.

[67] P. Hasin, Low-temperature synthesis of mesoporous cobalt(II) carbide using graphene oxide as a carbon source, J. Phys. Chem. C. 118 (2014) 4726–4732. https://doi.org/10.1021/jp411844a.

[68] J. Xiong, Y. Ding, T. Wang, L. Yan, W. Chen, H. Zhu, Y. Lu, The formation of Co2C species in activated carbon supported cobalt-based catalysts and its impact on Fischer-Tropsch reaction, Catal. Letters. 102 (2005) 265–269. https://doi.org/10.1007/s10562-005-5867-1.

[69] J.C. Mohandas, M.K. Gnanamani, G. Jacobs, W. Ma, Y. Ji, S. Khalid, B.H. Davis, Fischer-Tropsch synthesis: Characterization and reaction testing of cobalt carbide, ACS Catal. 1 (2011) 1581–1588. https://doi.org/10.1021/cs200236q.

[70] G. Kwak, D.-E. Kim, Y.T. Kim, H.-G. Park, S.C. Kang, K.-S. Ha, K.-W. Jun, Y.-J. Lee, Enhanced catalytic activity of cobalt catalysts for Fischer–Tropsch synthesis via carburization and hydrogenation and its application to regeneration, Catal. Sci. Technol. 6 (2016) 4594–4600. https://doi.org/10.1039/C5CY01399B.

[71] N.E. Tsakoumis, R. Dehghan, R.E. Johnsen, A. Voronov, W. van Beek, J.C. Walmsley, Ø. Borg, E. Rytter, D. Chen, M. Rønning, A. Holmen, A combined in situ XAS-XRPD-Raman study of Fischer-Tropsch synthesis over a carbon supported Co catalyst, Catal. Today. 205 (2013) 86–93. https://doi.org/10.1016/j.cattod.2012.08.041.

[72] A.P. Petersen, M. Claeys, P.J. Kooyman, E. van Steen, Cobalt-Based Fischer–Tropsch

Synthesis : A kinetic inverse model system, Catalysts 2019, 9, 794.

[73] Y. Pei, Y. Ding, J. Zang, X. Song, W. Dong, H. Zhu, T. Wang, W. Chen, Fischer-Tropsch synthesis: Characterizing and reaction testing of Co2C/SiO2 and Co2C/Al2O3 catalysts, Cuihua Xuebao/Chinese J. Catal. 36 (2015) 252–259. https://doi.org/10.1016/S1872-2067(14)60179-0.

[74] G. Kwak, M.H. Woo, S.C. Kang, H.G. Park, Y.J. Lee, K.W. Jun, K.S. Ha, In situ monitoring during the transition of cobalt carbide to metal state and its application as Fischer-Tropsch catalyst in slurry phase, J. Catal. 307 (2013) 27–36. https://doi.org/10.1016/j.jcat.2013.06.029.

[75] Y. Dai, Y. Zhao, T. Lin, S. Li, F. Yu, Y. An, X. Wang, K. Xiao, F. Sun, Z. Jiang, Y. Lu, H. Wang, L. Zhong, Y. Sun, Particle size effects of cobalt carbide for Fischer–Tropsch to olefins, ACS Catal. 9 (2019) 798–809. https://doi.org/10.1021/acscatal.8b03631.

[76] L. Zhong, F. Yu, Y. An, Y. Zhao, Y. Sun, Z. Li, T. Lin, Y. Lin, X. Qi, Y. Dai, L. Gu, J. Hu, S. Jin, Q. Shen, H. Wang, Cobalt carbide nanoprisms for direct production of lower olefins from syngas, Nature. 538 (2016) 84–87. https://doi.org/10.1038/nature19786.

[77] M.K. Gnanamani, G. Jacobs, W.D. Shafer, D.E. Sparks, S. Hopps, G.A. Thomas, B.H. Davis, Low temperature water–gas shift reaction over alkali metal promoted cobalt carbide catalysts, Top. Catal. 57 (2014) 612–618. https://doi.org/10.1007/s11244-013-0219-7.

[78] M. Moyo, M.A.M. Motchelaho, H. Xiong, L.L. Jewell, N.J. Coville, Promotion of Co/carbon sphere Fischer-Tropsch catalysts by residual K and Mn from carbon oxidation by KMnO 4, Appl. Catal. A Gen. 413–414 (2012) 223–229. https://doi.org/10.1016/j.apcata.2011.11.012.

[79] W.G. Zhou, J.Y. Liu, X. Wu, J.F. Chen, Y. Zhang, An effective Co/MnOx catalyst for forming light olefins via Fischer-Tropsch synthesis, Catal. Commun. 60 (2015) 76–81. https://doi.org/10.1016/j.catcom.2014.10.027.

[80] Z. Li, L. Zhong, F. Yu, Y. An, Y. Dai, Y. Yang, T.-J. Lin, S. Li, H. Wang, P. Gao, Y. Sun, M. He, Effects of sodium on the catalytic performance of CoMn catalysts for Fischer-Tropsch to olefins, ACS Catal. 7, (2017), 3622-3631. https://doi.org/10.1021/acscatal.6b03478.

[81] Y.P. Pei, J.X. Liu, Y.H. Zhao, Y.J. Ding, T. Liu, W. Da Dong, H.J. Zhu, H.Y. Su, L. Yan, J.L. Li, W.X. Li, High alcohols synthesis via Fischer-Tropsch reaction at cobalt metal/carbide interface, ACS Catal. 5 (2015) 3620–3624. https://doi.org/10.1021/acscatal.5b00791.

[82] G. Jiao, Y. Ding, H. Zhu, X. Li, J. Li, R. Lin, W. Dong, L. Gong, Y. Pei, Y. Lu, Effect of La2O3 doping on syntheses of C1-C18 mixed linear alcohols from syngas over the Co/AC catalysts, Appl. Catal. A Gen. 364 (2009) 137–142. https://doi.org/10.1016/j.apcata.2009.05.040.

[83] P. Chen, J. Liu, W. Li, Carbon monoxide activation on cobalt carbide for Fischer–Tropsch Synthesis from First-Principles Theory, ACS Catal. 9 (2019) 8093–8103. https://doi.org/10.1021/acscatal.9b00649.

[84] J.X. Liu, W.X. Li, Theoretical study of crystal phase effect in heterogeneous catalysis, Wiley Interdiscip. Rev. Comput. Mol. Sci. 6 (2016) 571–583. https://doi.org/10.1002/wcms.1267.

[85] F. Sun, R. Yang, Z. Xia, Y. Yang, Z. Zhao, S. Gu, Effects of cobalt carbide on Fischer–Tropsch synthesis with MnO supported Co-based catalysts, J. Energy Chem. 42 (2020) 227–232. https://doi.org/10.1016/j.jechem.2019.07.007.

[86] B. Li, Q. Zhang, L. Chen, X. Pan, Vacancy-mediated diffusion of carbon in cobalt and its influence on CO activation, (2010) 7848–7855. https://doi.org/10.1039/b925764k.

[87] M.K. Gnanamani, G. Jacobs, U.M. Graham, M.C. Ribeiro, F.B. Noronha, W.D. Shafer, B.H. Davis, Influence of carbide formation on oxygenates selectivity during Fischer-Tropsch synthesis over Ce-containing Co catalysts, Catal. Today. 261 (2016) 40–47. https://doi.org/10.1016/j.cattod.2015.08.047.

[88] M. Athariboroujeny, A. Raub, V. Iablokov, S. Chenakin, L. Kovarik, N. Kruse, Competing mechanisms in CO hydrogenation over Co-MnOx catalysts, ACS Catal. 9 (2019) 5603–5612. https://doi.org/10.1021/acscatal.9b00967.

[89] Y. Zhao, H. Su, K. Sun, J. Liu, W. Li, Structural and electronic properties of cobalt carbide Co 2 C and its surface stability: Density functional theory study, 606 (2012) 598–604. https://doi.org/10.1016/j.susc.2011.11.025.

[90] P. Liu, D. Liang, R. Zhang, B. Wang, The formation of C2 species and CH4 over the Co2C catalyst in Fischer-Tropsch synthesis: The effect of surface termination on product selectivity, Comput. Mater. Sci. 172 (2020) 109345. https://doi.org/https://doi.org/10.1016/j.commatsci.2019.109345.

[91] B. Liu, W. Li, Y. Xu, Q. Lin, F. Jiang, X. Liu, Insight into the intrinsic active site for selective production of light olefins in cobalt-catalyzed Fischer–Tropsch Synthesis, ACS Catal. 9 (2019)

7073–7089. https://doi.org/10.1021/acscatal.9b00352.

[92] C. Li, W. Wang, L. Yan, Y. Ding, A mini review on strategies for heterogenization of rhodium-based hydroformylation catalysts, (2017). https://doi.org/https://doi.org/10.1007/s11705-017-1672-9.

[93] X. Wang, Recent advances in continuous rhodium-catalyzed hydroformylation, J. Flow Chem. 5 (2015) 125–132. https://doi.org/10.1556/1846.2015.00003.

[94] Â.C.B. Neves, M.J.F. Calvete, T.M.V.D. Pinho E Melo, M.M. Pereira, Immobilized catalysts for hydroformylation reactions: A versatile tool for aldehyde synthesis, European J. Org. Chem. (2012) 6309–6320. https://doi.org/10.1002/ejoc.201200709.

[95] V.A. Likholobov, B.L. Moroz, Hydroformylation on solid catalysts, Handb. Heterog. Catal. (2008). https://doi.org/10.1002/9783527610044.hetcat0189.

[96] S.I. Reut, G.L. Kamalov and G.I. Golodets, Kinetics of heterogeneous catalytic hydroformylation of propylene on rhodium-cobalt catalysts. Reaction Mechanism, React. Kinet. Catal. Lett., 44 (1991) 191–195.

[97] L. Wang, W. Zhang, S. Wang, Z. Gao, Z. Luo, X. Wang, R. Zeng, A. Li, H. Li, M. Wang, X. Zheng, J. Zhu, W. Zhang, C. Ma, R. Si, J. Zeng, Atomic-level insights in optimizing reaction paths for hydroformylation reaction over Rh/CoO single-atom catalyst, Nat. Commun. 7 (2016) 1–8. https://doi.org/10.1038/ncomms14036.

[98] J.Y. Kim, J.H. Park, O.S. Jung, Y.K. Chung, K.H. Park, Heterogenized catalysts containing cobalt-rhodium heterobimetallic nanoparticles for olefin hydroformylation, Catal. Letters. 128 (2009) 483–486. https://doi.org/10.1007/s10562-008-9776-y.

[99] X. Qiu, N. Tsubaki, S. Sun, K. Fujimoto, Promoting efect of noble metals to Co/SiO2 catalysts for hydroformylation of 1-hexene, Catal. Commun. 2. 2 (2001) 75–80.

[100] N. Navidi, J.W. Thybaut, G.B. Marin, Experimental investigation of ethylene hydroformylation to propanol on Rh and Co based catalysts, CHISA 2012 - 20th Int. Congr. Chem. Process Eng. PRES 2012 - 15th Conf. PRES. 469 (2012) 357–366. http://www.scopus.com/inward/record.url?eid=2-s2.0-84874870414&partnerID=MN8TOARS.

[101] L. Huang, Y. Xu, G. Piao, A. Liu, Enhancement of olefin hydroformylation related to supported bimetallic Rh-Co clusters, Catal. Letters. 23 (1994) 87–95.

[102] M. Marchionna, G. Longoni, Hydroformylation of formaldehyde catalyzed by cobalt-rhodium bimetallic systems, J. Mol. Catal. 35 (1986) 107–118. https://doi.org/10.1016/0304-5102(86)85061-1.

[103] L. Huang, Y. Xu, G. Piao, A. Liu, Enhancement of olefin hydroformylation related to supported bimetallic Rh-Co clusters, 23 (1994) 87–95.

[104] K.S. Novoselov, A.K. Geim, S. V Morozov, D. Jiang, Y. Zhang, S. V Dubonos, I. V Grigorieva, A.A. Firsov, Electric Field Effect in Atomically Thin Carbon Films, Science (80). 306 (2004) 666–669. https://doi.org/10.1126/science.1102896.

[105] J. Xu, R.S. Ruoff, H. Zhu, The physics and chemistry of graphene-on-surfaces, Chem. Soc. Rev. 46 (2017) 4417–4449. https://doi.org/10.1039/C7CS00256d.

[106] Y. Cheng, Y. Fan, Y. Pei, M. Qiao, Graphene-supported metal/metal oxide nanohybrids: synthesis and applications in heterogeneous catalysis, Catal. Sci. Technol. 5 (2015) 3903–3916. https://doi.org/10.1039/C5CY00630A.

[107] V. Singh, D. Joung, L. Zhai, S. Das, Progress in materials science graphene based materials : Past, present and future, Prog. Mater. Sci. 56 (2011) 1178–1271. https://doi.org/10.1016/j.pmatsci.2011.03.003.

[108] H. Zhao, Q. Zhu, Y. Gao, P. Zhai, D. Ma, Applied Catalysis A : General Iron oxide nanoparticles supported on pyrolytic graphene oxide as model catalysts for Fischer-Tropsch synthesis, "Applied Catal. A, Gen. 456 (2013) 233–239. https://doi.org/10.1016/j.apcata.2013.03.006.

[109] B. Sun, Z. Jiang, D. Fang, K. Xu, Y. Pei, S. Yan, M. Qiao, K. Fan, B. Zong, One-pot approach to a highly robust iron oxide/reduced graphene oxide nanocatalyst for Fischer-Tropsch Synthesis, ChemCatChem. 5 (2013) 714–719. https://doi.org/10.1002/cctc.201200653.

[110] A. Tavasoli, K. Sadagiani, F. Khorashe, A. A. Seifkordi, A. A. Rohani, A. Nakhaeipour, Cobalt supported on carbon nanotubes - A promising novel Fischer-Tropsch synthesis catalyst, Fuel Process. Technol. 89 (2008) 491–498. https://doi.org/10.1016/j.fuproc.2007.09.008.

[111] X. Guo, Z. Jiao, G. Jin, X.-Y. Guo, Photocatalytic Fischer–Tropsch Synthesis on graphene-supported worm-like ruthenium nanostructures, ACS Catal. (2015) 150519165718003. https://doi.org/10.1021/acscatal.5b00697.

[112] V. Singh, D. Joung, L. Zhai, S. Das, S.I. Khondaker, S. Seal, Graphene based materials: Past,

present and future, Prog. Mater. Sci. 56 (2011) 1178–1271. https://doi.org/10.1016/j.pmatsci.2011.03.003.

[113] M. Tan, Y. Ishikuro, Y. Hosoi, N. Yamane, P. Ai, P. Zhang, G. Yang, M. Wu, R. Yang, N. Tsubaki, PPh 3 functionalized Rh/rGO catalyst for heterogeneous hydroformylation: Bifunctional reduction of graphene oxide by organic ligand, Chem. Eng. J. (2017). https://doi.org/10.1016/j.cej.2017.08.023.

[114] Y. V. Ioni, S.E. Lyubimov, V.A. Davankov, S.P. Gubin, Modified graphene oxide as a support for rhodium nanoparticles active in olefin hydroformylation*, Russ. Chem. Bull. Int. Ed. 63 (2014) 2243–2249.

[115] A. Manuscript, Active and regioselective rhodium catalyst supported on reduced graphene oxide for 1-hexene hydroformylation, Catal. Sci. Technol. (2015) 1162–1172. https://doi.org/10.1039/C5CY01355K.

[116] M. Tan, Y. Ishikuro, Y. Hosoi, N. Yamane, P. Ai, P. Zhang, G. Yang, M. Wu, R. Yang, N. Tsubaki, PPh3 functionalized Rh/rGO catalyst for heterogeneous hydroformylation: Bifunctional reduction of graphene oxide by organic ligand, Chem. Eng. J. 330 (2017) 863–869. https://doi.org/https://doi.org/10.1016/j.cej.2017.08.023.

[117] M. Tan, G. Yang, T. Wang, T. Vitidsant, J. Li, Q. Wei, P. Ai, M. Wu, J. Zheng, N. Tsubaki, Active and regioselective rhodium catalyst supported on reduced graphene oxide for 1-hexene hydroformylation, Catal. Sci. Technol. 6 (2016) 1162–1172. https://doi.org/10.1039/C5CY01355K.

[118] J.A. Farmer, C.T. Campbell, Ceria maintains smaller metal catalyst particles by strong metal-support bonding, Science (80). 329 (2010) 933. https://doi.org/10.1126/science.1191778.

[119] G.R. Jenness, J.R. Schmidt, Unraveling the role of metal−support interactions in heterogeneous catalysis: Oxygenate selectivity in Fischer−Tropsch Synthesis, 4,(2014),1563.

[120] H. Wan, B. Wu, H. Xiang, Y. Li, Fischer-Tropsch Synthesis: Influence of support incorporation manner on metal dispersion, metal-support interaction, and activity of iron catalysts, ACS Catal. 2 (2012) 1877–1883. https://doi.org/10.1021/cs200584s.

[121] R. Thalinger, T. Götsch, C. Zhuo, W. Hetaba, W. Wallisch, M. Stöger-Pollach, D. Schmidmair, B. Klötzer, S. Penner, Rhodium-catalyzed methanation and methane steam reforming reactions

on rhodium–perovskite systems: Metal–support interaction, ChemCatChem. 8 (2016) 2057–2067. https://doi.org/10.1002/cctc.201600262.

[122] T.W. van Deelen, C. Hernández Mejía, K.P. de Jong, Control of metal-support interactions in heterogeneous catalysts to enhance activity and selectivity, Nat. Catal. 2 (2019) 955–970. https://doi.org/10.1038/s41929-019-0364-x.

[123] M. Ahmadi, H. Mistry, B. Roldan Cuenya, Tailoring the catalytic properties of metal nanoparticles via support interactions, J. Phys. Chem. Lett. 7 (2016) 3519–3533. https://doi.org/10.1021/acs.jpclett.6b01198.

[124] Y. Tang, J. Lai, Y. Chao, M. Luo, F. Lin, J. Zhou, D. Su, Strengthening reactive metal-support interaction to stabilize high-density Pt single atoms on electron-deficient g-C_3N4 for boosting photocatalytic H_2 production Peng, (2018). https://doi.org/10.1016/j.nanoen.2018.11.033.

[125] S. Penner, M. Armbrüster, Formation of intermetallic compounds by reactive metal–support interaction: A frequently encountered phenomenon in catalysis, ChemCatChem. 7 (2015) 374–392. https://doi.org/10.1002/cctc.201402635.

[126] C.-J. Pan, M.-C. Tsai, W.-N. Su, J. Rick, N.G. Akalework, A.K. Agegnehu, S.-Y. Cheng, B.-J. Hwang, Tuning/exploiting strong metal-support interaction (SMSI) in heterogeneous catalysis, J. Taiwan Inst. Chem. Eng. 74 (2017) 154–186. https://doi.org/https://doi.org/10.1016/j.jtice.2017.02.012.

[127] C. Hernández Mejía, T.W. van Deelen, K.P. de Jong, Activity enhancement of cobalt catalysts by tuning metal-support interactions, Nat. Commun. 9 (2018) 1–8. https://doi.org/10.1038/s41467-018-06903-w.

[128] T.U. A. Maeda, F. Yamakawa, Effect of strong metal-support interaction (SMSI) on ethylene hydroformylation over niobia-supported palladium catalysts, Catal Lett. 4 (1990) 107–112.

[129] H. Xiong, L.L. Jewell, N.J. Coville, Shaped carbons as supports for the catalytic conversion of syngas to clean fuels, ACS Catal. 5 (2015) 2640–2658. https://doi.org/10.1021/acscatal.5b00090.

[130] Y. Zhang, H.-B. Zhang, G.-D. Lin, P. Chen, Y.-Z. Yuan, K.R. Tsai, Preparation, characterization and catalytic hydroformylation properties of carbon nanotubes-supported Rh–phosphine catalyst, Appl. Catal. A Gen. 187 (1999) 213–224. https://doi.org/10.1016/S0926-

860X(99)00229-X.

[131] H. Zhang, Y. Zhang, G. Lin, Y. Yuan, K.R. Tsai, Carbon nanotubes-supported Rh-phosphine complex catalysts for propene hydroformylation, Studies in Surface Science and Catalysis. (2010) 3885–3890.

[132] J. Qiu, H. Zhang, X. Wang, B. Yin, Hydroformylation of 1-octene over carbon nanotube supported cobalt catalyst, ACS Div. Fuel Chem. Prepr. 49 (2004) 940–941.

[133] H. Sakagami, N. Ohta, S. Endo, T. Harada, N. Takahashi, Location of active sites for 3-pentanone formation during ethene hydroformylation on Rh/active-carbon catalysts, J. Catal. 171 (1997) 449–456.

[134] X. Song, Y. Ding, W. Chen, W. Dong, Y. Pei, J. Zang, L. Yan, Y. Lu, Formation of 3-pentanone via ethylene hydroformylation over Co/activated carbon catalyst, Appl. Catal. A Gen. 452 (2013) 155–162. https://doi.org/10.1016/j.apcata.2012.11.006.

[135] B. Li, X. Li, K. Asami, K. Fujimoto, Low-pressure hydroformylation of middle olefins over Co and Rh supported on active carbon catalysts, Energy Fuels. 17 (2003) 810–816.

[136] R. Gao, C.D. Tan, R.T.K. Baker, Ethylene hydroformylation on graphite nanofiber supported rhodium catalysts, Catal. Today. 65 (2001) 19–29. https://doi.org/10.1016/S0920-5861(00)00541-1.

[137] T.A. Kainulainen, M.K. Niemelä, A.O.I. Krause, Rh/C catalysts in ethene hydroformylation: The effect of different supports and pretreatments, J. Mol. Catal. A Chem. 140 (1999) 173–184. https://doi.org/10.1016/S1381-1169(98)00223-4.

[138] C.J.K. Weststrate, D. Sharma, D.G. Rodriguez, M.A. Gleeson, H.O.A. Fredriksson, J.W.H. Niemantsverdriet, Mechanistic insight into carbon-carbon bond formation on cobalt under simulated Fischer-Tropsch synthesis conditions, Nat. Commun. (2020). https://doi.org/10.1038/s41467-020-14613-5.

[139] M. Claeys, E. van Steen, Basic studies, Elsevier B.V., 2004. https://doi.org/10.1016/S0167-2991(04)80465-8.

[140] C.J.W.D. Sharma, D.G. Rodriguez, M.A. Gleeson, H.O.A. Fredriksson, J.W. Niemantsverdriet, Reactivity of - C_3H_x adsorbates in presence of Co^- adsorbed CO and hydrogen: Testing Fischer–Tropsch chain growth mechanisms, Top. Catal. (2020).

https://doi.org/10.1007/s11244-020-01306-y.

[141] M.M.G. R. A. van Santen, I. M. Ciobica, E. van Steen, Mechanistic issues in Fischer–Tropsch catalysis, 2011. https://doi.org/10.1016/B978-0-12-387772-7.00003-4.

[142] S. Mousavi, A. Zamaniyan, M. Irani, M. Rashidzadeh, Generalized kinetic model for iron and cobalt based Fischer–Tropsch synthesis catalysts: Review and model evaluation, Applied Catal. A, Gen. 506 (2015) 57–66. https://doi.org/10.1016/j.apcata.2015.08.020.

[143] F.E. Paulik, Recent developments in hydroformylation catalysis, Catal. Rev. 6 (1972) 49-. https://doi.org/10.1080/01614947208078691.

[144] W. Dong, J. Liu, H. Zhu, Y. Ding, Y. Pei, J. Liu, H. Du, M. Jiang, T. Liu, H. Su, W. Li, Co–Co 2 C and Co–Co_2 C/AC catalysts for hydroformylation of 1-hexene under low pressure: Experimental and theoretical studies, J. Phys. Chem. C. 118 (2014) 19114–19122. https://doi.org/10.1021/jp504215y.

[145] E.S.P.B. V, J.H. Boelee, K. van der Wiele, Influence of reaction conditions on the effect of Co-feeding ethene in the Fischer-Tropsch Synthesis on a fused-iron catalyst in the liquid phase, Appl. Catal. 53 (1989) 1–13.

[146] G. Prefectural, I. Technology, Enhancement of propene formation by Co-feeding ethene and synthesis gas on Co / SiO_2 catalyst, Transaction of the Materials Research Society of Japan, 390 (2009) 387–390.

[147] A.I. McNab, A.J. McCue, D. Dionisi, J.A. Anderson, Combined quantitative FTIR and online GC study of Fischer-Tropsch synthesis involving co-fed ethylene, J. Catal. 362 (2018) 10–17. https://doi.org/10.1016/j.jcat.2018.03.026.

[148] C.J. Weststrate, J.W. Niemantsverdriet, CO as a promoting spectator species of CxHy conversions relevant for Fischer–Tropsch chain growth on cobalt: Evidence from temperature-programmed reaction and reflection absorption infrared spectroscopy, ACS Catal. 8 (2018) 10826–10835. https://doi.org/10.1021/acscatal.8b02743.

Chapter 3: Experimental

3.1 Introduction

Experiment results are significantly influenced by the experiment design and laboratory set-up. The performance of heterogeneous ethene hydroformylation (EH) and Fischer-Tropsch synthesis (FTS) could differ, depending on various factors and parameters, such as material, catalyst preparation, reactor system, operating conditions and product analysis. Cobalt was supported by reduced graphene oxide (RGO) with and without a rhodium promoter, and the catalyst performance of EH and FTS was tested in a tubular fixed bed reactor (TFBR). The feed-gas of EH is $CO/H_2/C_2H_4$ and the feed-gas of FTS is CO/H_2. The products of EH are hydrocarbons, propanol and propionaldehyde, while the products of FTS are hydrocarbons and alcohols. The data on EH were collected after the reaction reached a steady state. In order to get more insight into the relationship between EH and FTS, a special experiment known as a cycle of EH and FTS was carried out and the data were collected at certain reaction time intervals. As the reaction regimes of heterogeneous EH and FTS and their product distribution are so complex, special attention was paid to the handling of these parameters. The results were intended to provide reliable technical information that could contribute to improving the design of industrial EH and FTS processes.

In this chapter, the general procedures and a description of the equipment used are provided. In order to investigate different aspects of EH and FTS, various experiments were designed and more details are provided in each chapter. The methods for catalyst characterization and original data processing are also detailed in this section.

3.2 Materials and Chemicals

3.2.1 Gases

All the gases used in the experiments were purchased from AFROX (African Oxygen Ltd). The gas composition/purity of each cylinder was certified and indicated with a label on the cylinder body. The

carrier gases for all the gas chromatographs (GC) were ultra-high purity (UHP) grades (>99.997). More detailed information is as follows:

1. Two kinds of gas mixtures were used for the reaction, namely (UHP) $CO/H_2/N_2$ and (UHP) C_2H_4/N_2. The mole ratios (%) of the gas mixture were:

   $CO/H_2/N_2$: $CO : H_2 : N_2 = 30 : 60 : 10$.

   C_2H_4/N_2: $C_2H_4 : N_2 = 50 : 50$.

2. Five pure gases were used. UHP N_2 was used to purge and test the leakage of the reactor system. UHP C_2H_4 and CO were used for the reaction. UHP H_2 was used for both catalyst reduction and the reaction. UHP Ar was used as the compensation gas when the feed-gas ratios experiment for EH was carried out.
3. The mole ratios (%) of the calibration gas mixtures are indicated in Table 3.1.

Table 3.1 Mole ratios (%) of the calibration gas mixtures

CH_4	C_2H_4	C_2H_6	N_2	CO	CO_2	H_2
2.5	0.25	0.44	10.5	30.8	5.9	49.61

4. Four pure gases were used for GC. UHP He and UHP Ar were used as carrier gases in the thermal conductivity detector (TCD). For the flame ionization detector (FID), UHP H_2 and UHP air were used for the flame, while Ar was used as the carrier gas.

3.2.2 Chemicals

The metals used in this study were cobalt and rhodium supported by RGO and titania. Except Rhodium chloride ($RhCl_3 \cdot 3H_2O$) was purchased from Maclin Co. Ltd, while all other chemicals were supplied by Sinopharm Chemical Reagent Co. Ltd.

3.3 Experiment Set-up

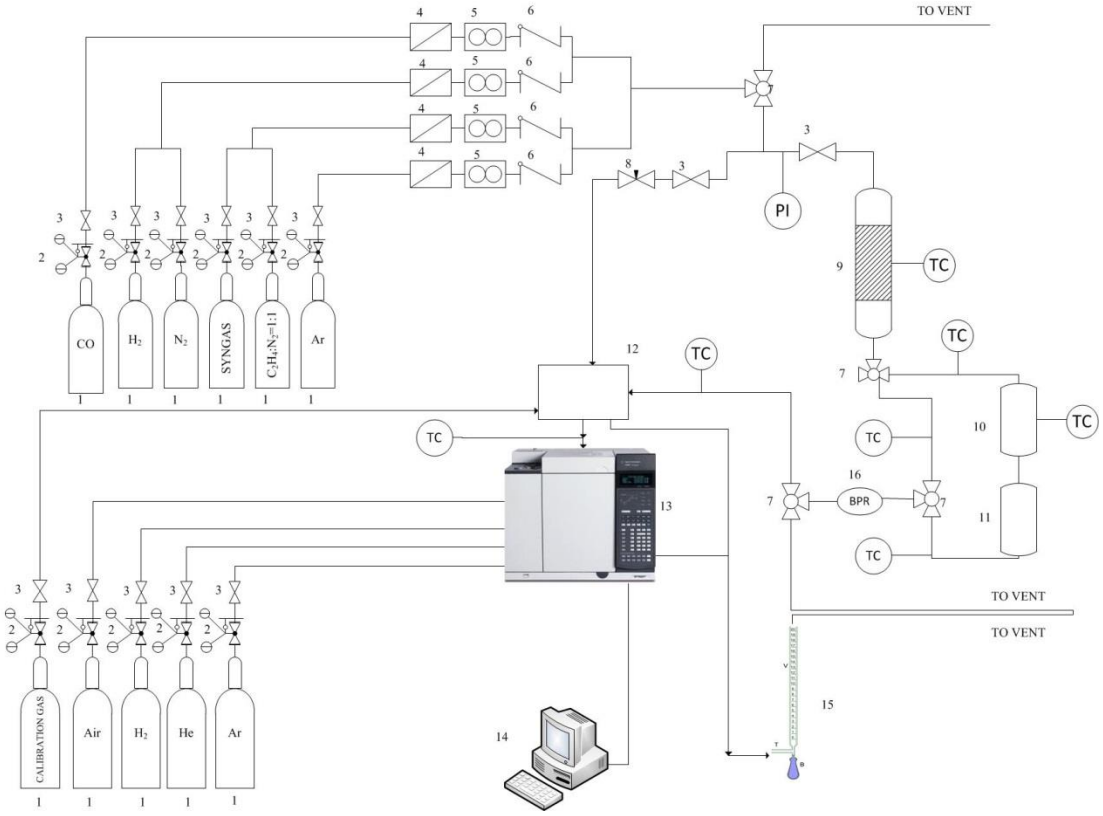

Equipment used: 1 - gas cylinders; 2 - pressure regulators; 3 - shut-off valves; 4 - one-way valves; 5 - mass flow controllers; 6 - needle valves; 7 - three-way valves; 8 - needle valve; 9 - FBR; 10 - hot condensable product trap; 11 - cold condensable product trap; 12 - multi-valve box; 13 - on-line GC; 14 - computer for data collection; 15 - bubble meter; 16 - back pressure regulator.

Figure 3.1 Experiment set-up

All the EH, FTS and cycles of the EH and FTS experiments were carried out in a TFBR using different catalysts. The equipment used for the reaction and product analysis is shown in Figure 3.1.

Information on the gases used is provided in Section 3.2.1. The feed-gas flow rate was controlled by means of a mass flow controller (Brooks 5850 instrument). The catalyst was loaded into the reactor and the top and bottom of the catalyst was filled with ceramic balls. (The structure of the catalyst bed is detailed in Section 3.5.) The feed-gas was pre-heated by the ceramic balls packed on top of the catalyst bed, then the products and un-reacted reactent gases passed through the bottom of the reactor column. For the EH reaction, the tail gases passed through a tube tail gas line to a back pressure regulator (Swagelock) with heat tape to keep the temperature at 180 ℃. For FTS, the tail gas passed a tail gas line with a hot trap (to maintain temperature at 150 ℃, as well as reactor pressure) and a cold trap (kept at room temperature and reactor pressure). After the joint of the two paths for

the tail gas, there was a back pressure regulator that was used to adjust the pressure in the reactor. When the tail gas passed through the back pressure regulator, the pressure of of the tail gases was reduced from the operating pressure to atmospheric pressure. The tail gases were then sent to the sampling loop (which maintained the temperature at 180 ℃) of an online GC (Agilent 7890B). To prevent condensation of products, all the tail gas lines were heated and kept at 180 ℃. After passing through the GC, the tail gases passed through a bubble meter (to test the tail gas flow rate) and then through the vent line for venting.

3.4 Catalyst Preparation and Characterization

Two kinds of catalysts were used: 20 wt.% Co/RGO; 0.5 wt.%Rh-20 wt.% Co/RGO (Co/Rh molar ratio is 69.8). Preparation of the RGO-based catalysts were used as a precipitation method. Details of the catalyst preparation procedure are provided in later chapters.

The morphology of the samples was captured by emission scanning electron microscopy (SEM) images, using Hitachi S-4800. Transmission electron microscopy (TEM) was carried out on a JEOL JEM-2000 microscope (200 kV). Thermo gravimetric analysis was done using a SDT Q600 thermo gravimetric analyzer. Powder X-ray diffraction (XRD) patterns were achieved using a Rigaku D/MAX-2500 XRD system (Cu Kα radiation, λ = 0.15406 nm) operated at 40 kV and 40 mA. H_2 temperature-programmed reduction (TPR) was carried out on a Zeton Altamira AMI-200 instrument. Prior to TPR measurement, the catalyst was flushed with Ar (> 99.999 %) at 150 °C for 1 h and then cooled to 50 °C. Subsequently, the temperature was raised from 50 to 800 °C with a ramp of 10 °C min^{-1} under H_2 / Ar (volume ratio 1 / 9, flow rate 30 mL min^{-1}). The temperature was finally maintained at 800 °C for 30 min. The H_2 concentration was monitored by means of a TCD. The H_2-TPR profile was recorded as H_2 consumption versus reduction temperature. Raman spectroscopy was obtained using a Horiba Scientific LabRAM HR Evolution instrument using 514 nm and 532 nm laser lines.

3.5 Reactor System

A fixed bed reactor (FBR) was used for heterogeneous EH to produce aldehyde and alcohol. The feed-gas flowed downward through the catalyst bed in a profile approximating that of a plug flow.

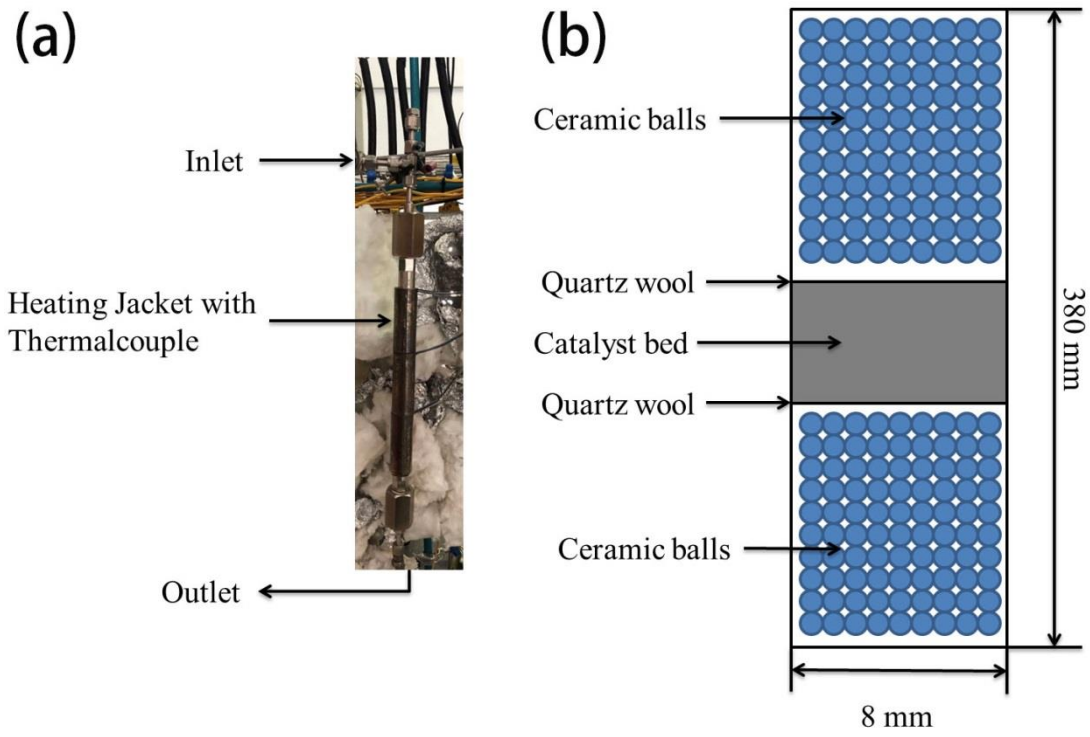

Figure 3.2 FBR showing: (a) a digital portrait of FBR; (b) a sketch of the catalyst loading design.

Figure 3.2 shows two of the same kind of FBR equipment used for all the experiments done in this study. The stainless steel reactors have an internal diameter of 8 mm and a tube length of 380 mm. The heating jacket with thermal couple was used to adjust and maintain the operating temperature. The ceramic balls on top of the catalyst bed was used to pre-heat the feed-gas, while the ceramic balls at the bottom of reactor supported the catalyst bed. The quartz wool placed at the top and the bottom of the catalyst bed was used to cushion the catalyst.

3.6 Product Analysis

The analytical equipment was required to meaure the propinoaldehyde and propinol, hydrocarbons, the inorganic component in reaction regime and the internal standard gas N_2. The tail gas was analyzed every 4 hours with an online Agliant 7890B GC. An FID was used to analyze propinoaldehyde, propinol and short-chain hydrocarbons. N_2, H_2, CO, CO_2 were analyzed using two TCDs.

3.6.1 Online GC stytem

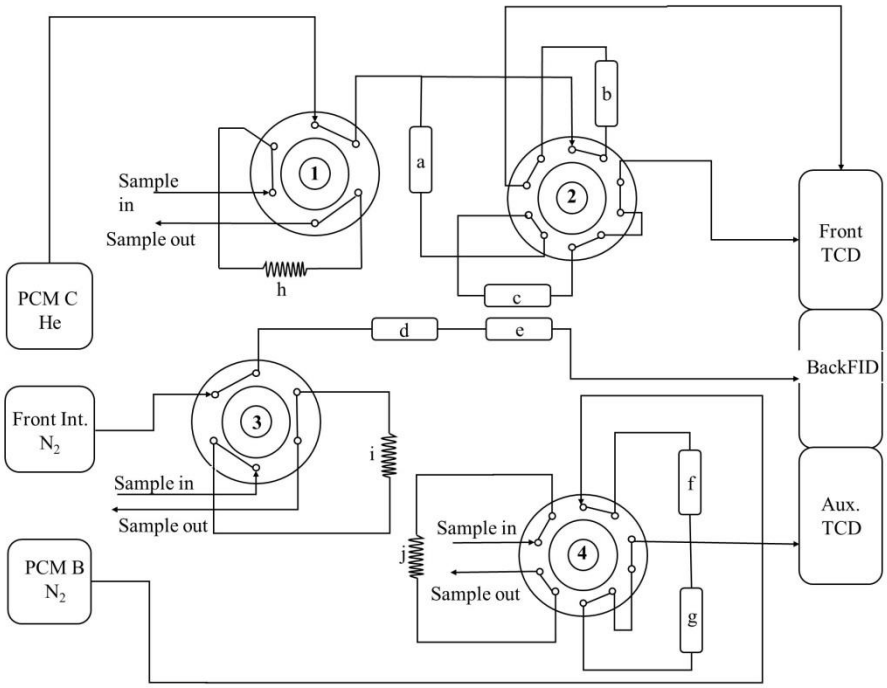

Figure 3.3 The sampling flow scheme for the online GC\; (a) – delay part; (b) and (f) - Mole Sieve 13 X column; (c) – Heyasep Q column; (d) – splitter; l–- LTM system with a CP-Sil 5 CB column; (g)–- Plot Q column; (h), (i) and (j) - sampling loops.

The tail gas from the FBR were sent to the GC sampling loops through a heated line (180 ℃). The gas entered the GC through three multiple sampling valves that were heated to 150 ℃. The temperature of the TCD and FID was kept at 250 ℃. The sampling flow scheme for the online GC is shown in Figure 3.3. Detailed infromation on the columns, carrier gas and oven temperature is provided in Table 3.2. Typical EH product chromatogram of the FID and TCD are shown in Figure 3.4. Typical FTS with alcohols product chromatograms of the FID and TCD are shown in Figure 3.5.

Table 3.2 Parameters of the online GC

Online GC	**Agilent 7890B**
Back Detector	FID2 B, T = 250 °C
Column 1	CP-SIL 5 CB (25 m x 150 µm x 2 µm)
Sample valve temperature	150 °C

Flame gas	Air with a flow rate of 40 ml(NTP)/min and UHP H2 with a flow rate of 400 ml(NTP)/min
Carrier gas	UHP Ar with a flow rate of 25 ml(NTP)/min
Oven temperature programme	35 °C for 3 min then 10 °C/min to 250 °C for 60 min
Product analysis	Hydrocarbons, propinoaldehyde and propinol
Front Detector	TCD1 A, T = 250 °C
Column 2	HAYESEP Q 100/120 mesh, 1 m, 1 mm ID
Column 3	13X Mole Sieve 80/100 mesh, 1m, 1 mm ID
Sample valve temperature	150 °C
Carrier gas	UHP He with a flow rate of 20 ml(NTP)/min
Oven temperature programme	50 °C for 5 min, then 10 °C/min to 80 °C for 0 min, then 25 °C/min to 200 °C for 25 min
Product analysis	N_2, CO, CH_4, CO_2
Aux Detector	TCD3 C, T = 250 °C
Column 3	13X mole sieve 80/100 mesh, 1m, 1 mm ID
Column 4	Plot Q
Sample valve temperature	150 °C
Carrier gas	UHP Ar with a flow rate of 20 ml(NTP)/min
Oven temperature programme	50 °C for 5 min, then 10 °C/min to 80 °C for 0 min, then 25 °C/min to 200 °C for 25 min
Product analysis	H_2

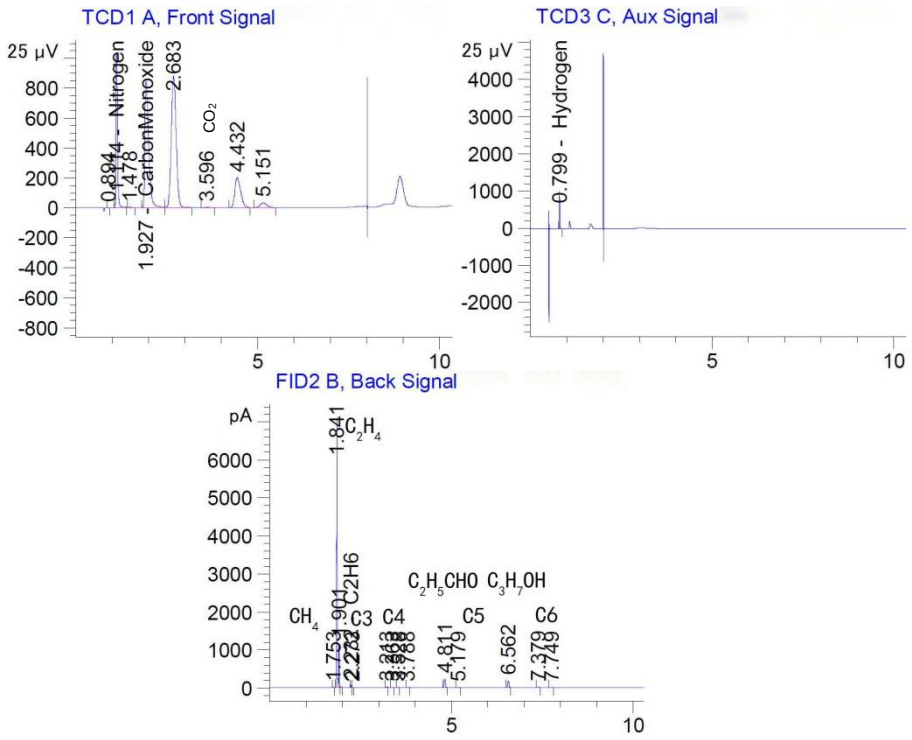

Figure 3. 4 Typical online analysis of EH

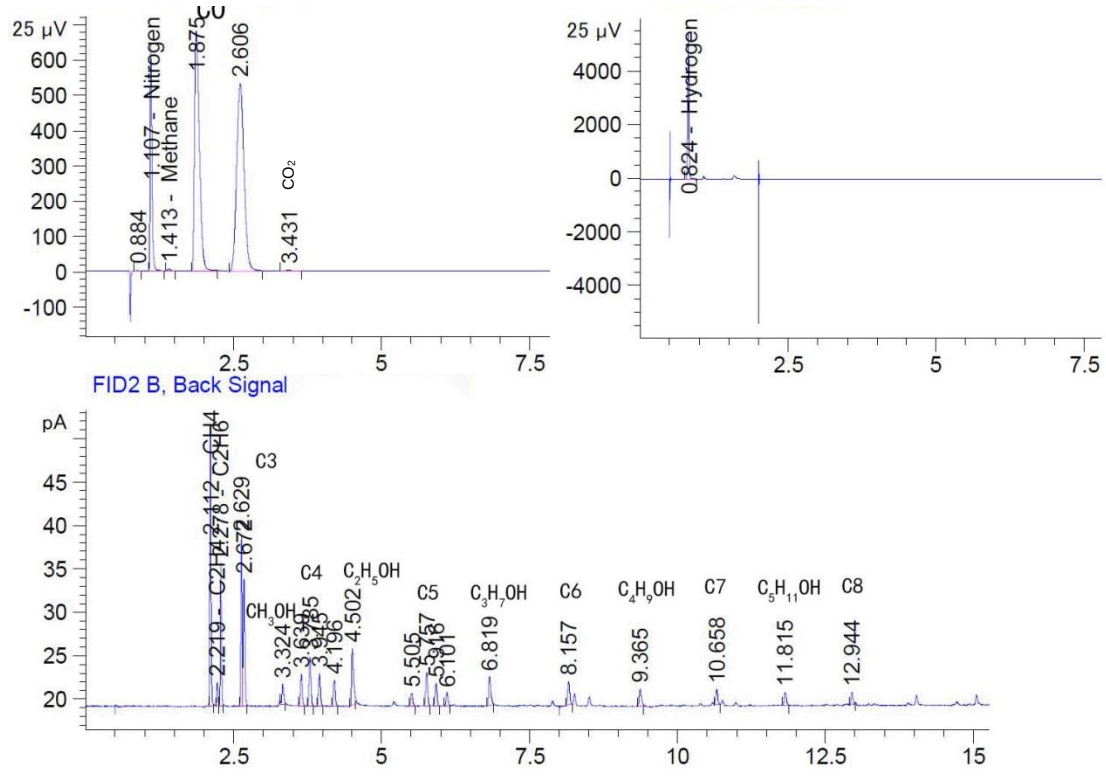

Figure 3. 5 Typical online analysis of FTS in Chapter 4

3.7 Calculations

3.7.1 Mole percentage

The mole composition of each component in the feed-gas and tail-gas was calculated using the data from the online GC. The mixture of feed-gas or tail-gas was separated by the columns and detected by TCDs and FIDs. The signal of each component was recorded as a peak and then the mole fraction of each component was calculated using the peak area based on the results of calibration gas. The calibration gas - a mixture of N_2, H_2, CO, CO_2, CH_4, C_2H_4 and C_2H_6, as described in Section 3.2.1 - was used to calibrate the response of the TCD and FID twice a week. The hydrocarbon product areas obtained from the FID were corrected by C_2H_4 (for olefins) and C_2H_6 (for paraffins) using the response factors based on the data reported by Dietz and Scanlon.[1,2] The response factors for C1-5 alcohols and propionaldehyde were obtained using the normalization method and corrected based on C_2H_4. The molar response factors are listed in Table 3.3.

Table 3.3 Molar response factors for hydrocarbons and oxygenates

Hydrocarbon carbon number	Olefin	Paraffin
2	1	1
3	0.7	0.74
4	0.55	0.55
Oxygenates	**Based on C_2H_4**	
CH_3OH	3.27	
C_2H_5OH	2.25	
C_2H_5CHO	1.02	
C_3H_7OH	1.29	
C_4H_9OH	1.58	
$C_5H_{11}OH$	1.19	

The molar percentage of a component in the feed-gas or tail-gas was calculated as follows:

$$P_{x,gas}\% = \left(\frac{A_{x,gas}}{A_{x,cal}}\right) \times P_{x,cal}\% \qquad (3.1)$$

Where: $P_{x,gas}\%$ is the molar percentage of component x in the analysed gas; $A_{x,gas}$ is the integrated area of the peak from the GC detector corresponding to component x in the analysed gas; $A_{x,cal}$ is the integrated area of the peak from the GC detector that corresponds to component x in the calibration gas; $P_{x,cal}\%$ is the molar percentage of component x in the calibration gas.

For components not included in the calibration gas, the molar percentage of the component was calculated using the reference component and relative molar response factors listed in Table 3.2. The following equation was used:

$$P_{x,gas}\% = \left(\frac{A_{x,gas} \times RF_{x,y}}{A_{y,cal}}\right) \times P_{y,cal}\% \quad (3.2)$$

Where: $P_{x,gas}\%$ is the molar percentage of component x in the analysed gas; $A_{x,gas}$ is the integrated area of the peak from the GC detector that corresponds to component x in the analysed gas; $RF_{x,y}$ is the relative response factor of component x in the analysed gas, based on the reference component y in the calibration gas; $A_{y,cal}$ is the integrated area of the peak from the GC detector the corresponds to the reference component y in the calibration gas; $P_{y,cal}\%$ is the molar percentage of component y in the calibration gas. C_2H_4 was used as the reference for olefins and oxygenates, while C_2H_6 was used as the reference for paraffins.

3.7.2 Mass balance

The volumetric flow rate of the feed-gas was controlled by the mass flow controllers, from which the flow rate of the tail-gas was calculated. N_2 in the feed-gas was used as the internal standard, as it is only present in both the feed-gas and tail-gas with a constant molar amount. Therefore, the outlet flow rate was determined using a N_2 balance. The N_2 balance across the reactor is defined as:

$$F_{in} \times P_{N_2,in} = F_{out} \times P_{N_2,out} \quad (3.3)$$

Where: F_{in} is the total molar flow rate of the feed-gas, mmol/h; F_{out} is the total molar flow rate of the reactor tail-gas, mmol/h; $P_{N_2,in}$ is the molar percentage of N_2 in the feed-gas; and $P_{N_2,out}$ is the molar percentage of N_2 in the tail-gas.

The molar flow rate of component x in the feed-gas or tail-gas can be calculated as follows:

$$F_{x,in} = F_{in} \times P_{x,in} \quad (3.4)$$

$$F_{x,out} = F_{out} \times P_{x,out} \quad (3.5)$$

Where: $F_{x,in}$ and $F_{x,out}$ are the molar flow rate of component x in feed-gas or tail-gas, mmol/h; $P_{x,in}$ and $P_{x,out}$ is the molar percentage of component x in the feed-gas or tail-gas, mmol/h; F_{in} is the total molar flow rate of the feed-gas, mmol/h; F_{out} is the total molar flow rate of the reactor tail-gas, mmol/h.

After the molar flow rate of every component in the feed-gas and tail-gas was calculated, the performance of the catalyst for FTS and EH was evaluated using parameters such as reactant reaction rate, reactant conversion, product selectivity and mass balance.

3.7.3 FTS calculations

- CO reaction rate:

$$-r_{CO} = \frac{F_{CO,in} - F_{CO,out}}{m_{cat}} \quad (3.6)$$

Where: $F_{CO,in}$ is the molar flow rate of CO in the feed-gas, mmol/h; $F_{CO,out}$ is the molar flow rate of CO in the tail-gas, mmol/h; m_{cat} is the mass of catalyst loaded into the reactor, g; r_{CO} is the reaction rate of CO, mmol/h/gcat.

- CO conversion:

$$CO_{conv} = \left(\frac{F_{CO,in} - F_{CO,out}}{F_{CO,in}}\right) \times 100\% \quad (3.7)$$

Where: $F_{CO,in}$ is the molar flow rate of CO in the feed-gas, mmol/h; $F_{CO,out}$ is the molar flow rate of CO in the tail-gas, mmol/h; CO_{conv} is CO conversion, %.

- Product selectivity:

$$S_{x,out} = \left(\frac{n \times F_{x,out}}{F_{CO,in} - F_{CO,out}}\right) \times 100\% \quad (3.8)$$

Where: $F_{x,out}$ is the molar flow rate of product x in the tail-gas, mmol/h; $F_{CO,in}$ is the molar flow rate of CO in the feed-gas, mmol/h; $F_{CO,out}$ is the molar flow rate of CO in the tail-gas, mmol/h; n is the carbon number in the product, x; $S_{x,out}$ is the selectivity of product x based on converted CO, %.

- Selectivity of other products:

$$S_{other} = 100 - \sum_1^4 S_{Hydrocarbons} - \sum_1^5 S_{Alcohols} \quad (3.9)$$

Where: S_{other} is the total selectivity of C_{5+} hydrocarbons and C_{6+} alcohols, %; $S_{Hydrocarbons}$ is the selectivity of hydrocarbons, %; $S_{Alcohols}$ is the selectivity of alcohols, %.

The FTS carbon mass balance was defined as the amount of carbon in feed-gas equals the amount of carbon in the tail-gas, with the acceptable error range being within 100±5%.

3.7.4 EH calculation

- Reaction rate:

$$-r_x = \frac{F_{x,in} - F_{x,out}}{m_{cat}} \quad (3.10)$$

Where: $F_{x,in}$ is the molar flow rate of component x in the feed-gas, mmol/h; $F_{x,out}$ is the molar flow rate of component x in the tail-gas, mmol/h; m_{cat} is the mass of catalyst loaded into the reactor, g; r_x is the reaction rate of component x, mmol/h/gcat; x is one of the components in the feed-gas (CO, H_2, C_2H_4).

- Conversion:

$$x_{conv} = \left(\frac{F_{x,in} - F_{x,out}}{F_{x,in}}\right) \times 100\% \quad (3.11)$$

Where: $F_{x,in}$ is the molar flow rate of component x in the feed-gas, mmol/h; $F_{x,out}$ is the molar flow rate of component x in the tail-gas, mmol/h; x_{conv} is the conversion of component x, %; x is one of the components in the feed-gas (CO, H_2, C_2H_4).

- Selectivity based on converted C_2H_4:

$$S_{x,C_2H_4} = \left(\frac{F_{x,out}}{F_{C_2H_4,in} - F_{C_2H_4,out}}\right) \times 100\% \quad (3.12)$$

Where: $F_{x,out}$ is the molar flow rate of product x in the tail-gas, mmol/h; $F_{C_2H_4,in}$ is the molar flow rate of C_2H_4 in the feed-gas, mmol/h; $F_{C_2H_4,out}$ is the molar flow rate of C_2H_4 in the tail-gas, mmol/h; S_{x,C_2H_4} is the selectivity of product x based on converted C_2H_4, %; x is C_2H_6 or C_2H_5CHO or C_3H_7OH.

- Selectivity based on total converted carbon from CO and C_2H_4:

$$S_{x,carbon} = \left[\frac{n \times F_{x,out}}{2 \times (F_{C_2H_4,in} - F_{C_2H_4,out}) + (F_{CO,in} - F_{CO,out})}\right] \times 100\% \quad (3.13)$$

Where: $F_{x,out}$ is the molar flow rate of product x in the tail-gas, mmol/h; $F_{C_2H_4,in}$ is the molar flow rate of C_2H_4 in the feed-gas, mmol/h; $F_{C_2H_4,out}$ is the molar flow rate of C_2H_4 in the tail-gas, mmol/h; $F_{CO,in}$ is the molar flow rate of CO in the feed-gas, mmol/h; $F_{CO,out}$ is the molar flow rate of CO in the tail-

gas, mmol/h; n is the carbon number in product x; $S_{x,carbon}$ is the selectivity of product x based on total converted carbon from CO and C_2H_4, %; x is C_2H_6 or C_2H_5CHO or C_3H_7OH.

- Selectivity based on converted CO:

$$S_{x,CO} = \left(\frac{F_{x,out}}{F_{CO,in} - F_{CO,out}}\right) \times 100\% \quad (3.14)$$

Where: $F_{x,out}$ is the molar flow rate of product x in the tail-gas, mmol/h; $F_{CO,in}$ is the molar flow rate of CO in the feed-gas, mmol/h; $F_{CO,out}$ is the molar flow rate of CO in the tail-gas, mmol/h; $S_{x,CO}$ is the selectivity of product x based on CO, %; x is C_2H_6 or C_2H_5CHO or C_3H_7OH.

The EH carbon mass balance was defined as the amount of carbon in feed-gas equals the amount of carbon in the tail-gas, with the acceptable error range being within 100±5%.

References

[1] W.A. Dietz, Response factors for gas chromatographic analyses, J. Chromatogr. Sci. 5 (1967) 68–71. https://doi.org/10.1093/chromsci/5.2.68.

[2] J.T. Scanlon, D.E. Willis, Calculation of flame ionization detector relative response factors using the eEffective carbon number concept, J. Chromatogr. Sci. 23 (1985) 333–340. https://doi.org/10.1093/chromsci/23.8.333.

Chapter 4: Insight into the Role of Co_2C supported on reduced graphene oxide in Fischer-Tropsch synthesis and ethene hydroformylation

Abstract

The role of Co_2C supported on reduced graphene oxide (RGO) for both the Fischer-Tropsch synthesis (FTS) and ethene hydroformylation (EH) reactions were investigated for the first time in this study. Two catalysts - cobalt supported by RGO (CG) and Rh-promoted cobalt supported by RGO (RCG) - were successfully synthesized. A series of experiments were performed wherein the feed was switched between syngas and a syngas–ethene mixture. During H_2 reduction: metallic Co was formed for the CG catalyst; however, Co_2C was detected in the RCG catalyst, which proved experimentally that RGO was the carbon source for the formation of Co_2C. After H_2 reduction, both the CG and RCG catalyst exhibited extremely low Fischer-Tropsch (FT) reactivity. This indicates that the interaction between Co and RGO limited the FT chain growth reaction.

The catalyst characterization results proved that exposure of the CG and RCG catalysts to syngas and/or a syngas-ethene mixture could transform CoO and/or metallic Co to Co_2C. It was found that the Co-Co_2C interface derived from the CG catalyst was inactive for FTS and exhibited low CO conversion, with the main products being short chain alcohols and hydrocarbons (C_1-C_4). Nevertheless, exposing the Co-Co_2C interface to the CO/C_2H_4/H_2 feed promoted the production of C_3 oxygenates, which indicated that the multi-phase of Co-Co_2C was highly active for EH. Moreover, a pure Co_2C phase was obtained with the promotion of Rh, which was completely inactive for FTS but highly active for EH. It was concluded that the interaction between RGO and cobalt species could suppress CO chain growth reaction, while promoting the CO insertion reaction to form aldehydes or alcohols.

4.1 Introduction

Hydroformylation, or OXO synthesis, was discovered by Otto Roelen in 1938, and is an important process used for the production of aldehydes.[1] Aldehydes are useful intermediates in the production

of valuable products such as alcohols, carboxylic acids, amines and diols. Currently, hydroformylation is widely used in the fine chemicals and pharmaceutical industries for the production of drugs, vitamins, herbicides and perfumes.[2] Hydroformylation is currently normally achieved through a homogenous process used by the industry. Although the homogenous process shows impressive activity and selectivity, the main disadvantage is that separating the products from the catalyst is a complicated process.[3–5] Hence a heterogeneous process is more desirable from an operational viewpoint. Research into heterogeneous EH would help to gain more understanding of the mechanism of hydroformylation and provide useful information that could be used in the development of a heterogeneous hydroformylation process that is low cost but high in efficiency.[1,6]

Graphene has become a well-known material in the past 16 years, since it was experimentally discovered in 2004 by Novoselov et al.[7] Many researchers have investigated the unique properties of graphene, and it has wide application in many fields, such as heterogeneous catalysis, electrochemical catalysis, adsorption and sensors, etc.[8,9] Graphene has many unique properties, including: high electron mobility at room temperature (250,000 cm^2/Vs); exceptional thermal conductivity (5000 $Wm^{-1}K^{-1}$); superior mechanical properties, with a Young's modulus of 1 tPa; and a high theoretical specific surface area (2600 m^2/g). This means that it is potentially an ideal substrate for use as a catalyst support.[10]

Hasin synthesised Co_2C by means of thermal reduction of a graphene oxide (GO)/Co_3O_4 nanocomposite with a 5% H_2/N_2 gas mixture (110 ml/min) at 200 ℃ for 1 h.[11] Meganathan prepared Co_2C/RGO by calcinating Co_3O_4/GO with ammonia (NH_3) gas at 400℃ for 5 h, where RGO refers to reduced graphene oxide.[12] These experimental results indicate the potential for the formation of Co_2C from RGO-supported cobalt oxide by calcination or activation of the catalyst using different atmospheres.

Cobalt carbide was identified as a surface species in research on FTS.[13] Early studies reported that cobalt carbide is neither an intermediate nor a catalytically active site for the FT reaction, but it does have a significant influence on CO reactivity and product selectivity.[14] Co_2C with (101) and (020)

facets exhibits high selectivity for the formation of lower olefins and has lower selectivity to methane.[15] The formation of Co_2C during FTS also increases selectivity to oxygenates, especially that of higher alcohols.[16,17]

Very little work has been reported on the performance of Co_2C in hydroformylation. However, Dong et al. reported that an unsupported Co−Co_2C catalyst and active carbon supported Co−Co_2C (Co−Co_2C/AC) catalysts are active for 1-hexene hydroformylation under pressure of 3.0 mPa and a temperature of 453 K.[18] Density Functional Theory (DFT) calculations (when using ethylene as a model hydroformylation reaction) indicated the possibility of Co_2C catalysed EH and was used to understand the nature of the 1-hexene hydroformylation catalytic reaction.[18] To the best of our knowledge, Co_2C catalysed EH has not been demonstrated experimentally as yet.

DFT calculations also show that although CO adsorbs strongly on stoichiometric and carbon-rich Co_2C surfaces, such as (110) and (111) facets, the energy barrier for subsequent CO direct dissociation is very high, which could lead to non-dissociative adsorption of CO on Co_2C. This limits its overall activity towards CO direct dissociation, but enhances the production of oxygenates from syngas via the CO insertion mechanism.[19] It can be deduced that Co_2C with (110) and (111) facets is possibly active for EH, as CO is non-dissociatively adsorbed on these facets. Rh used as a hydroformylation catalyst was developed many years ago, [20] but one disadvantage of Rh is that it is too expensive.[1] It would be interesting to investigate the catalytic performance of a cobalt catalyst promoted by a trace amount of Rh for both the FT and hydroformylation reactions. However, to the best of our knowledge, no such research has been done as yet.

With the aim of investigating the roles of Co_2C and the effect of the interaction between cobalt species and RGO on FTS and EH, groups of experiments were conducted involving switching from syngas to syngas co-feeding with ethene over two catalysts (cobalt supported by RGO (CG) and Rh-promoted cobalt supported by RGO (RCG)). A multi Co-Co_2C phase and a pure Co_2C phase supported on RGO were obtained during treatment of the catalyst with H_2 and syngas/ethene, and their catalytic performance is compared and discussed in the present work.

4.2 Materials and Methods

4.2.1 Preparation of 20%Co/RGO (CG)

GO was synthesized using a modified Hummer`s method.[21,22] 10 g of graphite was added to 230 ml of 95% H_2SO_4, and the mixture was stirred for 30 min in an ice-water bath. Then, 50 g of $KMnO_4$ was slowly added to the mixture over a period of 2 h, and the mixture was then stirred for 1 h. The ice water was then removed, and the mixture was allowed to settle at room temperature for about 16 h. The mixture was then mixed with ice obtained from an H_2O_2 aqueous solution (5 ml 30% H_2O_2 in 100 ml deionized water). The colour of the mixture changed to golden. After removing the residual metal ions, the mixture was centrifuged and washed with deionized water until the pH value was equal to that of the deionized water. The concentration of the GO solution obtained was 13.86 mg/ml.

A 346 ml GO solution (4.8 g GO) was treated by ultrasound for 30 min. Then 10 ml of a solution of 5.06 g $Co(Ac)_2 \cdot 4H_2O$ was added. After it was treated by ultrasound for 30 min, the pH of the solution was adjusted to 10, and 2 ml hydrazine hydrate was added to the solution. The solution was again treated by ultrasound for another 30 min, and the solution was then moved to a Teflon-lined stainless steel autoclave. The GO was reduced using the hydro-thermal method at 180 ℃ for 15 h. The obtained sample was dried at 80 ℃ and calcined at 400 ℃ for 5 h under an N_2 atmosphere.

4.2.2 Preparation of 0.5%Rh-20%Co/RGO (RCG)

When preparing the 0.5%Rh-20%Co/RGO catalyst, a similar preparation procedure was followed as indicated in item 2.1 above (for 20%Co/RGO). The only difference was that when adding 5.06 g of $Co(Ac)_2 \cdot 4H_2O$ to the GO solution, 0.08 g $RhCl_3 \cdot 3H_2O$ was also added to the GO solution. More details are provided in Section 4.2.1.

4.2.3 Characterization

The morphology of the samples was captured by emission scanning electron microscopy (SEM) images, using the Hitachi S-4800 equipment. Transmission electron microscopy (TEM) was carried out using a JEOL JEM-2000 microscope (200 kV). Powder X-ray diffraction (XRD) patterns were achieved using a

Rigaku D/MAX-2500 XRD system (Cu Kα radiation, λ = 0.15406 nm) operated at 40 kV and 40 mA. Raman spectroscopy was obtained using a Horiba Scientific LabRAM HR Evolution instrument and a 514 nm laser line.

4.2.4 Catalytic performance

The performance of the catalysts was evaluated using a fixed-bed reactor (FBR) with an internal diameter of 8 mm and a length of 380 mm. 0.5 g of 20%Co/RGO catalyst was loaded into the reactor and reduced with H_2 (AFROX - 99.999%) at 350 ℃ , 1 bar and 30 ml/min for 20 h. 0.5 g of 0.5%Rh-20%Co/RGO catalyst was loaded into the reactor and reduced with H_2 (AFROX - 99.999%) at 330 ℃ , 1 bar and 30 ml/min for 20 h. The FTS reactions were then done with syngas feed (SFT) and EH using syngas co-fed with ethene, and a number of different conditions were imposed. All the feed-gas, calibration gas and products were analysed using an online Agilent 7890B GC. The oxygenates and hydrocarbons were separated using a CP-Sil 5CB (25m x 0.15mm x 2.0 µm) column and analysed by means of a flame ionization detector (FID). The other gases were analysed by means of a thermal conductivity detector (TCD). Finally, the used catalyst was unloaded for purposes of further characterisation. The mass balance of each data point was with the range 100%±5%.

4.3 Results and Discussion

4.3.1 XRD

XRD was used to analyse the crystalline structure of the fresh and reacted catalyst. (See Figure 4.1.) In the patterns produced by both catalysts, the wide peak at

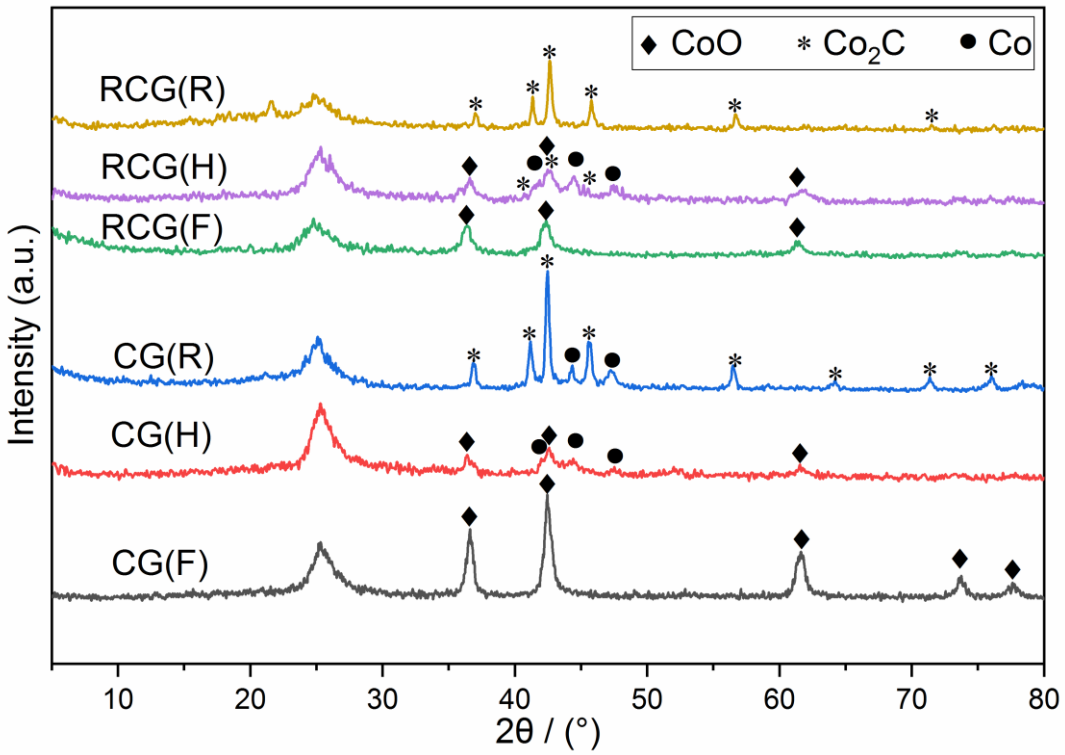

Figure 4.1 XRD patterns of fresh and spent catalysts. Cobalt/RGO (CG). Rh-Co/RGO (RCG). (F) - fresh catalyst; (H) - H_2 reduced catalysts; (R) - reacted catalysts.

around 26° is assigned to the amorphous peak of reduced GO. According to the JCPDS 48-1719 PDF card, the diffraction peaks at 36.49°, 42.39°, 61.50°, 73.67° and 77.53° correspond to CoO facets of (111), (200), (200), (311) and (222). Unlike that Co_3O_4 is the main phase for the calcined cobalt catalyst supported on TiO_2 [23], SiO_2 [24,25], Al_2O_3 [26], the XRD analysis proves that cobalt is present as CoO in both fresh CG (CG(F)) and fresh RCG (RCG(F)). Additionally, there was no Rh species detected because of the very low loading.

In the XRD pattern of H_2 reduced CG (CG (H)), the peaks at 41.98°, 44.40° and 47.52° are assigned to the Co (100), (002) and (101) facets (JCPDS 05-0727), while the peaks at 36.42°, 42.58° and 61.56° correspond to the CoO (111), (200) and (220) facets (JCPDS 65-2902). In the XRD pattern of H_2 reduced RCG (RCG(H)), the peaks at 41.88°, 44.50° and 47.48° are assigned to the Co (100), (002) and (101) facets (JCPDS 05-0727). In the pattern of RCG(H), the peaks at 36.58°, 42.48° and 61.50° correspond to the CoO (111), (200) and (200) facets, according to JCPDS 65-2902. The peaks at 41.52°, 42.70° and 45.56° are assigned to the Co_2C (020) (111) and (210) facets (JCPDS 05-0704). Therefore, with the promotion of Rh, Co_2C can be formed during the reduction of CoO supported on RGO in an H_2 atmosphere, which indicates that the RGO supplies the carbon for the formation of Co_2C.

In the XRD pattern of reacted CG(CG(R)), the peaks at 44.38°, 76.05° (JCPDS 15-0806) and 47.27°(JCPDS 05-0727) correspond to the Co (111), (220) and (101) facets. The other peaks are assigned to the Co_2C facets of (110), (101), (020), (111), (210), (121), (220), (002) and (301) (JCPDS 65-8206). However, in the pattern of reacted RCG (RCG(R)), the peaks are assigned to the Co_2C facets (011), (020), (111), (210), (121), (301) and (131) (JCPDS 05-0704). This means that after EH, the cobalt phase was changed from CoO to Co_2C without Co. It was observed that Co_2C/RGO was formed from CoO/RGO during the reactions under an atmosphere of CO/H_2 /(and/or) C_2H_4. Moreover, the addition of rhodium promoted the formation of Co_2C during the reaction, as the pure Co_2C phase was presented in RCG(R). (See Fig 4.1.)

4.3.2 SEM

SEM measurement was performed to investigate the morphology of fresh catalysts – see Figure 4.2 for the SEM images. The RGO displayed a disordered layer structure that formed a three-dimensional network, as per CG(F) and RCG(F). (See Figure 4.2 (a) and (c).) This is as per the XRD result that a wide peak at around 26° is assigned to the amorphous peak of reduced GO. CoO particles were uniformly dispersed in CG(F), but appeared to be sintered with each other due to the calcination, as indicated in Figure 2 (b). Curiously, CoO particles formed nanorods in RCG(F). The inset in Figure 4.2 (d) is a SEM-EDS mapping image of Rh in RCG. It indicates that Rh was indeed loaded to the RCG(F) catalyst.

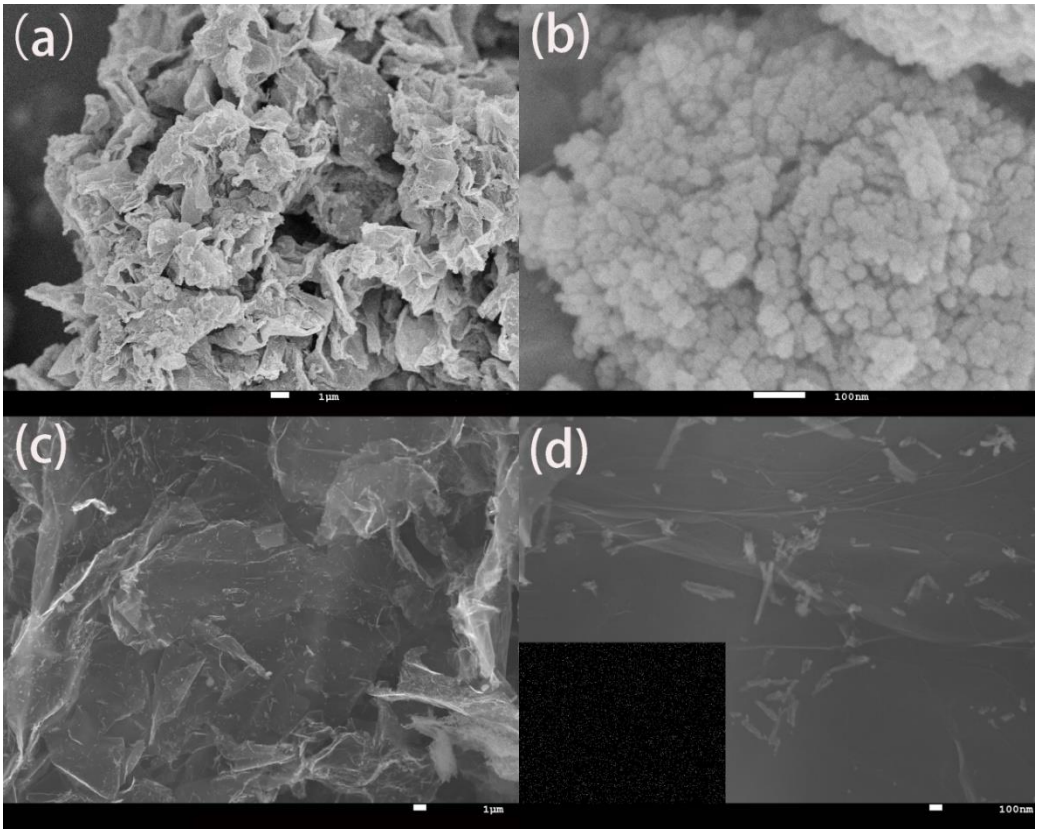

Figure 4.2 SEM images of fresh catalysts. CG(F) - (a) and–(b) RCG(F) - (c) and (d). Inset of 2 (d): SEM-EDS mapping images of Rh in–RCG(F). (F) – fresh catalyst; (R) - reacted catalysts.

4.3.3 TEM

The micro-structural and nano-structural features of the fresh and reacted catalysts were examined by means of TEM. The particle size of CoO in CG(F) varied from 11 nm to 33 nm, while in CG(R) the particle size range was 62 nm to 96 nm. (See Figure 4.3 (a) and (c).) The particle size of CoO in RCG(F) varied from 15 nm to 32 nm, while the particle size range in RCG(R) was 30 nm to 73 nm. (See Figure 4.3 (e) and (g)) Therefore, the particle size grew dramatically after the reaction in both the CG and the RCG catalyst. So, the disordered RGO layers provided a substrate for the formation and growth of Co_2C through interaction between CoO and a regime of CO, H_2 and C_2H_4 during the reaction.

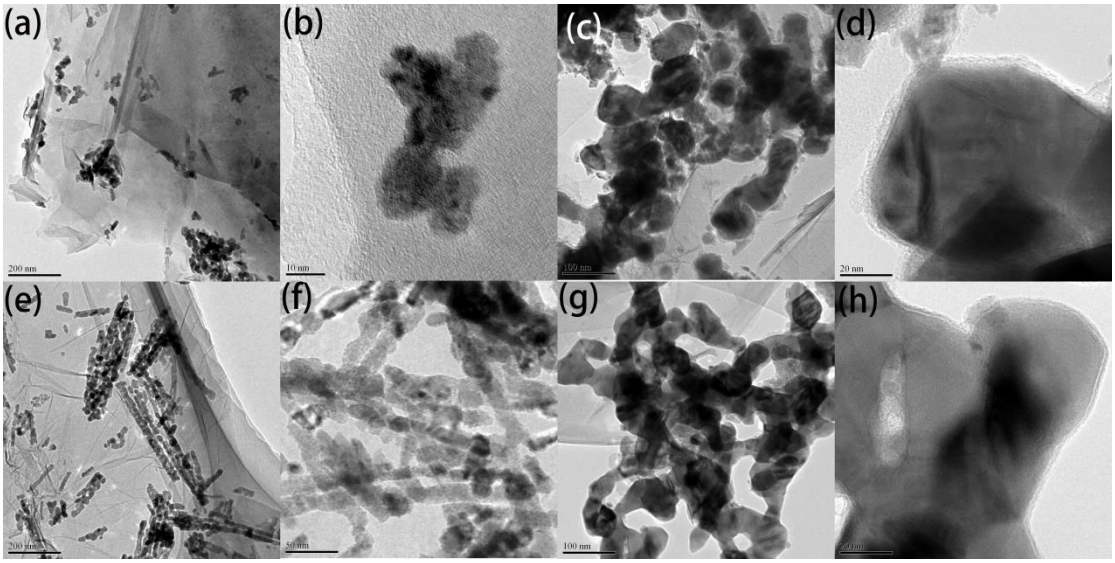

Figure 4.3 TEM images of fresh and reacted catalysts. CG(F) - (a) and (b);RCG(F) - (e) and (f), CG(R) - (c) and (d); RCG(R) - (g) and (h). (F) - fresh catalyst; (R) - reacted catalysts.

4.3.4 Raman

Raman spectroscopy was used to observe the structural and electronic changes in the catalyst of both the support RGO and the cobalt species before and after the reactions. Figure 4.4 shows that the original data was fitted using the Lorentzian method.

The presence of D` in the spectrum of CG(F) and RCG(F) (Figure 4.4 (a and c)) indicates that there are defects on the RGO planes in both the CG(F) and the RCG(F) catalyst, as D` normally appears in the Raman spectrum of defected graphite.[27,28] Figure 4.4 shows a 2D peak in CG(F), CG(R) and RCG(R), however, it was not detected in the spectrum of RCG(F). It has been reported that: the 2D peak is the D-peak overtone and no defects are required for its activation; the 2D band is not observed in the Raman spectra of chemisorbed graphene.[29][30]. Therefore, the addition of Rh resulted in more defects being induced on RGO in RCG(F) than in CG(F); the metals were chemisorbed on RGO in RCG(F), but not with the CG(F) catalysts.

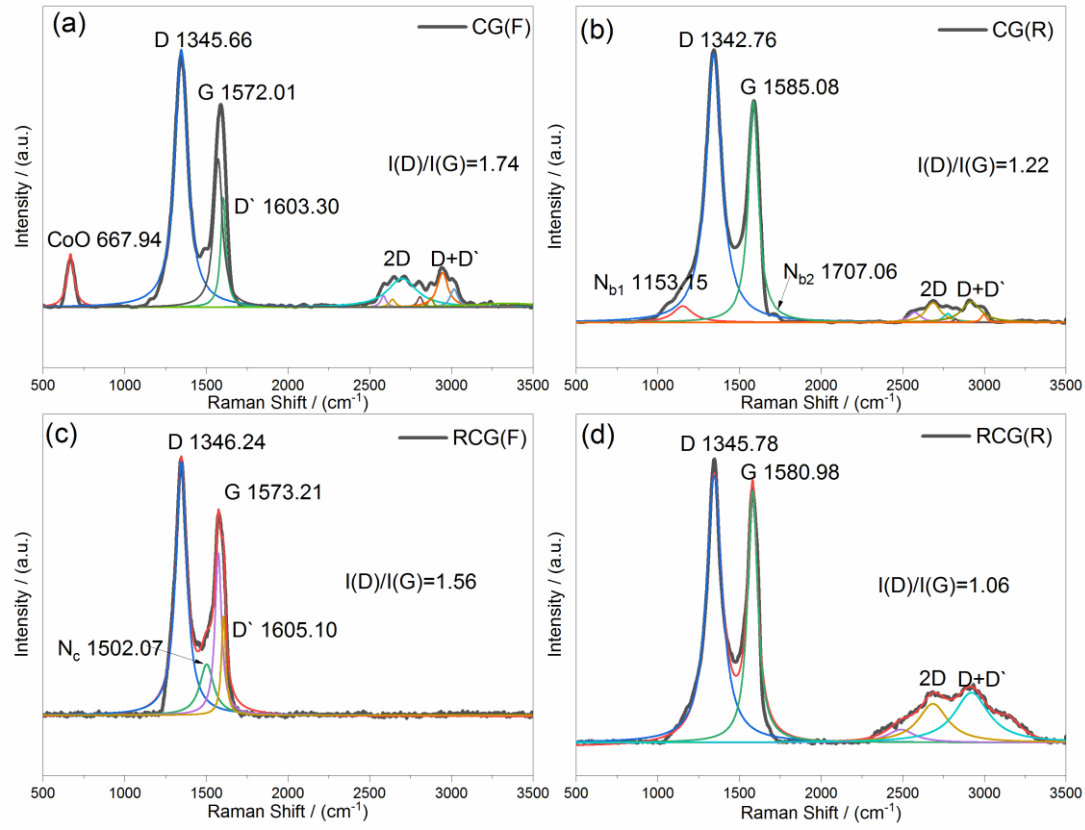

Figure 4.4 Raman spectra of fresh catalysts and reacted catalysts excited at 514 nm laser lines. (F) - fresh catalyst; (R) - reacted catalysts.

The Raman spectra for the used catalyst were plotted, as per Figure 4.4 (b) for CG(R) and Figure 4.4 (d) for RCG(R). After the experimental EH reaction, the D` peak disappeared and the 2D peak appeared for both CG(R) and RCG(R) This means that the defects decreased and the metals might not have chemisorbed in both CG(R) and RCG(R) after the EH reaction.

The relative intensity ratio of the D peak and G peak I(D)/I(G) is equivalent to normalizing the evolution of disorder, which is independent of the number of layers of graphene.[31] The results obtained with monolayer graphene can thus be used to explain the results in this research.[31] Figure 4.4 shows that: the I(D)/I(G) of CG decreased dramatically from 1.74 (Figure 4.4(a)) to 1.22 (Figure 4.4 (b)) after reaction; while the I(D)/I(G) of RCG decreased from 1.56 (Figure 4.4(c)) to 1.30 (Figure 4.4 (d)). The literature [32] indicates that the L_D of RGO in the fresh catalyst (L_D (nm) is the distance between the defects) is higher than 5 nm, while the L_D of RGO in the used catalyst is higher than 7 nm. Therefore, the relationship between $I(D)/I(G) \propto 1/L_D^2$ and $I(D)/I(G) \propto n_D^2$ (n_D (cm^{-2}) (i.e. defect density) are used to explain the results obtained in this research.[29,32] As the I(D)/I(G) decreased in this study, it was

concluded that the L_D of RGO increased and the n_D of RGO decreased after the reactions. This means that the defects of RGO decreased and the RGO surface was well restored after reaction.

As reported in the literature, doping is confirmed by a blue shift in the G peak, while FWHM (full width at half maximum) of the G peaks decreases significantly.[33] However, a red shift of the G peak (from 1572.01 to 1585.08 cm^{-1}) and an increase in FWHM of the G peak (from 64.31 to 74.70 cm^{-1}) were observed in the spectrum of CG(R). (See Table 4.1.) This possibly demonstrates a decrease in cobalt species doping on the RGO during the reactions. The same trend was observed in the RCG catalyst: a red shift of the G peak from 1573.21 to 1580.98 cm^{-1} and an increase in FWHM of the G peak (from 48.73 to 73.89 $cm^{-1)}$. This could be ascribed to the following: a decrease in the defects on the surface of RGO; the cobalt species crystal may be prone to grow on the surface of RGO, instead of doping with RGO. The decrease of cobalt species doping also led to an increase in particle size after the reactions, as indicated by the TEM.

Table 4.1 FWHM of the G peak in the Raman spectrum of RCG(F), RCG(R) and CG(F)

Sample	G peak FWHM (cm^{-1})
CG(F)	64.31
CG(R)	74.70
RCG(F)	48.73
RCG(R)	73.89

The peak at 667.94 cm^{-1} in the spectrum of CG(F) is attributed to the A_{1g} of CoO.[34,35] After reactions in the spectrum of CG(R), this peak disappeared. However, wo new peaks appeared in the spectrum of the used catalyst: N_{b1} at 1153.15 cm^{-1} and N_{b2} at 1707.06 cm^{-1}. N_{b2} is assigned to the Stokes combination of the E_{2g} LO phonon and the B_{2g} ZO´ phonon layer-breathing-modes for a few layers graphene.[29] More importantly, N_{b1} corresponds to neither cobalt species nor to RGO: its origin is due to interaction between cobalt species and RGO.[33] In the spectrum of RCG(F), an unknown peak presented at 1502.07 cm^{-1}, which is probably caused by a different interaction between CoO and RGO with the addition of Rh. (See Figure 4.4 (c).)

In summary, after the reactions, the structure of RGO was -restored and the RGO layer became more unique, which provides a better substrate for the growth of a crystalized Co_2C with a large size. Graphene is a two-dimensional structure that can provide a plane for crystal growth, while the traditional porous supports may have a prohibiting effect on crystal growth. This leads to a decrease in Co_2C doping on RGO and the strength of the interaction between Co_2C and RGO (which is different with doping).

4.3.5 FTS and EH performance over the CG catalyst

After reduction with H_2, the CG catalyst was tested for FTS activity, using syngas under typical FT reaction conditions. (See Table 4.2 and Figure 4.5.) No FTS activity was observed at 200 ℃. From 210 ℃ to 230 ℃, the CO conversion stabilized to about 1%. Even at 250 ℃, the CO conversion was only 5.21%. (See Figure 4.2.) It is worth noting that the selectivity to lower hydrocarbons (C_1-C_4 hydrocarbons) and C_1-C_5 alcohols is unusually high, namely 45.54% and 27.54%, respectively. (See Table 4.2.)

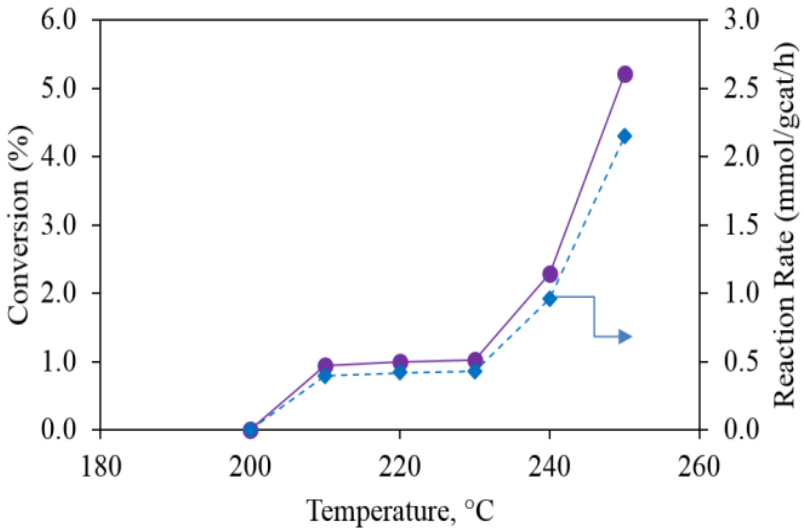

Figure 4.5 FTS CO conversion and reaction rate at different temperatures: P = 20 bar; CO : H_2 = 1 : 2; GHSV= 1800 h^{-1}. (CG catalyst).

Table 4.2 Reaction results for FTS. P = 20 bar; T = 250 ℃; CO:H_2 = 1:2; GHSV = 1800 h^{-1}

CO Conv.(%)	Selectivity			
	CO_2	C1-C4	C1-5 Alcohols	Other *
5.21	6.23	45.54	27.54	20.69

*The other products are higher alcohols and hydrocarbons.

The XRD data Figure 4.1 shows that multi Co-Co_2C phases occurred during syngas conversion. The experimental results indicate that the Co_2C formed on the catalyst surface suppressed FT chain growth reaction and increased the conversion of syngas to oxygenates.

With the aim of testing the catalytic function of Co_2C, a second group of experiments was conducted by switching between a SFT and a syngas-ethene feed. For purposes of convenience, the feed-gas switches were labelled as follows: (1) SFT; (2) EH; (3) SFT; (4) EH; (5) SFT. The experimental results plotted are shown in Figure 4.6. CO conversion increased dramatically between (1) SFT and (2) EH. CO conversion declined monotonically between (1) SFT, (3) SFT and (5) SFT, while CO conversion increased a little between (2) EH and (4) EH. In addition: the oxygenates that formed during (3) SFT and (5) SFT were different from those formed during (1) SFT; the formation rates decreased; the long chain alcohols C_4-C_5 were not formed in later cycles. In contrast, the oxygenated products formed during (2) EH and (4) EH comprised only C_2H_5CHO and C_3H_7OH; the formation rates of (4) EH were only a little higher than those of (2) EH. This indicates that the catalyst was changed by co-feeding ethene during the cycle and that it became more active for EH. This may be due to the growth of the Co_2C (111) facet, which may cause the catalytic performance to change.[19] The experimental results provide strong evidence that Co_2C is highly active for olefin hydroformylation rather than FTS. Furthermore, co-feeding ethene with syngas could have changed the nature of the active sites, and this change seems to be irreversible.

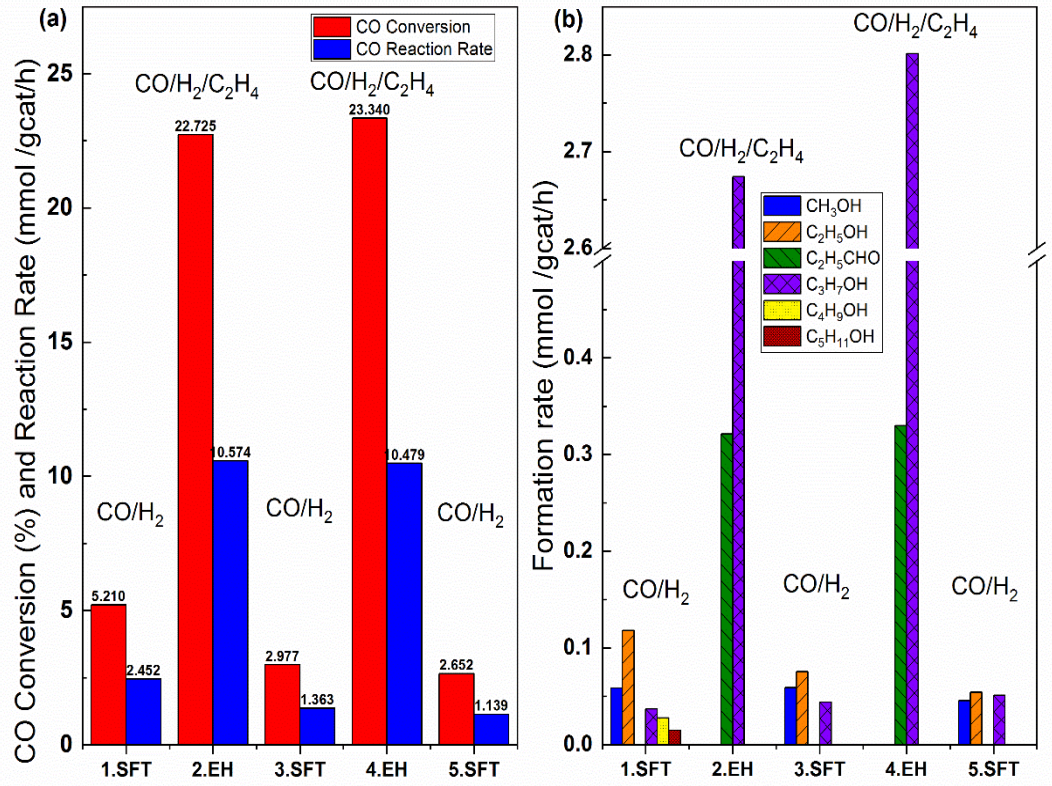

Figure 4.6 Cycle of FTS and EH by switching from syngas (SFT) and syngas with ethene (EH) over the CG catalyst. T = 250 ℃, P = 20 bar. FTS: 30 ml/min syngas (GHSV = 1800 h^{-1}), CO:H_2 = 1:2; EH: 30 ml/min syngas (CO:H_2 = 1:2) with 10 ml/min C_2H_4 (GHSV = 2400 h^{-1}).

In order to achieve high product selectivity towards C_2H_5CHO and C_3H_7OH on a CG catalyst, a feed-gas ratio of CO:C_2H_4:H_2 = 1:1:0.4 was used for EH. A higher CO ratio and lower H_2 ratio should limit the rate of the competing side reactions, mainly from ethene hydrogenation.[36] The experimental results obtained are summarized in Table 4.3. The selectivity to C_2H_5CHO and C_3H_7OH, based on converted ethene, is 16.62% and 20.32%, respectively. The total C_3 oxygenate selectivity is 36.94%. Only a small portion of ethene oligomerized to C_4 products. 78.92% of the reacted CO formed C_3 oxygenates with ethene, according to the selectivity based on converted CO. This means that CO hydrogenation through FTS was significantly inhibited. Furthermore, based on the total converted carbon from CO and ethene combined, the selectivity of the C_3 oxygenates is 44.85%, while the selectivity of ethane is 45.54%. Although selectivity to ethene hydrogenation is still high, the selectivity to EH is much higher than that of either FTS or ethene oligomerization. It can be concluded that the non-dissociative CO adsorption on Co_2C makes it highly active for EH, while limiting CO activation for chain growth. These results enhanced conversion of CO, C_2H_4 and H_2 towards C_3 oxygenates.

Table 4.3 Catalytic results for EH after FTS over the CG catalyst: P = 20 bar; T = 250 ℃, CO; C_2H_4:H_2 = 1:1:0.4; GHSV = 4440 h^{-1}.

Conversion(%)			Reaction rate ($mmol/g_{cat}/h$)			Selectivity based on Converted C_2H_4 (%)				Selectivity based on Converted Carbon (%)				Selectivity based on Converted CO (%)		
CO	C_2H_4	H_2	CO	C_2H_4	H_2	C_2H_6	C_2H_5CHO	C_3H_7OH	C_3Oxy^a	C_2H_6	C_2H_5CHO	C_3H_7OH	C_3Oxy^a	C_2H_5CHO	C_3H_7OH	C_3Oxy^a
10.56	24.56	73.93	15.49	32.86	42.64	56.33	16.62	20.32	36.94	45.54	20.17	24.68	44.85	35.43	43.50	78.92

[a]Total selectivity of (C_2H_5COH+C_3H_7OH)

4.3.6 FTS and EH performance over the RCG catalyst

A second group of experiments was also conducted on a RCG catalyst by switching between a syngas feed (SFT) and a syngas-ethene feed (EH). The set of feed-gas switches were denoted: (1) SFT; (2) EH; (3) SFT. The experimental results plotted are shown in Figure 4.7. In the initial stage, i.e. (1) SFT, the CO conversion was 0.596% and the CO reaction rate was 0.536 mmol/h/gcat. However, during stage (2) EH, the CO conversion and reaction rate increased dramatically to 17.281% and 12.601 mmol/h/gcat, respectively. Furthermore, at stage (3) SFT after EH, the CO conversion and reaction rate decreased to a far lower level than seen in the initial stage, i.e. (3) SFT: 0.052% and 0.038 mmol/h/gcat, respectively. A comparison of the data in Figure 4.6 and Figure 4.7 indicates that CO conversion for the RCG catalyst is much lower than for the CG catalyst initially, when introducing syngas into the ((1) SFT) reactor when using the same reaction conditions. The pure Co_2C phase was detected for the RCG catalyst, as shown in the XRD result (Figure 4.1) This indicates that Co_2C supported on RGO is not active for FTS, but is highly active for EH.

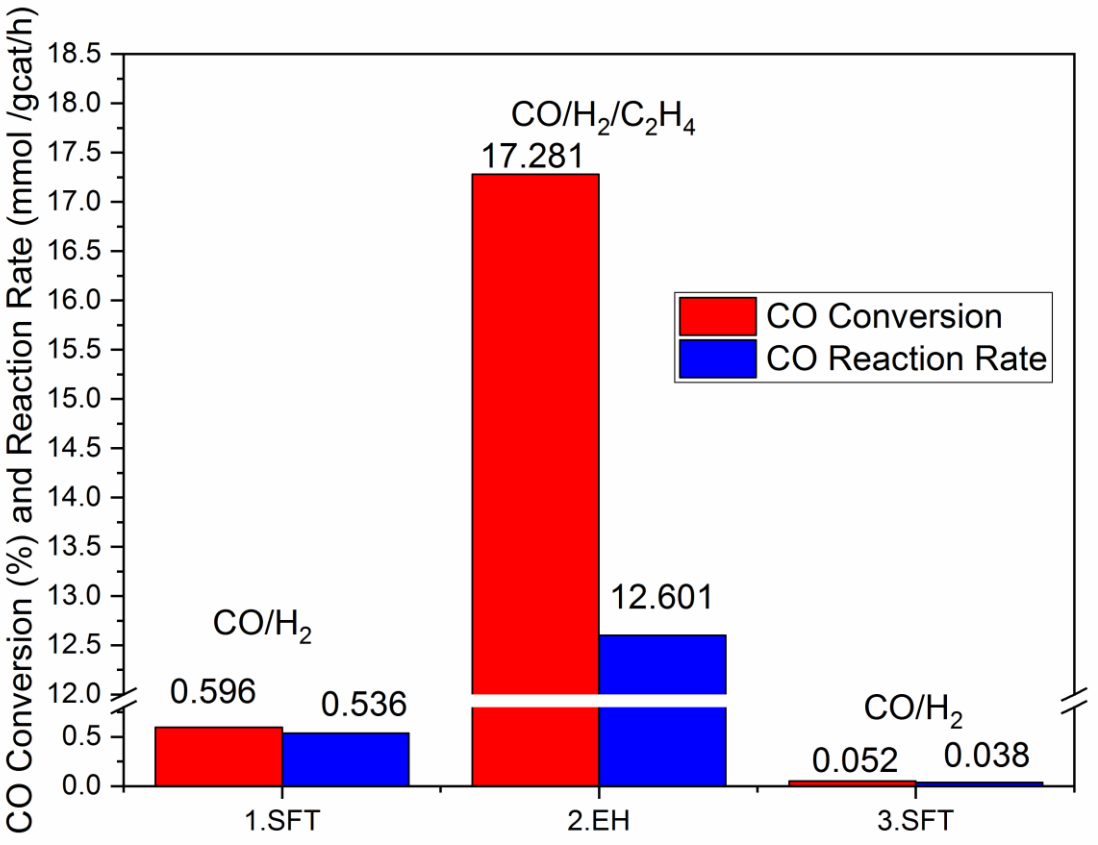

Figure 4.7 Cycle of FTS and EH by switching from syngas and syngas with ethylene. T = 250 ℃, P = 20 bar. FTS: GHSV = 800 h^{-1}, CO:H_2 = 1:2; EH: CO: C_2H_4:H_2 = 1:1:1 (GHSV = 1800 h^{-1}). (RCG catalyst).

4.4 Discussion

During H_2 reduction, Co_2C was formed for the Rh promoted catalyst (RCG), which indicates that RGO was the carbon source for the formation of carbides. However, no Co_2C was detected for the catalyst without Rh promotion. Pure Co_2C was formed after the SFT and EH reactions for the RCG catalyst (Figure 4.1) and it exhibited extremely low FT activity (CO conversion was less than 0.1%) and relatively high hydroformylation activity (Figure 4.7). These results indicate that: Rh plays an important role in enhancing the formation of Co_2C; it worked together with Co_2C to catalyse the hydroformylation reaction (Figure 4.7).

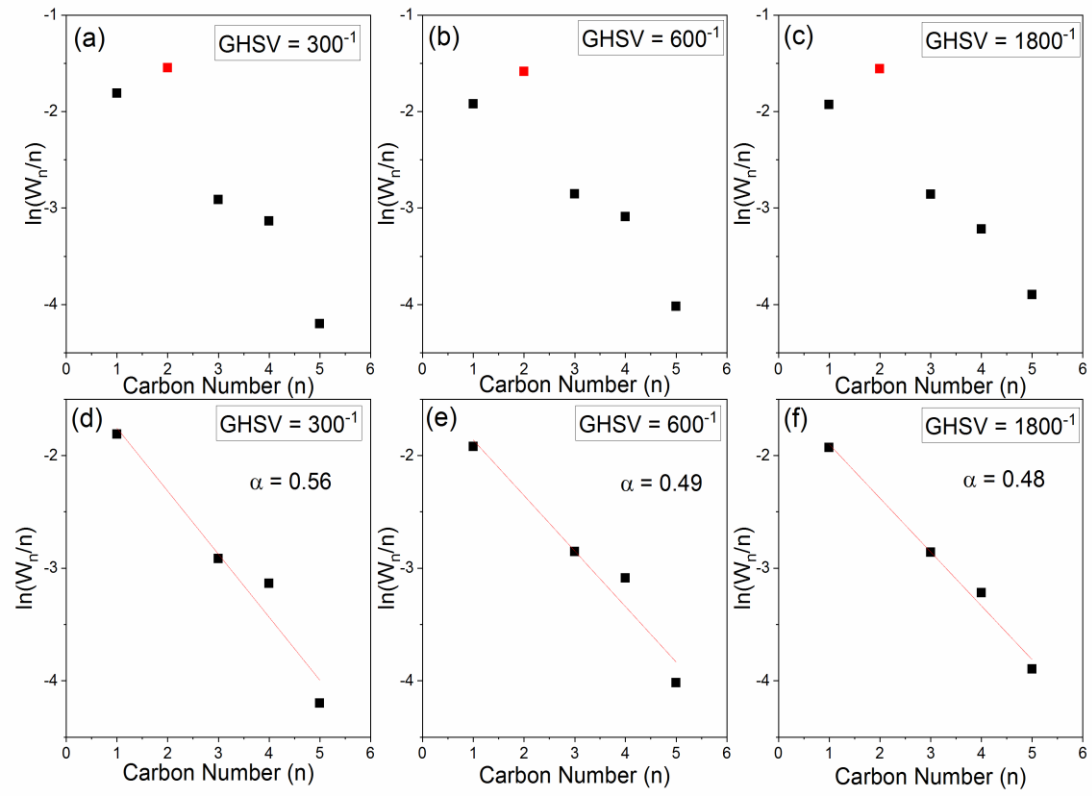

Figure 4.8 Alcohols product plot (ln(Wn/n)) versus carbon number n. Reaction conditions: P = 20 bar; T = 250 ℃; CO:H_2 = 1:2, at different GHSV. (CG catalyst)

It is generally accepted that metallic Co is active for FTS, while Co_2C is inactive for FTS.[14] This was also seen in the experimental data from this study (Figure 4.6 and 4.7). In addition, researchers report that Co_2C does not form easily during FTS[37]. Furthermore, Co_2C is unstable and could easily transform back to metallic Co[14,38]. The present work showed that Co_2C was formed during the SFT and EH reactions with the CG catalyst. It was also extremely stable on the RGO, as the low FTS activity and the high selectivity of the oxygenates was observed for all the runs conducted, including when switching the feed between syngas and syngas with ethene, and when using different reaction temperatures and different flow rates. The experimental data indicate that Co_2C is stable under the conditions.

The catalytic behaviour of both the CG and RCG catalyst was changed to enhance the production of the C_3 oxygenates after introducing syngas co-feeding with ethene (Figure 4.6 and 4.7). This indicates that the feed mixture of $CO/H_2/C_2H_4$ is a desirable agent for the activation of CoO supported on an RGO catalyst with high hydroformylation activity.

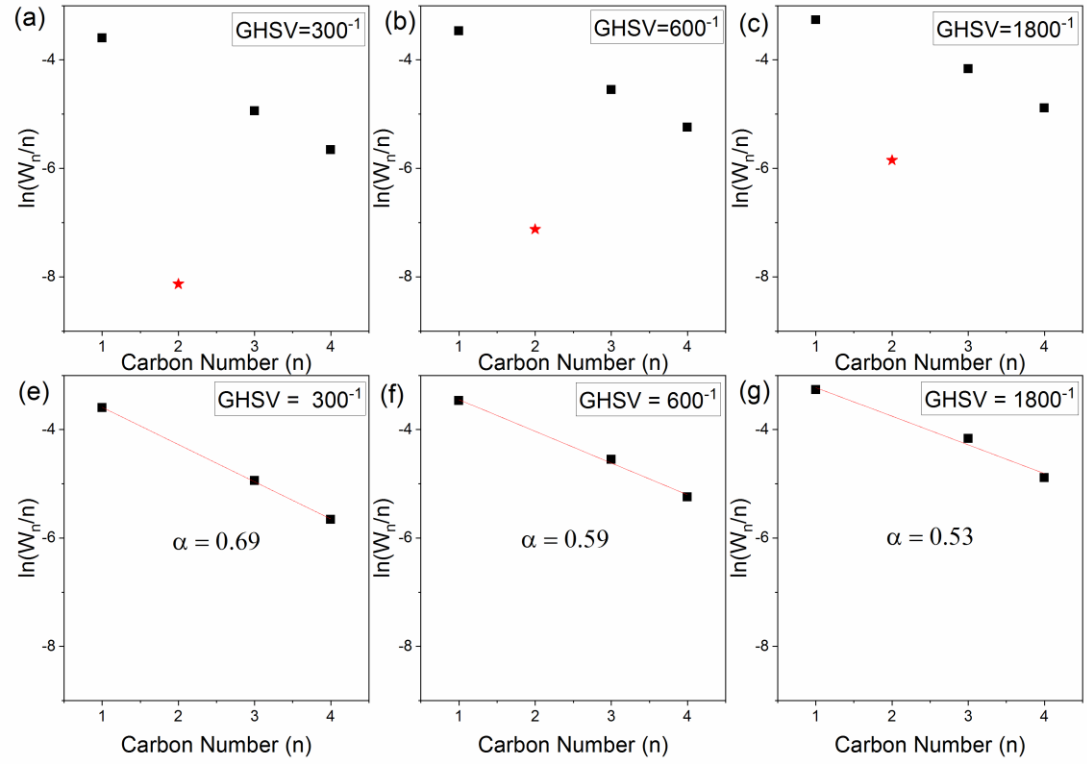

Figure 4.9 C_1-C_4 Hydrocarbons product plots (ln(Wn/n)) versus Carbon number n. Reaction conditions: P = 20 bar; T = 250 ℃; CO:H_2 = 1:2, at different GHSV. (CG catalyst)

Figure 4.6 shows that the initial runs of SFT produce more longer chain oxygenates, such as $C_{4\text{-}5}$ alcohols. Before doing the switching experiments, another group of experiments was conducted by changing the flow rate of the syngas - see Figure 4.6. The product distribution of the C_1-C_5 alcohols obtained at different GHSV were plotted as (ln(Wn/n)) versus carbon number - see Figure 4.8 (a), (b) and (c). Figure 4.8 (e), (f) and (g) display the linear fitted plots without the C_2 point. It is obvious that the data points of the C_1, C_3, C_4 and C_5 alcohols followed the Anderson-Schulz-Flory (ASF) distribution closely with all GHSV rates; however, the data points of C_2 deviated from the ASF plots with all GHSV rates.

Hydrocarbon products were also produced. The C_1-C_4 hydrocarbon product distribution obtained at different GHSV rates were plotted as (ln(Wn/n)) versus carbon number, as shown in Figure 4.9 (a), (b) and (c). Figure 4.9 (e), (f) and (g) display the linear fitted plots without the C_2 point. It is obvious that the data points of the C_1, C_3 and C_4 hydrocarbons follow the ASF distribution in all the GHSV results;

however, the data points of C_2 deviated from the ASF plot in all the GHSV results. Generally, C_1 was above the ASF plot for normal Co-based catalysts [39,40]. However, the results show that the C_1 was lie on the ASF plot for all the runs over the CG catalyst.

The mechanisms of FTS are quite complicated because of its complex product spectrum, and different mechanisms have been proposed by many researchers.[41] Among them, CO dissociation and CO insertion mechanisms have been developed and they may synergistically and competitively catalyse the FT reaction. The XRD results (Figure 4.1) show that the multi Co-Co_2C phases co-exist. As discussed above, Co_2C is active for the hydroformylation reaction and Co is active for the FT chain growth reaction. Under the reaction conditions used, both hydrocarbon products and oxygenates were produced – see Figures 4.6 and 4.7. Both figures reveal an ASF product distribution, while the values of the chain growth probability (α) were different: the one for hydrocarbons was much higher than the one for alcohols.

The data indicate that there may be different mechanisms that are followed for with two groups of products. In addition, the experimental data indicate that pure Co_2C has no chain growth activity (Figure 4.7), so that the production of C_2-C_5 alcohols from syngas may be catalysed synergistically by the multi Co-Co_2C phases. A possible pathway for the production of chain growth alcohol is shown in Scheme 1(b). It shows that metallic Co is active for the chain growth reaction (R-CH_x*), and the Co_2C could activate the absorbed CO (*CO), and the R-CH_x* and *CO could be reacting together on the interface of Co-Co_2C to form long chain oxygenates.

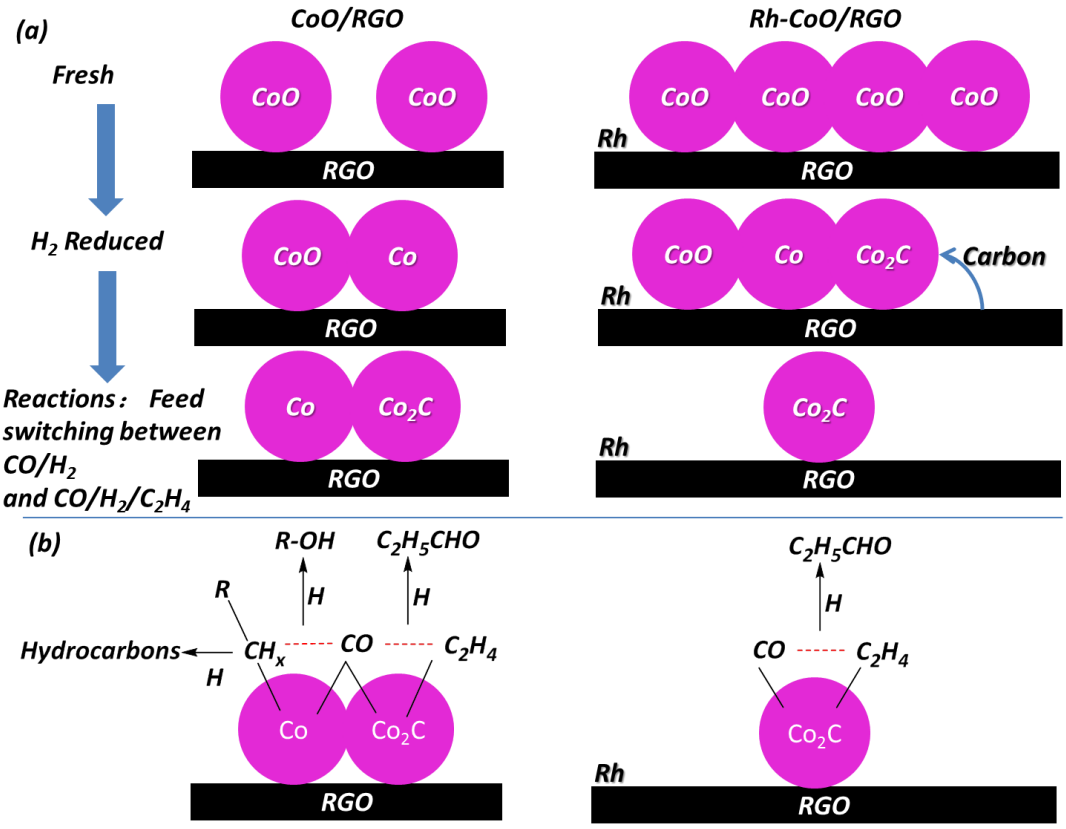

Scheme 4.1 Illustration of cobalt phase changes during the whole process on the two catalysts - (a). Proposed reaction pathways on the two catalysts - (b).

4.5 Conclusion

CoO/RGO after H_2 reduction exhibited very low FT reaction activity. This indicated that Co-RGO interaction prevented the FT chain growth reaction, which shows that Co_2C/RGO can be formed under an atmosphere of syngas or syngas co-feeding with ethene on a CG catalyst. EH catalysed by Co_2C has been demonstrated experimentally. The performance of Co_2C/RGO for EH was investigated and showed promising activity and reasonably high selectivity to C_3 oxygenates. It was found that the Co-Co_2C was not active for FTS with a low CO conversion and reaction rate, with the main products being short chain alcohols and hydrocarbons (C_1-C_4) that follow the ASF product distribution. The Co-Co_2C i was highly active for EH. Exposure of the Co-Co_2C to $CO/C_2H_4/H_2$ increased the activity in producing C_3 oxygenates.

A trace amount of Rh significantly enhances the formation of Co_2C on the RGO during H_2 reduction, and treatment with syngas and syngas co-feeding with ethene. The pure Co_2C phase was inactive for

FTS, but highly active for EH. It can be concluded that Co_2C may suppress CO from attending the chain growth reaction, but promote CO insertion to form aldehyde or alcohols. Different atmosphere treatments may change the nature of the active site significantly; consequently, the catalytic performance may be tuned, in particular with co-feeding ethene with syngas, which leads to an irreversible change in the activity and selectivity.

The interphase of Co-Co_2C has the potential to synergistically catalyze the conversion of syngas to long chain oxygenates by combining the chain growth reaction and the hydroformylation reaction. The formation of Co_2C limits the CO conversion to chain growth reaction for subsequent FTS chain growth or direct conversion of syngas to alcohols. This could be evidence of non-dissociative adsorption of CO on Co_2C. Co_2C/RGO derived from CoO/RGO is highly active for heterogeneous EH and has potential for use in industrial hydroformylation processes.

References

[1] R. Franke, D. Selent, A. Borner, Applied hydroformylation, Chem. Rev. 112 (2012) 5675–5732. https://doi.org/10.1021/cr3001803.

[2] E.V. Gusevskaya, J. Jiménez-Pinto, A. Börner, Hydroformylation in the realm of scents, ChemCatChem. 6 (2014) 382–411. https://doi.org/10.1002/cctc.201300474.

[3] C. Li, W. Wang, L. Yan, Y. Ding, A mini review on strategies for heterogenization of rhodium-based hydroformylation catalysts, Front. Chem. Sci. Eng. 12 (2018) 113–123. https://doi.org/10.1007/s11705-017-1672-9.

[4] X. Wang, Recent advances in continuous rhodium-catalyzed hydroformylation, J. Flow Chem. 5 (2015) 125–132. https://doi.org/10.1556/1846.2015.00003.

[5] Â.C.B. Neves, M.J.F. Calvete, T.M.V.D. Pinho E Melo, M.M. Pereira, Immobilized catalysts for hydroformylation reactions: A versatile tool for aldehyde synthesis, European J. Org. Chem. (2012) 6309–6320. https://doi.org/10.1002/ejoc.201200709.

[6] R. Tudor, A. Shah, Industrial low pressure hydroformylation: Forty-five years of progress for the LP Oxo SM process, Johnson Matthey Technol. Rev. 61 (2017) 246–256. https://doi.org/10.1595/205651317x695875.

[7] K.S. Novoselov, A.K. Geim, S.V. Morozov, D. Jiang, Y. Zhang, S. V Dubonos, I.V. Grigorieva, A.A. Firsov, Electric field effect in atomically thin carbon films, Science (80). 306 (2004) 666–669. https://doi.org/10.1126/science.1102896.

[8] J. Xu, R.S. Ruoff, H. Zhu, The physics and chemistry of graphene-on-surfaces, Chem. Soc. Rev. 46 (2017) 4417–4449. https://doi.org/10.1039/C7CS00256d.

[9] Y. Cheng, Y. Fan, Y. Pei, M. Qiao, Graphene-supported metal/metal oxide nanohybrids: Synthesis and applications in heterogeneous catalysis, Catal. Sci. Technol. 5 (2015) 3903–3916. https://doi.org/10.1039/C5CY00630A.

[10] V. Singh, D. Joung, L. Zhai, S. Das, Progress in materials science graphene based materials: Past, present and future, Prog. Mater. Sci. 56 (2011) 1178–1271.

https://doi.org/10.1016/j.pmatsci.2011.03.003.

[11] P. Hasin, Low-temperature synthesis of mesoporous cobalt(II) carbide using graphene oxide as a carbon source, J. Phys. Chem. C. 118 (2014) 4726–4732. https://doi.org/10.1021/jp411844a.

[12] M.D. Meganathan, S. Mao, T. Huang, G. Sun, Reduced graphene oxide intercalated Co2C or Co_4N nanoparticles as an efficient and durable fuel cell catalyst for oxygen reduction, J. Mater. Chem. A. 5 (2017) 2972–2980. https://doi.org/10.1039/C6TA09729D.

[13] S. Weller, L.J.E. Hofer, R.B. Anderson, The role of bulk cobalt carbide in the Fischer—Tropsch Synthesis1, J. Am. Chem. Soc. 70 (1948) 799–801. https://doi.org/10.1021/ja01182a108.

[14] J.C. Mohandas, M.K. Gnanamani, G. Jacobs, W. Ma, Y. Ji, S. Khalid, B.H. Davis, Fischer-Tropsch synthesis: Characterization and reaction testing of cobalt carbide, ACS Catal. 1 (2011) 1581–1588. https://doi.org/10.1021/cs200236q.

[15] L. Zhong, F. Yu, Y. An, Y. Zhao, Y. Sun, Z. Li, T. Lin, Y. Lin, X. Qi, Y. Dai, L. Gu, J. Hu, S. Jin, Q. Shen, H. Wang, Cobalt carbide nanoprisms for direct production of lower olefins from syngas, Nature. 538 (2016) 84–87. https://doi.org/10.1038/nature19786.

[16] M.K. Gnanamani, G. Jacobs, U.M. Graham, M.C. Ribeiro, F.B. Noronha, W.D. Shafer, B.H. Davis, Influence of carbide formation on oxygenates selectivity during Fischer-Tropsch synthesis over Ce-containing Co catalysts, Catal. Today. 261 (2016) 40–47. https://doi.org/10.1016/j.cattod.2015.08.047.

[17] Y.P. Pei, J.X. Liu, Y.H. Zhao, Y.J. Ding, T. Liu, W. Da Dong, H.J. Zhu, H.Y. Su, L. Yan, J.L. Li, W.X. Li, High alcohols synthesis via Fischer-Tropsch reaction at cobalt metal/carbide interface, ACS Catal. 5 (2015) 3620–3624. https://doi.org/10.1021/acscatal.5b00791.

[18] W. Dong, J. Liu, H. Zhu, Y. Ding, Y. Pei, J. Liu, H. Du, M. Jiang, T. Liu, H. Su, W. Li, Co–Co2C and Co–Co2C/AC catalysts for hydroformylation of 1-hexene under low pressure: experimental and theoretical studies, J. Phys. Chem. C. 118 (2014) 19114–19122. https://doi.org/10.1021/jp504215y.

[19] P. Chen, J. Liu, W. Li, Carbon monoxide activation on cobalt carbide for Fischer–Tropsch Synthesis from First-Principles Theory, ACS Catal. 9 (2019) 8093–8103. https://doi.org/10.1021/acscatal.9b00649.

[20] V. Bernales, R.D. Froese, Rhodium catalyzed hydroformylation of olefins, J. Comput. Chem. 40 (2019) 342–348. https://doi.org/10.1002/jcc.25605.

[21] W.S. Hummers, R.E. Offeman, Preparation of graphitic oxide, J. Am. Chem. Soc. 80 (1958) 1339. https://doi.org/10.1021/ja01539a017.

[22] H. Yu, B. Zhang, C. Bulin, R. Li, R. Xing, High-efficient synthesis of graphene oxide based on improved Hummers method, Sci. Rep. 6 (2016) 36143. https://doi.org/10.1038/srep36143.

[23] F. Morales, F.M.F. de Groot, O.L.J. Gijzeman, A. Mens, O. Stephan, B.M. Weckhuysen, Mn promotion effects in Co/TiO2 Fischer-Tropsch catalysts as investigated by XPS and STEM-EELS, J. Catal. 230 (2005) 301–308. https://doi.org/10.1016/j.jcat.2004.11.047.

[24] Y. Li, X. Qin, T. Wang, L. Ma, L. Chen, N. Tsubaki, Fischer-Tropsch synthesis from H2-deficient biosyngas over Mn added Co/SiO2 catalysts, Fuel. 136 (2014) 130–135. https://doi.org/10.1016/j.fuel.2014.06.048.

[25] A.A. Mirzaei, S. Vahid, H.O. Torshizi, Effect of support and promoter on the catalytic performance and structural properties of the Fe-Co-Ni catalysts for CO hydrogenation, J. Nat. Gas Sci. Eng. 15 (2013) 106–117. https://doi.org/10.1016/j.jngse.2013.10.002.

[26] Ø. Borg, S. Eri, E. a. Blekkan, S. Storsæter, H. Wigum, E. Rytter, A. Holmen, Fischer-Tropsch synthesis over γ-alumina-supported cobalt catalysts: Effect of support variables, J. Catal. 248 (2007) 89–100. https://doi.org/10.1016/j.jcat.2007.03.008.

[27] D.M. Basko, S. Piscanec, A.C. Ferrari, Electron-electron interactions and doping dependence of the two-phonon Raman intensity in graphene, Phys. Rev. B. 80 (2009) 1–10. https://doi.org/10.1103/physrevb.80.165413.

[28] W. Luo, S. Zafeiratos, Tuning morphology and redox properties of cobalt particles supported on oxides by an in-between graphene layer, J. Phys. Chem. C. 120 (2016) 14130–14139. https://doi.org/10.1021/acs.jpcc.6b03595.

[29] A.C. Ferrari, D.M. Basko, Raman spectroscopy as a versatile tool for studying the properties of graphene, Nat. Nanotechnol. 8 (2013) 235–246. https://doi.org/10.1038/nnano.2013.46.

[30] D.Y. Usachov, V.Y. Davydov, V.S. Levitskii, V.O. Shevelev, D. Marchenko, B.V. Senkovskiy, O.Y. Vilkov, A.G. Rybkin, L.V. Yashina, E. V. Chulkov, I.Y. Sklyadneva, R. Heid, K.P. Bohnen, C. Laubschat, D.V. Vyalikh, Raman spectroscopy of lattice-matched graphene on strongly interacting metal surfaces, ACS Nano. 11 (2017) 6336–6345. https://doi.org/10.1021/acsnano.7b02686.

[31] A. Jorio, M.M. Lucchese, F. Stavale, E.H.M. Ferreira, M.V.O. Moutinho, R.B. Capaz, C.A. Achete, Raman study of ion-induced defects in N-layer graphene, J. Phys. Condens. Matter. 334204 (2010). https://doi.org/10.1088/0953-8984/22/33/334204.

[32] L.G. Cançado, A. Jorio, E.H.M. Ferreira, F. Stavale, C.A. Achete, R.B. Capaz, M.V.O. Moutinho, A. Lombardo, T.S. Kulmala, A.C. Ferrari, Quantifying defects in graphene via Raman spectroscopy at different excitation energies, Nano Lett. 11 (2011) 3190–3196. https://doi.org/10.1021/nl201432g.

[33] I. Serrano-Esparza, J. Fan, J.M. Michalik, L.A. Rodríguez, M.R. Ibarra, J.M. de Teresa, The nature of graphene-metal bonding probed by Raman spectroscopy: The special case of cobalt, J. Phys. D. Appl. Phys. 49 (2016). https://doi.org/10.1088/0022-3727/49/10/105301.

[34] S. Gupta, S.B. Carrizosa, Graphene–inorganic hybrids with cobalt oxide polymorphs for electrochemical energy systems and electrocatalysis: Synthesis, processing and properties, J. Electron. Mater. 44 (2015) 4492–4509. https://doi.org/10.1007/s11664-015-4016-x.

[35] Y. Li, W. Qiu, F. Qin, H. Fang, V.G. Hadjiev, D. Litvinov, J. Bao, Identification of cobalt oxides with Raman scattering and Fourier transform infrared spectroscopy, J. Phys. Chem. C. 120 (2016) 4511–4516. https://doi.org/10.1021/acs.jpcc.5b11185.

[36] N. Navidi, J.W. Thybaut, G.B. Marin, Experimental investigation of ethylene hydroformylation to propanal on Rh and Co based catalysts, Appl. Catal. A Gen. 469 (2014) 357–366. https://doi.org/10.1016/j.apcata.2013.10.019.

[37] M. Claeys, M.E. Dry, E. van Steen, E. du Plessis, P.J. van Berge, A.M. Saib, D.J. Moodley, In

situ magnetometer study on the formation and stability of cobalt carbide in Fischer-Tropsch synthesis, J. Catal. 318 (2014) 193–202. https://doi.org/10.1016/j.jcat.2014.08.002.

[38] Q. Lin, B. Liu, F. Jiang, X. Fang, Y. Xu, X. Liu, Assessing the formation of cobalt carbide and its catalytic performance under realistic reaction conditions and tuning product selectivity in a cobalt-based FTS reaction, Catal. Sci. Technol. 9 (2019) 3238–3258. https://doi.org/10.1039/C9CY00328B.

[39] E.W. Kuipers, C. Scheper, J.H. Wilson, I.H. Vinkenburg, H. Oosterbeek, Non-ASF product distributions due to secondary reactions during Fischer–Tropsch Synthesis, J. Catal. 158 (1996) 288–300.

[40] Y.Y. Ji, H.W. Xiang, J.L. Yang, Y.Y. Xu, Y.W. Li, B. Zhong, Effect of reaction conditions on the product distribution during Fischer-Tropsch synthesis over an industrial Fe-Mn catalyst, Appl. Catal. A Gen. 214 (2001) 77–86. https://doi.org/10.1016/S0926-860X(01)00480-X.

[41] J. van de Loosdrecht, F.G. Botes, I.M. Ciobica, A. Ferreira, P. Gibson, D.J. Moodley, A.M. Saib, J.L. Visagie, C.J. Weststrate, J.W. Niemantsverdriet, A linear dependence of these probabilities on the transient CO gas pressure provides evidence for, in: J. Reedijk, K.B.T.-C.I.C.I.I. (Second E. Poeppelmeier (Eds.), Elsevier, Amsterdam, 2013: pp. 525–557. https://doi.org/https://doi.org/10.1016/B978-0-08-097774-4.00729-4.

Chapter 5: Rh/Co/rGO catalyst for heterogenous ethylene hydroformylation: Bimetallic species-support interaction

Abstract

The metal-support interaction (MSI) alters the geometric morphologies, electronic properties, or distribution of metal nanoparticles, which is indeed to influence the heterogenous catalytic system. Two heterogenous ethylene hydroformylation catalysts, cobalt supported on reduced graphene oxide (RGO) with or without Rhodium (5%Rh-20%Co/RGO and 20%Co/RGO), were successfully synthesized. The effect of the MSI between Co and RGO and a MSI tuning strategy by Rh on the ethylene hydroformylation were investigated. CoO nanorods was present in fresh Rh-Co/RGO, while only CoO nano-particles were formed in fresh Co/RGO. Rh enhanced the reducibility of the cobalt species. After reduction and the ethylene hydroformylation reaction, Co_2C was formed in spent Rh-Co/RGO, while a mixture of Co and CoO were present in spent Co/RGO. Co_2C grew to a large flat plane structure in spent Rh-Co/RGO, while Co and CoO formed smaller nano-particles in spent Co/RGO. The changes of the geometric morphologies and the phases of the active species made by the Rh-Co-RGO interaction significantly enhance the activity of the CO and the selectivity for the production of the C_3 oxygenates. A Model on how the nanoparticles distributed on the RGO were hypothesized.

5.1 Introduction

Hydroformylation is one of the most important homogeneous industrial processes used to produce value-added aldehydes, and great effort has been made i.t.o. heterogenizing this process to overcome the disadvantages of the homogeneous process, such as catalyst recovery, product separation and high pressure.[1–3] Carbon materials have been applied in the field of syngas conversion for decades, because of the relatively weak MSI, which makes it easy to tailor the catalyst properties.[4] Likewise, carbon materials are also used as a support for heterogeneous hydroformylation, including nanotubes,[5–7] AC,[8–10] and graphite nanofibers.[11] In recent years, graphene (the basic building block of graphitic materials that have unique properties) has been used as a support material in

hydroformylation.[12–15] However, most of the research done to date has focused on catalytic performance, and there is a lack of information on the effect of MSI.[13–15]

Metal that is heterogeneously dispersed on a support plays a vital role in the catalysis of a wide range of industrial reactions, and MSI in catalysts has received much attention in recent years because of its impact on catalysis.[16–19] The catalysis can be influenced by MSI through charge transfer, the interfacial perimeter, nanoparticle morphology, chemical composition and strong MSI.[20,21] Furthermore, the intermetallic compounds formed through MSI are highly active for certain corresponding reactions.[22,23] Therefore, strategies for tuning MSI to enhance the performance of catalysts has been studied i.t.o. commercial supports, especially metal oxide supports.[20,21,24] Tuning MSI is important i.t.o. selectively increasing the yield of the target products (including hydrocarbons and oxygenates) from both Fischer-Tropsch Synthesis (FTS) and EH reactions.[17,18,25–27] Hence, it is important to investigate and develop tuning strategies for MSI in graphene-based hydroformylation catalysts.

Rhodium and cobalt are the most active and most commonly-used metals in industrial hydroformylation processes.[28,29] Therefore, in this study, a RGO-supported cobalt catalyst and a rhodium-promoted cobalt catalyst supported by RGO were tested for EH performance. Special attention was paid to MSI in the catalysts.

5.2 Experiment

5.2.1 Preparation of catalysts

The methods for synthesis of catalysts are the same with that in Chapter4

1) Graphene Oxide (GO)

10 g of graphite was added to 230 ml of 95% H_2SO_4 and the mixture was stirred for 30 min in an ice-water bath. 50 g of $KMnO_4$ was then slowly added to the mixture over 2 hours and the mixture was stirred for another 1 h. After the ice-water was removed, the mixture was left to settle at room temperature for about 16 h. Then the mixture was put in ice obtained from an H_2O_2 aqueous solution

(5ml 30% H_2O_2 in 100ml deionized water). The colour of the mixture then changed to bright yellow. To remove the residual metal ions, the mixture was centrifuged and washed with deionized water (to remove the remaining sulfuric acid) until the pH value of the supernatant was neutral (pH 7). The graphene oxide yield was 13.86 mg/ml.

2) 20%Co/RGO (CG)

A 346 ml GO solution (4.8 g GO) was subjected to ultrasound for 30 min. Then 10 ml of a solution of 5.06 g $Co(Ac)_2 \cdot 4H_2O$ was added. After the solution was subjected to ultrasound for 30 min, the pH value was adjusted to 10, and 2 ml hydrazine hydrate was then added. Thereafter, the solution was subjected to ultrasound for 30 min and the solution was then moved to a teflon-lined stainless steel autoclave. The GO was reduced using the hydro-thermal method at 180 ℃ for 15 h. The obtained sample was dried at 80 ℃ and calcined at 400 ℃ for 5 h under an N_2 atmosphere.

3) 0.5%Rh-20%Co/RGO (RCG)

A 346 ml GO solution (4.77g GO) was subjected to ultrasound for 30 min. Then 10ml of a solution of 5.06 g $Co(Ac)_2 \bullet 4H_2O$ and 0.08 g $RhCl_3 \cdot 3H_2O$ was added to the GO solution. After the solution was treated by ultrasound for 30 min, the pH was adjusted to 10, and 2 ml of hydrazine hydrate was added. Thereafter, the solution was treated by ultrasound for 30 min, and the solution was then moved to a teflon-lined stainless steel autoclave. The GO was reduced using the hydro-thermal method at 180 ℃ for 15 h. The obtained sample was dried at 80 ℃ and calcined at 400 ℃ for 5 h under an N_2 atmosphere.

5.2.2 Characterization

The morphology of the samples was captured by emission scanning electron microscopy (SEM) images, using the Hitachi S-4800 equipment. Transmission electron microscopy (TEM) was done using a JEOL JEM-2000 microscope (200 kV). Thermo gravimetric analysis was tested using a SDT Q600 Thermo Gravimetric Analyzer. Powder X-ray diffraction (XRD) patterns were obtained using a Rigaku D/MAX-2500 XRD system (Cu Kα radiation, λ = 0.15406 nm) operated at 40 kV and 40 mA. H_2 temperature-programmed reduction (TPR) was done using a Zeton Altamira AMI-200 instrument. Prior to TPR measurement, the catalyst was flushed with Ar (> 99.999 %) at 150 °C for 1 h, and then

cooled to 50 °C.The temperature was then raised from 50 to 800 °C using a ramp rate of 10 °C min^{-1} under H_2 / Ar (volume ratio 1 / 9, flow rate 30 mL min^{-1}), and the temperature was then maintained at 800 °C for 30 min. The H_2 concentration was monitored by means of a thermal conductivity detector (TCD). The H_2-TPR profile was recorded as H_2 consumption versus reduction temperature. Raman spectroscopy was obtained by means of a Horiba Scientific LabRAM HR Evolution instrument using 514 nm.

5.2.3 Catalytic performance

The performance of the catalysts was evaluated using a fixed-bed reactor (FBR) with an internal diameter of 8 mm and a length of 380 mm. The 0.5 g catalyst was loaded into the reactor and reduced with H_2 (AFROX – 99.999%) at 350 °C, 1 bar, 30ml/min for 20 h. The EH reaction was then initiated, using the two catalysts under the following conditions: P = 2 MPa; GHSV = 1200 h^{-1}; Feed-gas ratio: (N_2 : C_2H_4 : CO : H_2 = 1 : 1 : 1 :1); temperature of 220 to 250 °C. All the feed-gas, calibration gas and products were analyzed using the online Agilent 7890B GC. Oxygenates and hydrocarbons were separated using a CP-Sil 5CB (25 m x 0.15 mm x 2.0 µm) column and analyzed by FID. The other gases were analyzed by TCD. Finally, the used catalyst was unloaded for further characterisation.

5.2.4. Calculations

1) Reaction rate:

$$-r_x = \frac{F_{x,in} - F_{x,out}}{m_{cat}} \qquad (5.1)$$

Where: $F_{x,in}$ is the molar flow rate of component x in the feed-gas, mmol/h; $F_{x,out}$ is the molar flow rate of component x in the tail-gas, mmol/h; m_{cat} is the mass of catalyst loaded into the reactor, g; r_x is the reaction rate of component x, mmol/h/gcat; x is one of the components in the feed-gas (CO, H_2, C_2H_4).

2) Conversion:

$$x_{conv} = \left(\frac{F_{x,in} - F_{x,out}}{F_{x,in}}\right) \times 100\% \qquad (5.2)$$

Where: $F_{x,in}$ is the molar flow rate of component x in the feed-gas, mmol/h; $F_{x,out}$ is the molar flow rate of component x in the tail-gas, mmol/h; x_{conv} is the conversion of component x, %; x is one of the components in the feed-gas (CO, H_2, C_2H_4).

3) Selectivity based on total converted carbon from CO and C_2H_4:

$$S_{x,carbon} = \left[\frac{n \times F_{x,out}}{2\times(F_{C_2H_4,in}-F_{C_2H_4,out})+(F_{CO,in}-F_{CO,out})}\right] \times 100\% \qquad (5.3)$$

Where: $F_{x,out}$ is the molar flow rate of product x in the tail-gas, mmol/h; $F_{C_2H_4,in}$ is the molar flow rate of C_2H_4 in the feed-gas, mmol/h; $F_{C_2H_4,out}$ is the molar flow rate of C_2H_4 in the tail-gas, mmol/h; $F_{CO,in}$ is the molar flow rate of CO in the feed-gas, mmol/h; $F_{CO,out}$ is the molar flow rate of CO in the tail-gas, mmol/h; n is the carbon number in product x; $S_{x,carbon}$ is the selectivity of product x based on total converted carbon from CO and C_2H_4, %; x is C_2H_6 or C_2H_5CHO or C_3H_7OH.

5.3 Results and Discussion

5.3.1 Characterization results

1) XRD

XRD was used to analyse the crystalline structure of the fresh and the spent catalyst. (See Figure 5.1.) In all patterns, the wide peak at about 26° was assigned to the amorphous peak of reduced graphene oxide (RGO). According to the JCPDS 43-1004 and 65-2902 PDF cards, the diffraction peaks at 36.2°, 42.3° and 61.4° correspond to the CoO facets (111), (200) and (220), respectively. This means that cobalt is present in the fresh catalyst as CoO. (See the patterns shown in CG(F) and RCG(F) in Figure 5.1.) However, the cobalt phase in RCG and CG were very different after the EH reaction. In the RCG(R) pattern, the peaks are assigned to the Co_2C facets (011), (020), (111), (210), (121), (002), (301), (131), (212) and (321) (JCPDS 05-0704). This means that after the EH reaction, the cobalt phase was transformed from CoO to Co_2C. Co and CoO were present in the CG(R) sample, according to the JCPDS 65-2902(CoO) and 15-0806 (Co) PDF cards. Rhodium did not show any peaks in the RCG samples, probably due to the very low loading of only 0.5 wt %. But with the addition of Rh, the cobalt phases were very different after the EH reaction. An unknown peak was also noticed at 21.5°, as shown in the RCG(R) pattern.

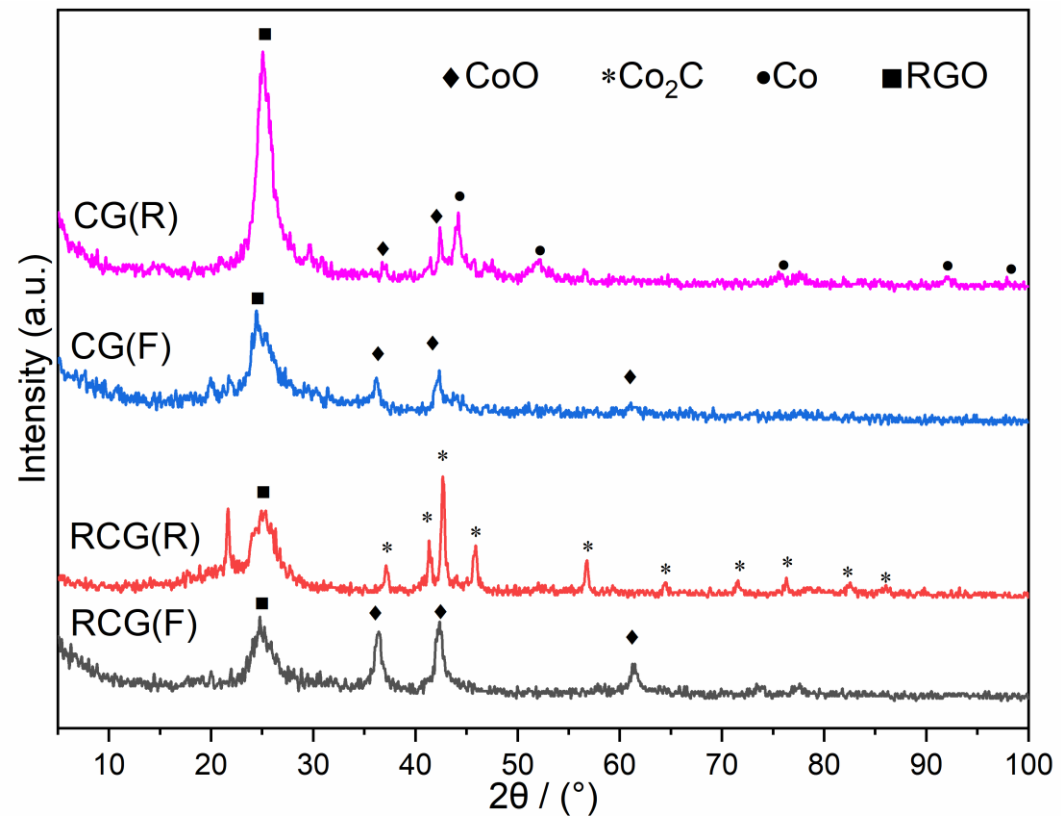

Figure 5.1 XRD patterns of fresh and spent catalysts of cobalt/RGO (CG) and Rh-Co/RGO (RCG). (F) - fresh catalysts; (R) - spent catalysts.

2) TEM

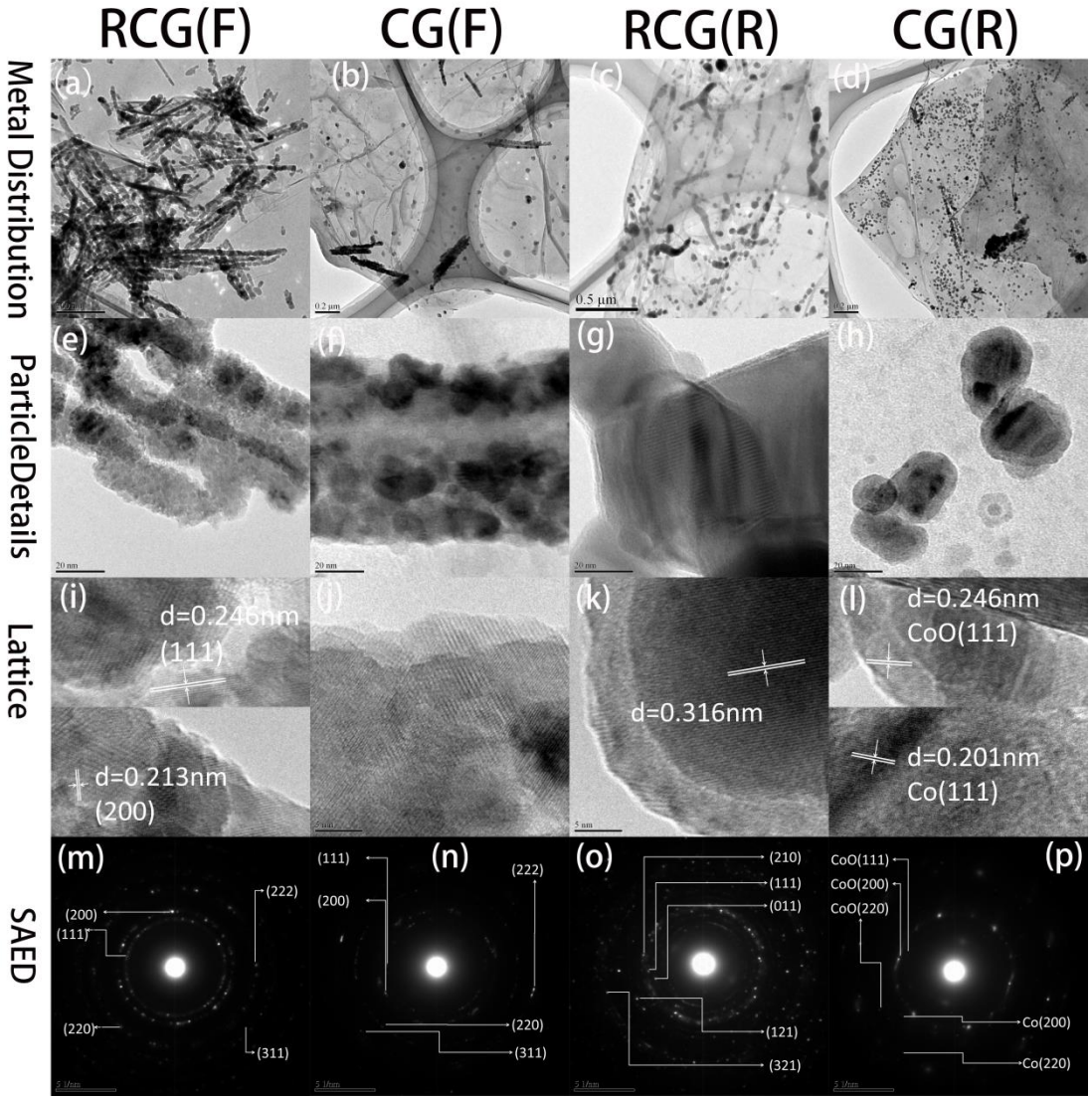

Figure 5.2 TEM images of the fresh and spent catalysts. F) - fresh catalysts; (R) - spent catalysts.

TEM was used to probe the MSI during the EH reaction from the shape, size, exposed crystal planes and dispersion of the metals. The cobalt oxide was well dispersed on RGO, except for the formation of some nanorods and nano-particles. (See CG(F) in Figure 5.2 (b).) With the addition of Rh, the dispersion of cobalt oxide became a disordered stacking of nanorods formed by cobalt oxide particles. (See RCG(F) in Figure 5.2 (a).) More interesting is the dramatically different change after the EH reaction: the well dispersed CoO with some nano-particles on RGO formed finer nano-particles, but sintered some large– particles - the average particle size decreased from 41.56 nm to 22.39 nm. (See Figure 5.2 (d) and (h).) However, with the presence of Rh, the CoO nanorods in RCG(F) were dispersed on RGO after EH. (See Figure 5.2 (c).) In addition, the reduced and reacted cobalt grew to a much larger Co_2C crystal. (See Figure 5.2 (g).) In Figure 5.2, images (i) to (p) show the detailed

lattice patterns and selected area electron diffraction (SAED) patterns, which are consistent with the facets detected by XRD and the parameters in the JCPDS cards. It was also noticed that the lattice pattern in the RCG(R) sample is not assigned to the cobalt carbide facets, and probably corresponds with the unknown lattice peak at 21.5° in the XRD pattern of RCG(R). (See Figure 5.2 (k).)

3) SEM

SEM measurements were taken to investigate the morphology of the metal and the support. With the fresh catalysts, RCG and CG, RGO displayed a disordered twisted-layer structure that formed a three-dimensional network. (See Figure 5.3 (a) and (b)). This coincided with the XRD result that shows a wide peak at about 26°, which is assigned to the amorphous peak of RGO. After the EH reaction, the RGO layers in CG(R) retained the three-dimensional network structure, as shown in Figure 5.3 (d). However, the RGO layers in RCG(R) became even, rather than forming twisted layers, and flat, two-dimensional layers formed. Figure 5.3 (i) to (p) shows the shape of the nanorods and nano-particles seen in the SEM images, which are consistent with the results obtained from TEM. Note that the larger crystal of Co_2C in RCG(R) has a flat plane structure, rather than a particle structure.

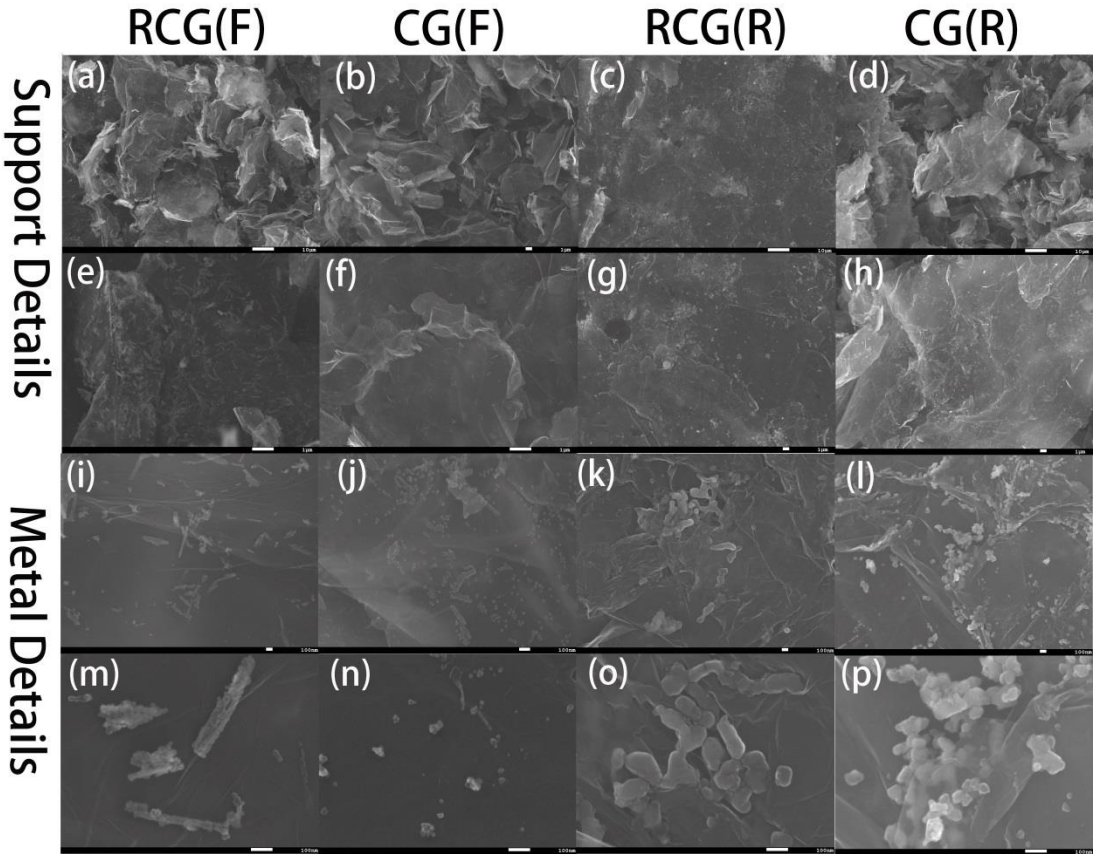

Figure 5.3 SEM images of the fresh and spent catalysts. F) - fresh catalysts; (R) - spent catalysts.

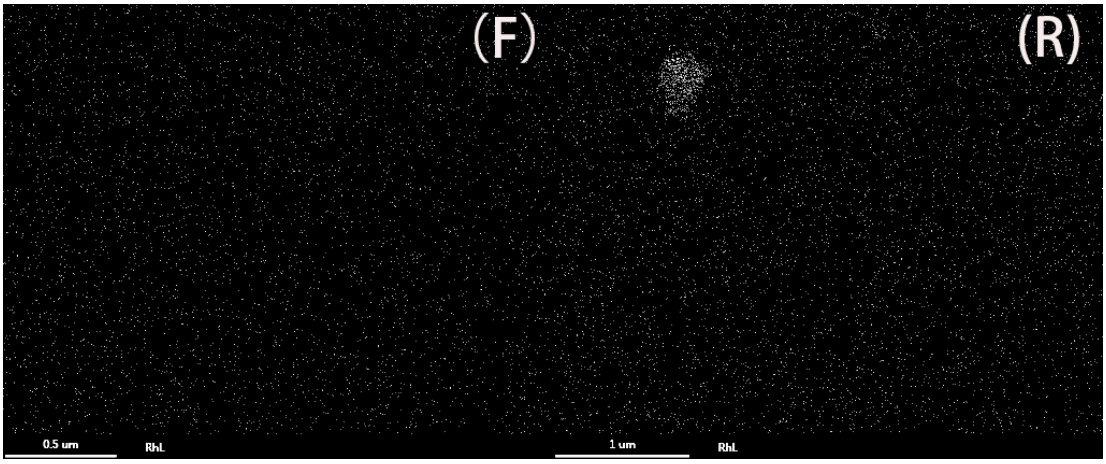

Figure 5.4 SEM-EDS mapping images of Rh in fresh and spent RCG.

SEM-EDS mapping was also performed to investigate the element dispersion - see Figure 5.4, which shows the Rh mapping on RGO. It is well dispersed on the RGO in both the fresh and spent catalysts, except for some agglomeration of Rh in RCG(R), which provides confirmation of rhodium being loaded onto RGO.

The SEM-EDS mapping images of C, O and Co in the fresh and spent catalysts are shown in Figure 5.5. The cobalt element was homogeneously loaded onto RGO in both the fresh and spent catalysts at the micron scale, which indicates that RGO is an ideal support for good dispersion of metals. The comparison shown in Figure 5.5 (e) and (g) indicates that most oxygen atoms were removed during reduction and the EH reaction. However, the oxygen atoms remained in the CG(R), even after the reduction and EH reaction - see Figure 5.5 (f) and (h). This is because of the existence of CoO in CG(R).

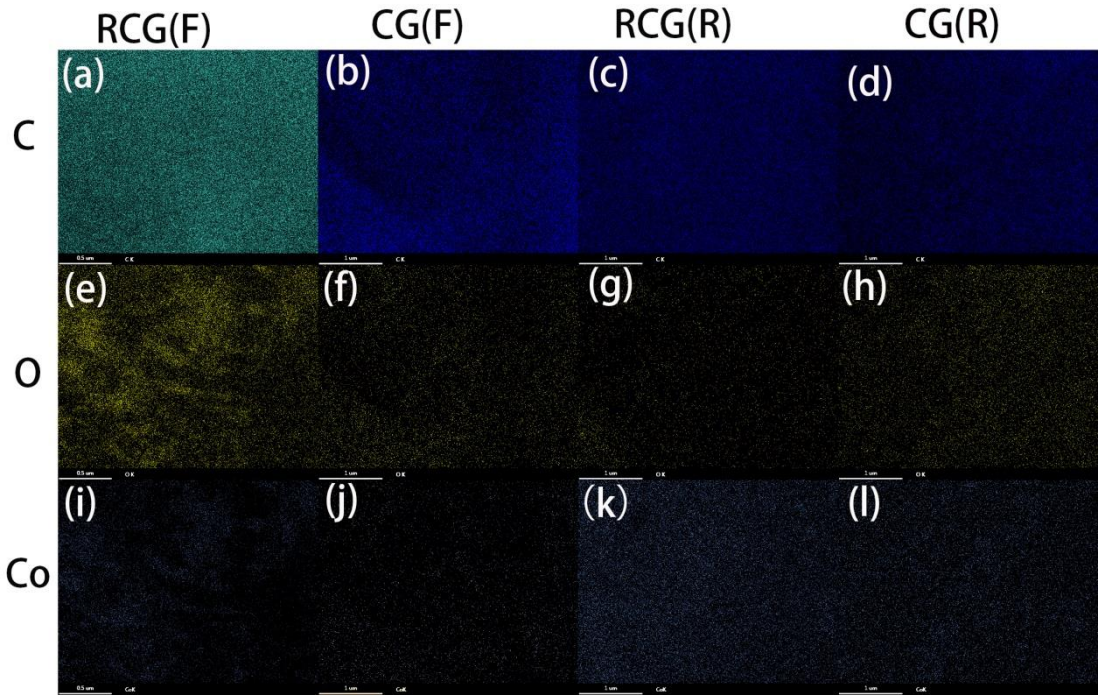

Figure 5.5 SEM-EDS mapping images of C, O and Co in the fresh and spent catalysts. F) - fresh catalysts; (R) - spent catalysts.

4) H_2-TPR

H_2-TPR experiments were performed on the fresh catalysts. The results are shown in Figure 5.6. Reduction of the fresh catalysts started visibly at 283 °C and ended at about 650 °C with both RCG and CG. Moreover, the major reduction peak of RCG was a single peak at 332 °C. However, with the reduction of CG, there were two major peaks: one at 412 °C and another at 438 °C. Figure 5.6 shows that the addtion of Rh promoted the reduction of cobalt oxide on RGO.

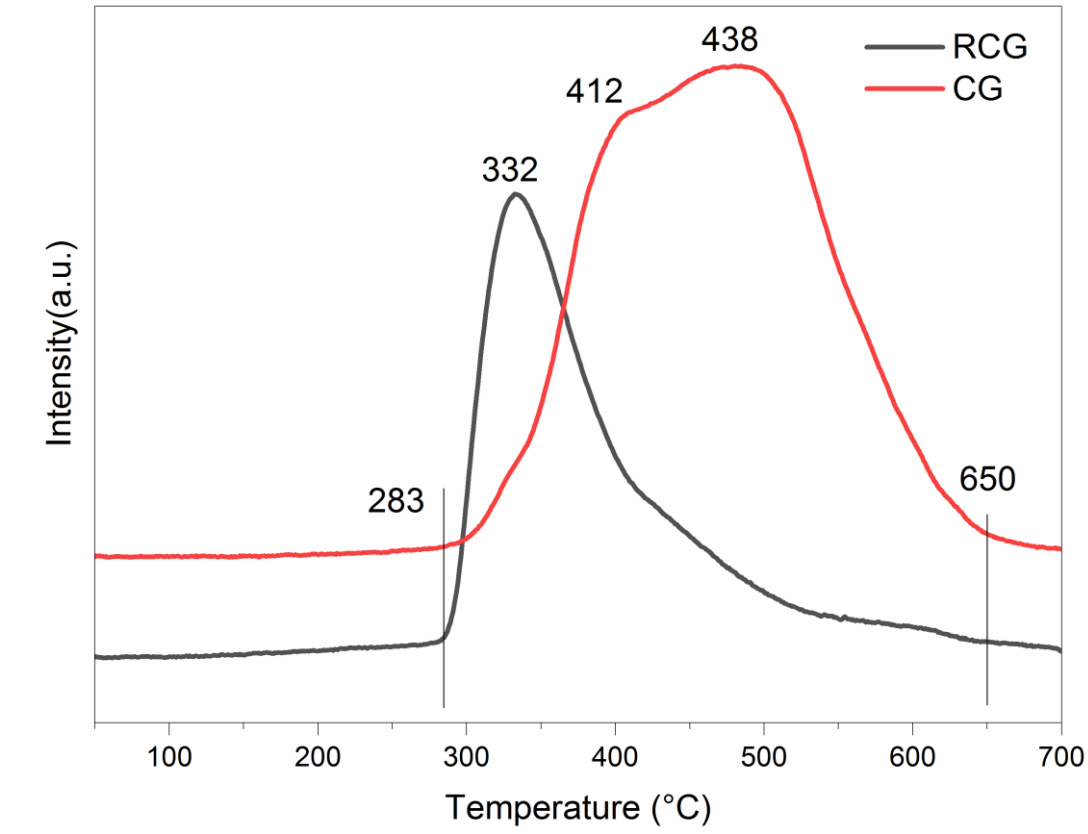

Figure 5.6 H_2-TPR profile of the fresh catalysts RCG and CG.

5) Raman

Raman spectroscopy was applied to observe the structural and electronic change of the support RGO before and after the reactions. The original data was fitted using the Lorentzian method - see Figure 5.7.

It has been reported that the 2D peak is the D-peak overtone and no defect is required for its activation. The 2D band is not observed in the Raman spectra of chemisorbed graphene.[30,31] A comparison of the spectrum of RCG(F) with the spectrum of RCG(R) and CG(F) shows that there is no 2D peak in the spectrum of RCG(F). (See Figure 5.7 (a), (b) and (c)). This means that the rhodium and cobalt in RCG(F) was chemisorbed and more defects existed in RGO. Moreover, the presence of D` in the spectrum of RCG(F) also proves the existence of defects in the RGO of RCG(F), because D` normally appears in the Raman spectrum of defected graphite.[32,33] Therefore, the addition of Rh resulted in more defects being induced on RGO in RCG(F). Furthermore, the metals were chemisorbed on RGO in RCG(F), while cobalt was not chemisorbed in CG(F). After the EH reaction, the defects decreased

and the RGO was restored fairly well. Meanwhile, the metals on RCG(R) were not chemisorbed anymore, as indicated by the presence of a 2D peak and the disappearance of the D` peak.

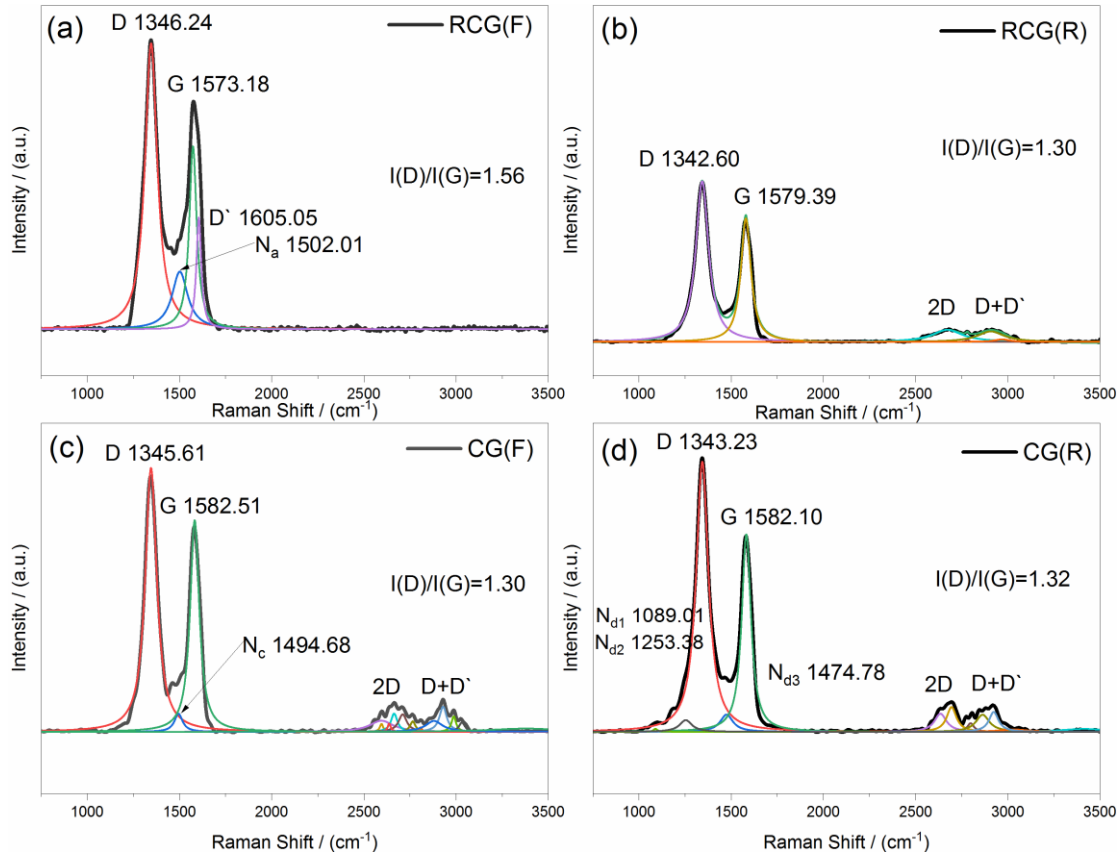

Figure 5.7 Raman spectra of the fresh catalysts and spent catalysts excited at 514 nm laser lines.

The literature [34] indicates that L_D of RGO in both the fresh and spent catalysts (L_D (nm) is the distance between the defects; this is higher than 7 nm. Therefore, the relationships of $I(D)/I(G) \propto 1/L_D^2$ and $I(D)/I(G) \propto n_D^2$ (n_D (cm^{-2}) indicate defect density and can be used to explain the results.[30,34] In the spectrum of fresh catalysts, I(D)/I(G) increased from 1.30 to 1.56 after Rh was added, which means Rh can induce more defects in RGO. (See Figure 5.7 (a) and (c).) After the EH reaction, I(D)/I(G) decreased from 1.56 to 1.30, the same I(D)/I(G) with CG(F). (See Figure 5.7 (a), (b) and (c).) This indicates that the distance between defect L_D increased, while the density of defect n_D decreased. The results of the comparison of I(D)/I(G) are the same as those in the discussion on the 2D peak and the D` peak.

As reported in the literature, doping is proved by a blue-shift in the G peak, and the FWHM (full width at half maximum) of the G peaks decreases significantly with doping.[35] A red-shift of the G peak

from 1573.18 to 1579.39 cm^{-1} and an increase in the FWHM of the G peak from 48.81 to 65.44cm^{-1} were observed in the spectrum of the used catalyst. (See Figure 5.7 (a) and (b) and Table 5.1.). This may indicate a decrease in metal doping on the RGO after reduction and reaction. A comparison of the FWHM of the G peak (Table 5.1) and the G peak positions is shown in Figure 5.7 (a) and (c) - after Rh is added. It shows that the FWHM of G increased from 48.81 to 59.32 cm^{-1} and there was a red-shift from 1573.18 to 1582.51 cm^{-1}. This means that Rh induced more doping sites on RGO in the fresh catalyst.

The peaks labelled N in Figure 5.7 do not belong to RGO or CoO. The Raman result reported in Chapter 4 shows that CoO peaked at 667.94 cm^{-1}. Therefore, the origin of N_c could be due to an interaction between RGO and CoO.[35] (See Figure 5.7 (c).) Similarly, the N_a and N_d peaks shown in Figure 5.7 (a) and (d) were also caused by the interaction between RGO and the corresponding cobalt species. A comparison of N_a with N_c indicates that the intensity of N_a is much higher than that of N_c, which indicates that Rh modified the interaction between RGO and CoO. This is supported by the characterization data obtained by Raman analysis, which shows that the addition of Rh led to a chemisorption of CoO on the RGO surface.

After the EH reaction, the peak indicating the interaction between RGO and Co2C or Rh is disappeared, see Figure 7.5 (b). So with the RCG catalyst, the chemisorbed strong MSI was changed to a weak MSI after the reduction and EH reaction.[36] However, three peaks related to the interaction between RGO and cobalt species existed in the spectrum of CG(R), which possibly originated in the interaction between Co, CoO and the interface of Co-CoO (N_d1-3 in Figure 5.7 (d)). Therefore, with the CG catalyst, MSI was enhanced during reduction and the EH reaction.[36]

Table 5.1. FWHM of the G peak in the Raman spectrum of RCG(F), RCG(R) and CG(F)

Sample	G peak FWHM (cm^{-1})
RCG(F)	48.81
RCG(R)	65.44
CG(F)	59.32

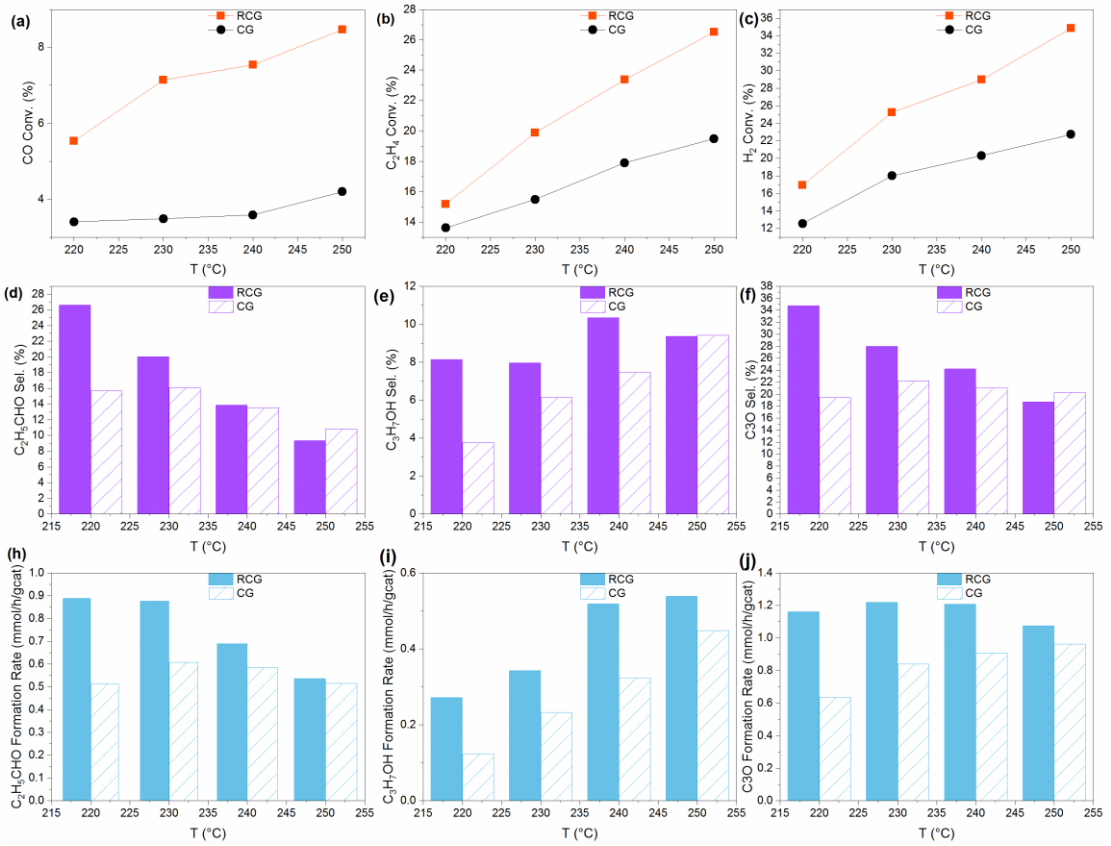

Figure 5.8 EH performance of RCG and CG. (Reaction conditions: P = 2 MPa, GHSV = 1200 h^{-1}, feed-gas ratio: (N_2 : C_2H_4 : CO : H_2 = 1 : 1 : 1 :1). * C_3O = (C_2H_5CHO+C_3H_7OH)).

5.3.2. Catalytic performance

Figure 5.8 provides a summary of the EH catalytic results of RCG and CG. From 220 °C to 240 °C, the conversion of CO, C_2H_4 and H_2, the C_3 oxygenates formation rate and selectivity for RCG are much higher than those of CG. At 220 °C, the C_3 oxygenate formation rate of RCG is twice as high as that of CG, 3.00 mmol/h/g_{cat} and 1.27 mmol/h/g_{cat}. the EH performance of cobalt supported by graphene was significantly enhaced by adding Rh, because the productivity of the target products (C_3 oxygenates) increased.

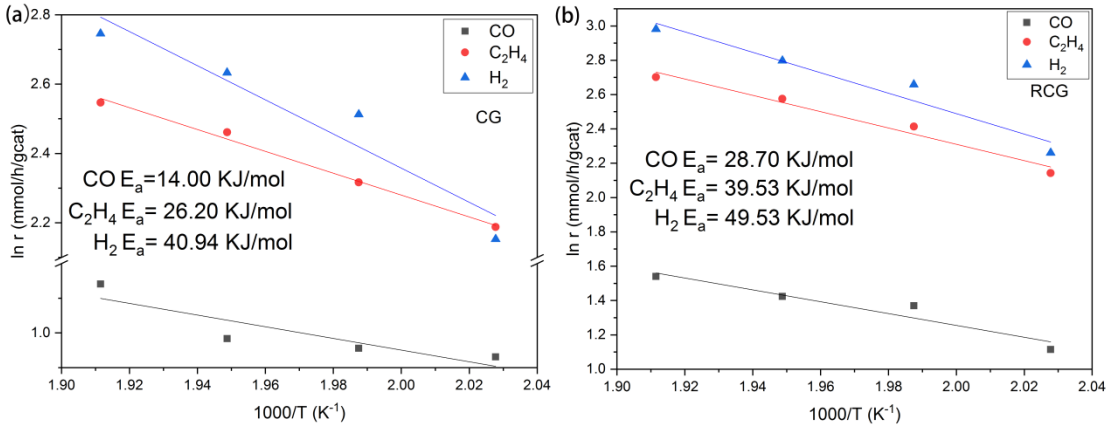

Figure 5.9 Reaction rate of CO, H_2 and C_2H_4 and temperature of CG (a) and the RCG (b) catalyst.

The apparent activation energies of CO, H_2 and C_2H_4 were determined from the Arrhenius diagram shown in Figure 5.9. The apparent activation energies of CO, H_2 and C_2H_4 on the RCG catalyst were higher on the CG catalyst. Hence, the reaction rate of CO hydrogenation to hydrocarbons and EH was lowered, while the reaction rate of EH increased significantly after Rh was loaded on the CG catalyst. This could be the reason for the increase in the C_3 oxygenates selectivity.

5.3.3. Discussion

Figure 5.10 shows a rhodium tuned MSI between RGO and cobalt species during the EH reaction, based on the results of the characterization, when using: the morphology of the metal particles and RGO; the chemical composition; strong MSI. Although CoO was in the original cobalt phase in both RCG(F) and CG(F), it formed different morphologies in

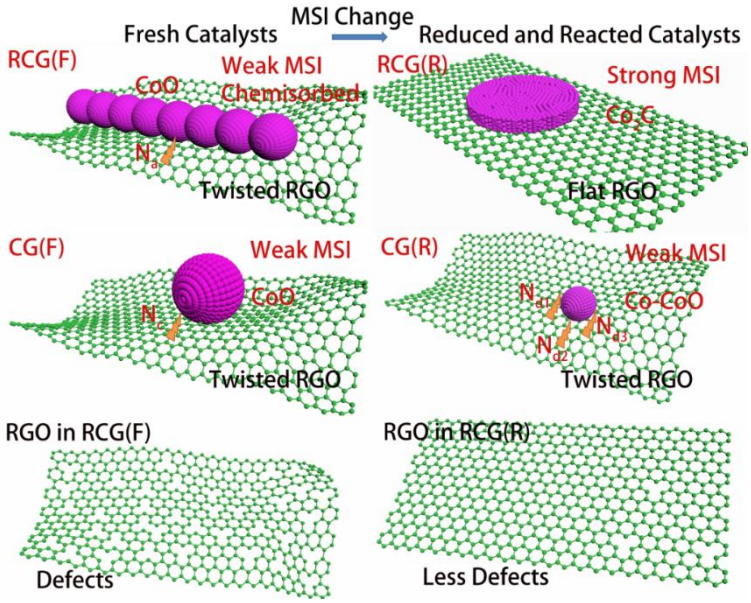

Figure 5.10 Demonstration of MSI between RGO and cobalt before and after EH reaction.

RCG(F) and CG(F), which CoO nanorods formed by CoO particles was presented in RCG(F) and just CoO nano-particles was formed in CG(F). Moreover, the particle size in RCG(F) is even smaller than in CG(F). It has been reported that, in the presence of the graphene interlayer, cobalt forms highly dispersed nanoparticles that are resistant to oxidation, but prone to surface diffusion and agglomeration.[37] But in this work, adding rhodium prevented agglomeration to bigger particles and promoted CoO forming a different nanorod morphology (see Figures 5.2-5.3). Therefore, Rhodium influenced the CoO morphology in fresh catalysts.

Curiously, after the reduction and EH reaction, Co_2C was formed in RCG(R), while a mixture of Co and CoO were present in CG(R). Additionally, along with the different cobalt species in RCG(R) and CG(R), the morphology of cobalt also varied. Co_2C grew to a large flat plane structure in RCG(R) (see Figure 5.3), while Co and CoO formed smaller nano-particles in CG(R) than seen in CG(F). Therefore, it can be concluded that rhodium played an important role in the formation of the active cobalt phase supported on RGO.

Based on the morphology of the cobalt species on RGO in this study, and the conclusions in the literature,[36] the MSI between RGO and the cobalt species in this work can be described as follows: a weak MSI was formed in RCG(F), CG(F) and CG(R), while a strong MSI formed in RCG(R); when

adding rhodium, the MSI exhibited an additional chemisorbed interaction in RCG(F), but not in CG(F); however, the weak MSI in RCG(F) was enhanced to a strong MSI in RCG(R) after the EH reaction; contrarily, the weak MSI in CG(F) remained.

The combined characteristics of RCG(R) indicate that rhodium has a significant effect on the structure of RGO during the EH reaction. The twisted RGO layers with defects seen in RCG(F) became flat RGO layers with fewer defects, which was not found in the CG catalyst. So, after adding rhodium, the structure of RGO is restored nicely. This may be the reason why ethylene can be decomposed to form graphene.[38] And in this work, the RGO structure in RCG was possibly restored by ethylene during the EH reaction.

All rhodium-enhanced MSI in the RCG catalyst led to enhanced EH catalytic performance, while the formation rates and selectivity of the C_3 oxygenates were significantly increased, as shown when the results of the RCG catalyst are compared to those of the CG catalyst.

5.4 Conclusion

MSI between RGO and cobalt species can be enhanced by adding rhodium. After adding rhodium to a reduce graphene oxide-supported cobalt catalyst, the difference from an unpromoted catalyst were seen in: the morphology and particle size of CoO in the fresh catalysts; the MSI in the fresh catalysts; the MSI after the EH reaction; the different active cobalt phases formed during the reaction; the restored RGO structure. All these tuned MSI significantly enhanced the catalytic performance of a reduced graphene-supported cobalt-based catalyst for EH. This provides a powerful methodology for tuning the interaction between graphene and metals to enhance catalytic performance. Additionally, a new heterogeneous EH was developed in this work, and its potential uses in industry are indicated.

References

[1] C. Li, W. Wang, L. Yan, Y. Ding, A mini review on strategies for heterogenization of rhodium-based hydroformylation catalysts, Front. Chem. Sci. Eng. (12)1(2018)113-123. https://doi.org/https://doi.org/10.1007/s11705-017-1672-9.

[2] X. Wang, Recent advances in continuous rhodium-catalyzed hydroformylation, J. Flow Chem. 5 (2015) 125–132. https://doi.org/10.1556/1846.2015.00003.

[3] Â.C.B. Neves, M.J.F. Calvete, T.M.V.D. Pinho E Melo, M.M. Pereira, Immobilized catalysts for hydroformylation reactions: A versatile tool for aldehyde synthesis, European J. Org. Chem. (2012) 6309–6320. https://doi.org/10.1002/ejoc.201200709.

[4] H. Xiong, L.L. Jewell, N.J. Coville, Shaped carbons as supports for the catalytic conversion of syngas to clean fuels, ACS Catal. 5 (2015) 2640–2658. https://doi.org/10.1021/acscatal.5b00090.

[5] Y. Zhang, H.-B. Zhang, G.-D. Lin, P. Chen, Y.-Z. Yuan, K.R. Tsai, Preparation, characterization and catalytic hydroformylation properties of carbon nanotubes-supported Rh–phosphine catalyst, Appl. Catal. A Gen. 187 (1999) 213–224. https://doi.org/10.1016/S0926-860X(99)00229-X.

[6] H. Zhang, Y. Zhang, G. Lin, Y. Yuan, K.R. Tsai, Carbon nanotubes-supported Rh-phosphine complex catalysts for propene hydroformylation, Studies in Surface Science and Catalysis (2010) 3885–3890.

[7] J. Qiu, H. Zhang, X. Wang, B. Yin, Hydroformylation of 1-octene over carbon nanotube supported cobalt catalyst, ACS Div. Fuel Chem. Prepr. 49 (2004) 940–941.

[8] H. Sakagami, N. Ohta, S. Endo, T. Harada, N. Takahashi, Location of active sites for 3-pentanone formation during ethene hydroformylation on Rh / active-carbon catalysts, J. Catal. 171 (1997) 449–456.

[9] X. Song, Y. Ding, W. Chen, W. Dong, Y. Pei, J. Zang, L. Yan, Y. Lu, Formation of 3-pentanone via ethylene hydroformylation over Co/activated carbon catalyst, Appl. Catal. A Gen. 452 (2013) 155–162. https://doi.org/10.1016/j.apcata.2012.11.006.

[10] B. Li, X. Li, K. Asami, K. Fujimoto, Low-pressure hydroformylation of middle olefins over Co and Rh supported on active carbon catalysts, Energy Fuels. 17 (2003) 810–816.

[11] R. Gao, C.D. Tan, R.T.K. Baker, Ethylene hydroformylation on graphite nanofiber supported rhodium catalysts, Catal. Today. 65 (2001) 19–29. https://doi.org/10.1016/S0920-5861(00)00541-1.

[12] V. Singh, D. Joung, L. Zhai, S. Das, S.I. Khondaker, S. Seal, Graphene based materials: Past, present and future, Prog. Mater. Sci. 56 (2011) 1178–1271. https://doi.org/10.1016/j.pmatsci.2011.03.003.

[13] M. Tan, Y. Ishikuro, Y. Hosoi, N. Yamane, P. Ai, P. Zhang, G. Yang, M. Wu, R. Yang, N. Tsubaki, PPh 3 functionalized Rh / rGO catalyst for heterogeneous hydroformylation: Bifunctional reduction of graphene oxide by organic ligand, Chem. Eng. J. (2017). https://doi.org/10.1016/j.cej.2017.08.023.

[14] Y. V. Ioni, S.E. Lyubimov, V.A. Davankov, S.P. Gubin, Modified graphene oxide as a support for rhodium nanoparticles active in olefin hydroformylation*, Russ. Chem. Bull. Int. Ed. 63 (2014) 2243–2249.

[15] M. Tan, G. Yang, T. Wang,et al. Active and regioselective rhodium catalyst supported on reduced graphene oxide for 1-hexene hydroformylation, Catal. Sci. Technol. (2015) 1162–1172. https://doi.org/10.1039/C5CY01355K.

[16] J.A. Farmer, C.T. Campbell, Ceria maintains smaller metal catalyst particles by strong metal-support bonding, Science (80). 329 (2010) 933. https://doi.org/10.1126/science.1191778.

[17] G.R. Jenness, J.R. Schmidt, Unraveling the role of metal−support interactions in heterogeneous catalysis: Oxygenate selectivity in Fischer−Tropsch Synthesis, (2013).

[18] H. Wan, B. Wu, H. Xiang, Y. Li, Fischer-Tropsch Synthesis: Influence of support incorporation

manner on metal dispersion, metal-support interaction, and activity of iron catalysts, ACS Catal. 2 (2012) 1877–1883. https://doi.org/10.1021/cs200584s.

[19] R. Thalinger, T. Götsch, C. Zhuo, W. Hetaba, W. Wallisch, M. Stöger-Pollach, D. Schmidmair, B. Klötzer, S. Penner, Rhodium-catalyzed methanation and methane steam reforming reactions on rhodium–perovskite systems: Metal–support interaction, ChemCatChem. 8 (2016) 2057–2067. https://doi.org/10.1002/cctc.201600262.

[20] T.W. van Deelen, C. Hernández Mejía, K.P. de Jong, Control of metal-support interactions in heterogeneous catalysts to enhance activity and selectivity, Nat. Catal. 2 (2019) 955–970. https://doi.org/10.1038/s41929-019-0364-x.

[21] M. Ahmadi, H. Mistry, B. Roldan Cuenya, Tailoring the catalytic properties of metal nanoparticles via support interactions, J. Phys. Chem. Lett. 7 (2016) 3519–3533. https://doi.org/10.1021/acs.jpclett.6b01198.

[22] Y. Tang, J. Lai, Y. Chao, M. Luo, F. Lin, J. Zhou, D. Su, Strengthening reactive metal-support interaction to stabilize high-density Pt single atoms on electron-deficient g-C_3N_4 for boosting photocatalytic H_2 production, NANOEN (2018). https://doi.org/10.1016/j.nanoen.2018.11.033.

[23] S. Penner, M. Armbrüster, Formation of intermetallic compounds by reactive metal–support interaction: A frequently encountered phenomenon in catalysis, ChemCatChem. 7 (2015) 374–392. https://doi.org/10.1002/cctc.201402635.

[24] C.-J. Pan, M.-C. Tsai, W.-N. Su, J. Rick, N.G. Akalework, A.K. Agegnehu, S.-Y. Cheng, B.-J. Hwang, Tuning/exploiting strong metal-support interaction (SMSI) in heterogeneous catalysis, J. Taiwan Inst. Chem. Eng. 74 (2017) 154–186. https://doi.org/https://doi.org/10.1016/j.jtice.2017.02.012.

[25] C. Hernández Mejía, T.W. van Deelen, K.P. de Jong, Activity enhancement of cobalt catalysts by tuning metal-support interactions, Nat. Commun. 9 (2018) 1–8. https://doi.org/10.1038/s41467-018-06903-w.

[26] K.K.& T.U. A. Maeda, F. Yamakawa, Effect of strong metal-support interaction (SMSI) on

ethylene hydroformylation over niobia-supported palladium catalysts, Catal Lett. 4 (1990) 107–112.

[27] L. Huang, Y. Xu, G. Piao, A. Liu, Enhancement of olefin hydroformylation related to supported bimetallic Rh-Co clusters, Catal. Letters. 23 (1994) 87–95.

[28] R. Franke, D. Selent, A. Borner, Applied hydroformylation, Chem. Rev. 112 (2012) 5675–5732. https://doi.org/10.1021/cr3001803.

[29] N. Huang, B. Liu, X. Lan, T. Wang, Insights into the bimetallic effects of a RhCo catalyst for ethene hydroformylation: Experimental and DFT investigations, Ind. Eng. Chem. Res. 59 (2020) 18771–18780. https://doi.org/10.1021/acs.iecr.0c03437.

[30] A.C. Ferrari, D.M. Basko, Raman spectroscopy as a versatile tool for studying the properties of graphene, Nat. Nanotechnol. 8 (2013) 235–246. https://doi.org/10.1038/nnano.2013.46.

[31] D.Y. Usachov, V.Y. Davydov, V.S. Levitskii, V.O. Shevelev, D. Marchenko, B. V. Senkovskiy, O.Y. Vilkov, A.G. Rybkin, L. V. Yashina, E. V. Chulkov, I.Y. Sklyadneva, R. Heid, K.P. Bohnen, C. Laubschat, D. V. Vyalikh, Raman spectroscopy of lattice-matched graphene on strongly interacting metal surfaces, ACS Nano. 11 (2017) 6336–6345. https://doi.org/10.1021/acsnano.7b02686.

[32] D.M. Basko, S. Piscanec, A.C. Ferrari, Electron-electron interactions and doping dependence of the two-phonon Raman intensity in graphene, Phys. Rev. B. 80 (2009) 1–10. https://doi.org/10.1103/physrevb.80.165413.

[33] W. Luo, S. Zafeiratos, Tuning morphology and redox properties of cobalt particles supported on oxides by an in-between graphene layer, J. Phys. Chem. C. 120 (2016) 14130–14139. https://doi.org/10.1021/acs.jpcc.6b03595.

[34] L.G. Cançado, A. Jorio, E.H.M. Ferreira, F. Stavale, C.A. Achete, R.B. Capaz, M.V.O. Moutinho, A. Lombardo, T.S. Kulmala, A.C. Ferrari, Quantifying defects in graphene via Raman spectroscopy at different excitation energies, Nano Lett. 11 (2011) 3190–3196. https://doi.org/10.1021/nl201432g.

[35] I. Serrano-Esparza, J. Fan, J.M. Michalik, L.A. Rodríguez, M.R. Ibarra, J.M. de Teresa, The nature of graphene-metal bonding probed by Raman spectroscopy: The special case of cobalt, J. Phys. D. Appl. Phys. 49 (2016). https://doi.org/10.1088/0022-3727/49/10/105301.

[36] B. Zhang, D.S. Su, Probing the metal-support interaction in carbon-supported catalysts by using electron microscopy, ChemCatChem. 7 (2015) 3639–3645. https://doi.org/10.1002/cctc.201500666.

[37] W. Luo, W.H. Doh, Y.T. Law, F. Aweke, A. Ksiazek-Sobieszek, A. Sobieszek, L. Salamacha, K. Skrzypiec, F. Le Normand, A. MacHocki, S. Zafeiratos, Single-layer graphene as an effective mediator of the metal-support interaction, J. Phys. Chem. Lett. 5 (2014) 1837–1844. https://doi.org/10.1021/jz500425j.

[38] A.J. Martínez-Galera, I. Brihuega, J.M. Gómez-Rodríguez, Ethylene irradiation: A new route to grow graphene on low reactivity metals, Nano Lett. 11 (2011) 3576–3580. https://doi.org/10.1021/nl201281m.

Chapter 6: Influence of feed-gas composition on ethene hydroformylation using a Rh-Co bimetallic catalyst supported on reduced graphene oxide

Abstract

The influence of feed-gas composition on the performance of ethene hydroformylation (EH) over a Rh-Co bimetallic catalyst supported on reduced graphene oxide (RGO) was investigated using a tubular fixed bed reactor (TFBR). Argon was used as the balance gas when the feed-gas ratio was changed, to keep the partial pressure of the other two gases constant, while the ratio of one component in the feed-gas was changed. First, the effect of single component gas ratio to the performance of EH was studied one by one (H_2, C_2H_4 and CO). Then an optimized ratio was found to obtain a high selectivity to C_3 oxygenates. The results showed that:

- 0.5%Rh-20%Co/RGO is a promising heterogeneous catalyst for EH.
- H_2 and CO have more influence on selectivity to oxygenates than does C_2H_4.
- A lower H_2 ratio and a higher CO ratio in feed-gas can lead to higher selectivity to oxygenates.
- The highest selectivity to oxygenates, 61.70%, was obtained at a feed-gas ratio of CO : C_2H_4 : H_2 = 4 : 2 : 1 with 17.53% C_2H_4 conversion.

6.1 Introduction

Hydroformylation is a catalysed reaction that can convert olefins with syngas to aldehydes. The aldehydes that form are valuable final products and intermediates in the synthesis of bulk chemicals like alcohols, esters and amines.[1] The hydroformylation process is the most common homogeneous process used in industry, as it has high selectivity (well in excess of 95%) to oxygenates when using an optimal choice of reaction parameters and process conditions.[2] The aldehydes can be manufactured stoichiometrically by adding carbon monoxide and hydrogen to olefins in one step with 100% atom efficiency.[3] However, the homogeneous process cannot avoid its intrinsic differences like catalyst loss, catalyst separation and recycling, the high cost of a rhodium-based catalyst, and metal species contamination in the aldehydes products.[4]

It is for these reasons that much effort has been made to fulfil the hydroformylation in a heterogeneous process using solid catalysts. One type of solid catalyst is immobilization of the homogeneous metal complex catalyst on various supports by physical adsorption, hydrogen bonding, or chemical anchoring.[5] The other type is a supported metal catalyst that is prepared by means of reduction or decomposition of a precursor (metal salt, oxide or complex) on a carrier (SiO_2, Al_2O_3, carbon, etc.).[6] For EH carried out in a continuous fixed bed reactor (FBR), the feed-gas ratio in most published work involved the stoichiometric ratio - normally C_2H_4:CO:H_2 =1:1:1.[7–16] Furthermore, the hydroformylation selectivity to oxygenates in most published work is far from 100%, except for Jiang et al.,[17] who reported that the highest selectivity to propanal was 99.9% when using a $Rh(CO)_2(acac)/SiO_2$ catalyst at a feed-gas ratio of (C_2H_4:CO:H_2 = 1:1:1).

The major side reaction in EH is hydrogenation. Due to this side reaction, the reaction rate of each component in the feed-gas cannot be maintained at the stoichiometric ratio of the hydroformylation reaction. Therefore, it is crucial to investigate the influence of the feed-gas ratio to the hydroformylation performance, however, very few studies have focused on the influence of the feed-gas ratio. Navidi et al. [18] reported on the Rh based catalyst a higher ethylene ratio in feed-gas have a more pronounced effect on the CO conversion and the production of oxygenates compared with increase the ratio of the other reactants. Gao et al. [19] studied a graphite nanofiber supported Rhodium catalysts that showed that a high partial pressure of CO and C_2H_4, and a concomitant low partial pressure of H_2 can increase the selectivity to oxygenates. The similar result that beneficial effects on the selectivity were observed at high CO partial pressure was also reported on.[20] In pursuit of an optimum performance, the influence of feed-gas ratio on the EH using a Rh-Co bimetallic supported on RGO was systematically studied in a fixed bed micro reactor. The catalyst reactivity, selectivity and productivity were measured and compared.

6.2 Experimental

6.2.1 Catalyst preparation

The preparation method used for graphene oxide (GO) and 0.5%Rh-20%Co/rGO followed the same procedure as detailed in Chapter 5.

6.2.2 Catalytic performance

The performance of the catalysts was evaluated using a fixed-bed reactor with an internal diameter of 8 mm and a length 380 mm. 0.5 g 0.5%-20%Co/RGO catalyst was loaded into the reactor and reduced with H_2 (AFROX (African Oxygen) Ltd.- 99.999%) at 330 °C, 1 bar, 30 ml/min for 20 h. Experiments were then done using different feed-gases and different conditions, as detailed in Table 6.1. N_2 was used as the internal standard for mass balance calculations and Ar was used as the balance gas when the partial pressure of one reactant gas was decreased. All the gas flow rates were controlled using a Brooks 5850 instrument. All the feed-gas, calibration gas and products were analyzed using an online Agilent 7890B GC. The oxygenates and hydrocarbons were separated by a CP-Sil 5CB (25m x 0.15mm x 2.0 µm) column and analyzed using a flame ionization detector (FID). The other gases were analyzed using a thermal conductivity detector (TCD).

6.2.3 Calculations

Reaction rate:

$$-r_x = \frac{F_{x,in} - F_{x,out}}{m_{cat}} \qquad (6.1)$$

Where: $F_{x,in}$ is the molar flow rate of component x in the feed-gas, mmol/h; $F_{x,out}$ is the molar flow rate of component x in the tail-gas, mmol/h; m_{cat} is the mass of catalyst loaded into the reactor, g; r_x is the reaction rate of component x, mmol/h/gcat; x is one of the components in the feed-gas (CO, H_2, C_2H_4).

Conversion:

$$x_{conv} = \left(\frac{F_{x,in} - F_{x,out}}{F_{x,in}}\right) \times 100\% \qquad (6.2)$$

Where: $F_{x,in}$ is the molar flow rate of component x in the feed-gas, mmol/h; $F_{x,out}$ is the molar flow rate of component x in the tail-gas, mmol/h; x_{conv} is the conversion of component x, %; x is one of the components in the feed-gas (CO, H_2, C_2H_4).

Selectivity based converted C_2H_4:

$$S_{x,C_2H_4} = \left(\frac{F_{x,out}}{F_{C_2H_4,in} - F_{C_2H_4,out}}\right) \times 100\% \qquad (6.3)$$

Where: $F_{x,out}$ is the molar flow rate of product x in the tail-gas, mmol/h; $F_{C_2H_4,in}$ is the molar flow rate of C_2H_4 in the feed-gas, mmol/h; $F_{C_2H_4,out}$ is the molar flow rate of C_2H_4 in the tail-gas, mmol/h; S_{x,C_2H_4} is the selectivity of product x based on converted C_2H_4, %; x is C_2H_6 or C_2H_5CHO or C_3H_7OH.

Selectivity based on total converted carbon from CO and C_2H_4:

$$S_{x,carbon} = \left[\frac{n \times F_{x,out}}{2 \times (F_{C_2H_4,in} - F_{C_2H_4,out}) + (F_{CO,in} - F_{CO,out})}\right] \times 100\% \qquad (6.4)$$

Where: $F_{x,out}$ is the molar flow rate of product x in the tail-gas, mmol/h; $F_{C_2H_4,in}$ is the molar flow rate of C_2H_4 in the feed-gas, mmol/h; $F_{C_2H_4,out}$ is the molar flow rate of C_2H_4 in the tail-gas, mmol/h; $F_{CO,in}$ is the molar flow rate of CO in the feed-gas, mmol/h; $F_{CO,out}$ is the molar flow rate of CO in the tail-gas, mmol/h; n is the carbon number in product x; $S_{x,carbon}$ is the selectivity of product x based on total converted carbon from CO and C_2H_4, %; x is C_2H_6 or C_2H_5CHO or C_3H_7OH.

Selectivity based on converted CO:

$$S_{x,CO} = \left(\frac{F_{x,out}}{F_{CO,in} - F_{CO,out}}\right) \times 100\%$$

Where: $F_{x,out}$ is the molar flow rate of product x in the tail-gas, mmol/h; $F_{CO,in}$ is the molar flow rate of CO in the feed-gas, mmol/h; $F_{CO,out}$ is the molar flow rate of CO in the tail-gas, mmol/h; $S_{x,CO}$ is the selectivity of product x based on CO, %; x is C_2H_6 or C_2H_5CHO or C_3H_7OH.

Table 6.1 Reaction conditions and feed-gas ratio for EH over a Rh-Co bimetallic catalyst

Group	Run	$CO:C_2H_4:H_2$	T (℃)	Total P (bar)	Flow rate (ml(NTP/mi)	N_2 Ar	Partial Pressure (bar) CO	C_2H_4	H_2	
A	1	1:1:1	250	20	60	5.00	5.00	5.00	5.00	0.00
	2	1:1:0.67	250	20	60	5.00	5.00	5.00	3.33	1.67
	3	1:1:0.5	250	20	60	5.00	5.00	5.00	2.50	2.50
	4	1:1:0.33	250	20	60	5.00	5.00	5.00	1.67	3.33
	5	1:1:0.2	250	20	60	5.00	5.00	5.00	1.00	4.00
B	6	1:1:1	250	20	60	5.00	5.00	5.00	5.00	0.00
	7	1:0.67:1	250	20	60	3.33	5.00	3.33	5.00	3.33
	8	1:0.5:1	250	20	60	2.50	5.00	2.50	5.00	5.00
	9	1:0.33:1	250	20	60	1.67	5.00	1.67	5.00	6.67
	10	1:0.2:1	250	20	60	1.00	5.00	1.00	5.00	8.00
C	11	1:1:1	250	20	60	5.00	5.00	5.00	5.00	0.00
	12	0.67:1:1	250	20	60	5.00	3.33	5.00	5.00	1.67
	13	0.5:1:1	250	20	60	5.00	2.50	5.00	5.00	2.50
	14	0.33:1:1	250	20	60	5.00	1.67	5.00	5.00	3.33
	15	0.2:1:1	250	20	60	5.00	1.00	5.00	5.00	4.00
D	16	1:1:1	250	20	60	5.00	5.00	5.00	5.00	0.00
	17	2:1:1	250	20	60	4.00	8.00	4.00	4.00	0.00
	18	4:2:1	250	20	60	4.00	8.00	4.00	2.00	2.00

6.3 Results and Discussion

Table 6.1 lists the 18 experimental runs that were conducted in the current research, with a reaction temperature of 250 °C, a total flow rate of 60 ml (NTP/min) and total pressure of 20 bar. These experimental runs were divided into four groups: (1) Group A (Runs 1-5) to investigate the effect of partial pressure of H_2; (2) Group B (Runs 6-10) to investigate the effect of partial pressure of C_2H_4; (3) Group C (Runs 11-15) to investigate the effect of partial pressure of CO; and (4) Group D (Run 16-18) to test the optimal reaction conditions.

6.3.1 Effect of H_2 partial pressure

With Group A, the partial pressure of CO and C_2H_4 were kept at a constant 5 bar, while the partial pressure of H_2 was adjusted from 1 bar to 5 bar, with the balance of the inert gas being ($Ar+N_2$). (See Table 6.1.) Figure 6.1 shows the effect of H_2 partial pressure on the EH performance of a 0.5%Rh-20%Co/RGO, regarding aspects such as conversion, reaction rate, product formation rate and selectivity. The x-axis in Figure 6.1 shows the ratio of the three reactants ($CO/C_2H_4/H_2$). It shows that only the ratio of H_2 to the other two reactants was changed by adjusting the partial pressure of H_2 and the inert gas.

Figure 6.1 (a) shows that the H_2 conversion first increased as the ratio of H_2 to CO (or C_2H_4) in the feed-gas decreased from 1 to 0.33; then the H_2 conversion dropped a little, as the ratio decreased further to 0.2. CO and C_2H_4 conversion exhibited the same trend when the H_2 ratio in the feed was decreased: the conversion rose as the H_2 ratio decreased from 1 to 0.67, then dropped, with the H_2 ratio decreasing from 0.67 to 0.2. A similar trend was seen with the CO and C_2H_4 reaction rates, as shown in Figure 6.1 (b). The H_2 reaction rate did not change much when the H_2 ratio in the feed decreased from 1 to 0.5, but the H_2 reaction rate dropped dramatically as the H_2 ratio in the feed-gas decreased from 0.5 to 0.2. This could be the explanation for the trend seen with H_2 conversion: when the H_2 ratio is higher than 0.5, the H_2 reaction rate did not change much; when the amount of H_2 in the feed-gas decreased, the converted amount of H_2 remained almost stable, so the H_2 conversion kept increasing until the H_2 ratio decreased to 0.33; after the H_2 ratio dropped to 0.33, the reaction rate also declined because the low partial pressure of H_2 limited the reaction rate.

Figure 6.1 (c) shows that the formation rate of C_2H_5CHO and C_3H_7OH both peaked at an H_2 ratio of 0.67. Except the formation rates of C_2H_5CHO and C_3H_7OH at the H_2 ratio of 0.5 were close to the peak point at H_2 ratio of 0.67, the C_3 oxygenates formation rates were much lower than the formation rate at an H_2 ratio of 0.67. Figure 6.1(d) shows that the selectivity of the main side reaction, ethene hydrogenation, was much higher than EH with the runs for Group A. Figure 6.1 (e) indicates that the highest selectivity of C_3 oxygenates to converted carbon was obtained at an H_2 ratio of 0.5. In Figure 6.1 (f), it can be seen the selectivity of the C_3 oxygenates is higher than 50% for the 5 runs, which

indicates that the selectivity of EH is higher than the side reaction of CO hydrogenation (CO + $2H_2$ = -CH_2- + H_2O). The highest CO selectivity to EH was obtained with a ratio of CO/C2H4/H2 at 1:1:0.5.

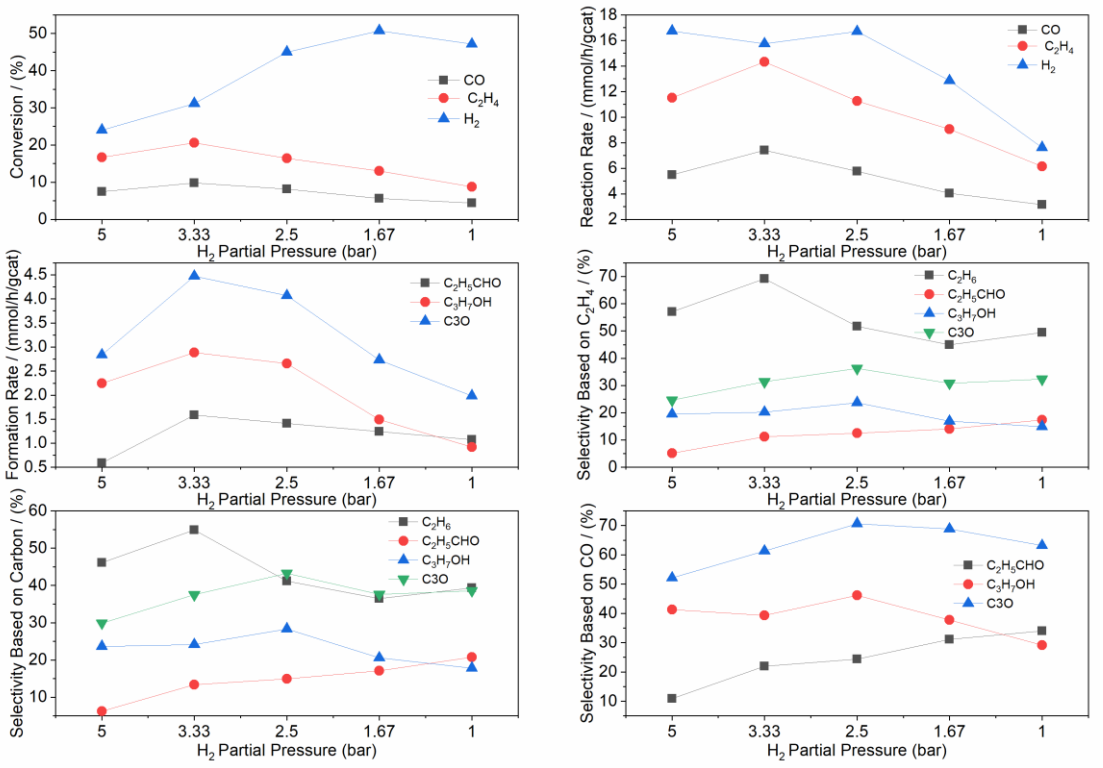

Figure 6.1 Catalytic activity and selectivity as a function of H_2 partial pressure for EH. Reaction conditions: P = 20 bar, T = 250 ℃, GHSV = 1200 h^{-1} with a feed-gas mixture of CO/C_2H_4/H_2/N_2/Ar. (The partial pressure of CO and C_2H_4 are indicated at a constant pressure of 5 bar each.)

In summary, the partial pressure of H_2 significantly influence the catalytic activity and selectivity for both the main reaction (hydroformylation) and the side reactions (hydrogenation). When combining the results of the product formation rates and selectivity of C_3 oxygenates, the ratio of CO:C_2H_4:H_2 = 1:1:0.5 could be an optimal condition for EH when using a 0.5%Rh-20%Co/RGO catalyst.

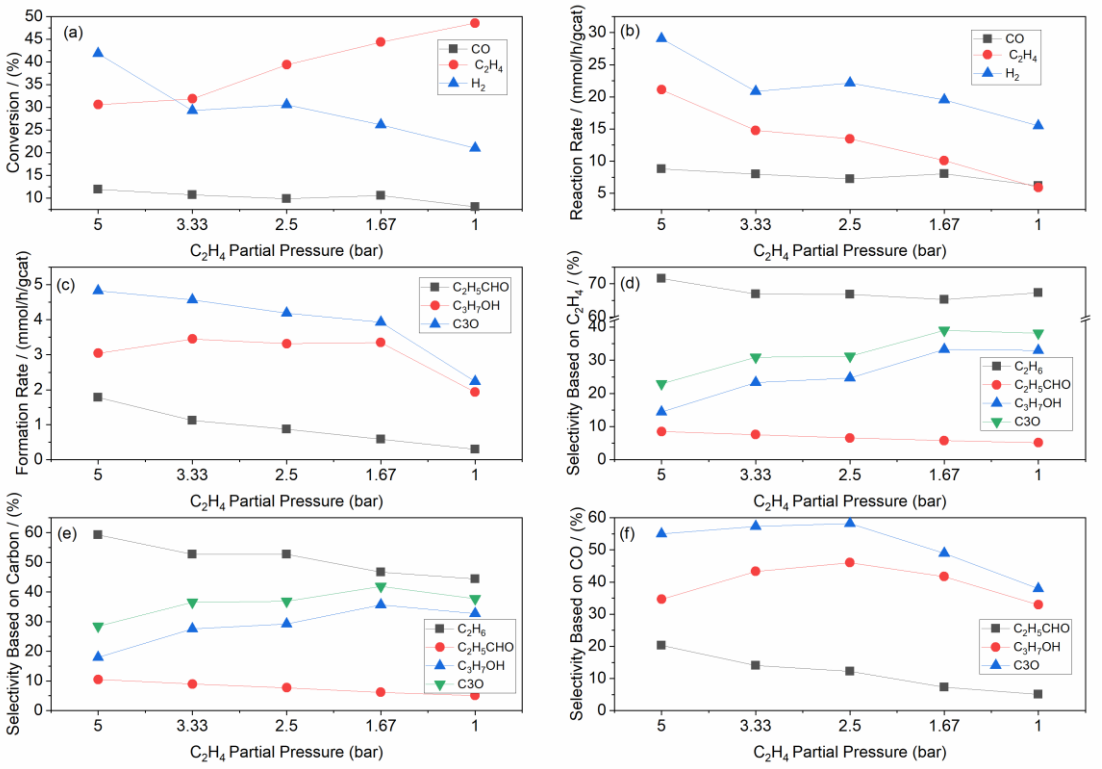

Figure 6.2 Catalytic activity and selectivity as a function of C_2H_4 partial pressure for EH. Reaction conditions: P = 20 bar, T = 250 ℃, GHSV = 1200 h^{-1} with a feed-gas mixture of CO/C_2H_4/H_2/N_2/Ar. (The partial pressure of CO and H_2 are indicated at a constant pressure of 5 bar each.)

6.3.2 Effect of C_2H_4 partial pressure

In Group B, the partial pressure of CO and H_2 were kept constant at 5 bar, while the partial pressure of C_2H_4 was adjusted from 1 bar to 5 bar with the balance of the inert gas being (Ar+N_2). (See Table 6.1.) Figure 6.2 provides a summary of the effect of C_2H_4 partial pressure on the performance of EH using a 0.5%Rh-20%Co/RGO catalyst. When the C_2H_4 partial pressure decreased, the conversion of C_2H_4 exhibited an upward trend, as shown in Figure 6.2 (a); however, there was a downward trend in the reaction rate of C_2H_4, as shown in Figure 6.2 (b). There was a sudden drop in H_2 conversion when the C_2H_4 ratio decreased from 1 to 0.67, but the H_2 conversion did not change much when the C_2H_4 ratio changed from 0.67 to 0.33. Finally, the conversion of H_2 declined further after the C_2H_4 ratio decreased to 0.2. The same trend was found in the reaction rate of H_2. However, both the conversion rate and the reaction rate of CO were almost stable as the C_2H_4 ratio changed from 1 to 0.33. (See Figure 6.2 (a) and (b).) At a low C_2H_4 ratio of 0.2, both the conversion rate and the reaction rate of CO dropped moderately. This suggests that the CO conversion rate and the reaction rate are not sensitive to a change in C_2H_4 partial pressure. Also, the change in C_2H_4 partial pressure affects the H_2

conversion rate and the reaction rate significantly only at a high ratio of C_2H_4. When the C_2H_4 ratio is below 0.67, the effect of the C_2H_4 ratio on H_2 conversion and the reaction rate is slight.

Figure 6.2 (c) shows that the formation rate of C_3H_7OH remained steady in the range of 3.04 to 3.50 mmol/h/gcat when the C_2H_4 ratio decreased from 1 to 0.33. However, there was a considerable drop to 1.93 mmol/h/gcat in the formation rate of C_3H_7OH when the C_2H_4 ratio decreased to 0.2. But the formation rate of C_2H_5CHO kept decreasing as the C_2H_4 ratio decreased. Therefore, a relatively high ratio of C_2H_4 can benefit the formation of C_2H_5CHO. Figure 6.2 (d) shows that the selectivity of C_2H_4 hydrogenation remained steady with a decrease in the C_2H_4 ratio of the feed-gas. The selectivity to C_3H_7OH increased as the C_2H_4 ratio decreased. The selectivity to C_2H_5CHO declined with a decrease in the C_2H_4 ratio in the feed-gas. It can be deduced that a decrease in C_2H_4 partial pressure did not inhibit EH, but did increase the formation rate and selectivity of C_3H_7OH. However, a low partial pressure of C_2H_4 led to a low formation rate and selectivity of C_2H_5CHO.

Figure 6.2 (f) shows the trend in CO selectivity to C_3 oxygenates. The selectivity of C_3H_7OH to converted CO first increased until the C_2H_4 ratio decreased from 1 to 0.5, then it dropped when the C_2H_4 ratio decreased from 0.5 to 0.2. With a decrease in the C_2H_4 ratio in the feed-gas, there was a declining trend in the selectivity of C_2H_5CHO to converted CO. The trend for total C_3 oxygenates was the same as the selectivity to C_3H_7OH.

Overall, changing the ethylene partial pressure can allow for the selectivity for propanol and propionaldehyde to be adjusted. High pressure ethylene can obtain more propionaldehyde, while reducing the ethylene partial pressure makes it easier to obtain propanol.

6.3.3 Effect of CO partial pressure

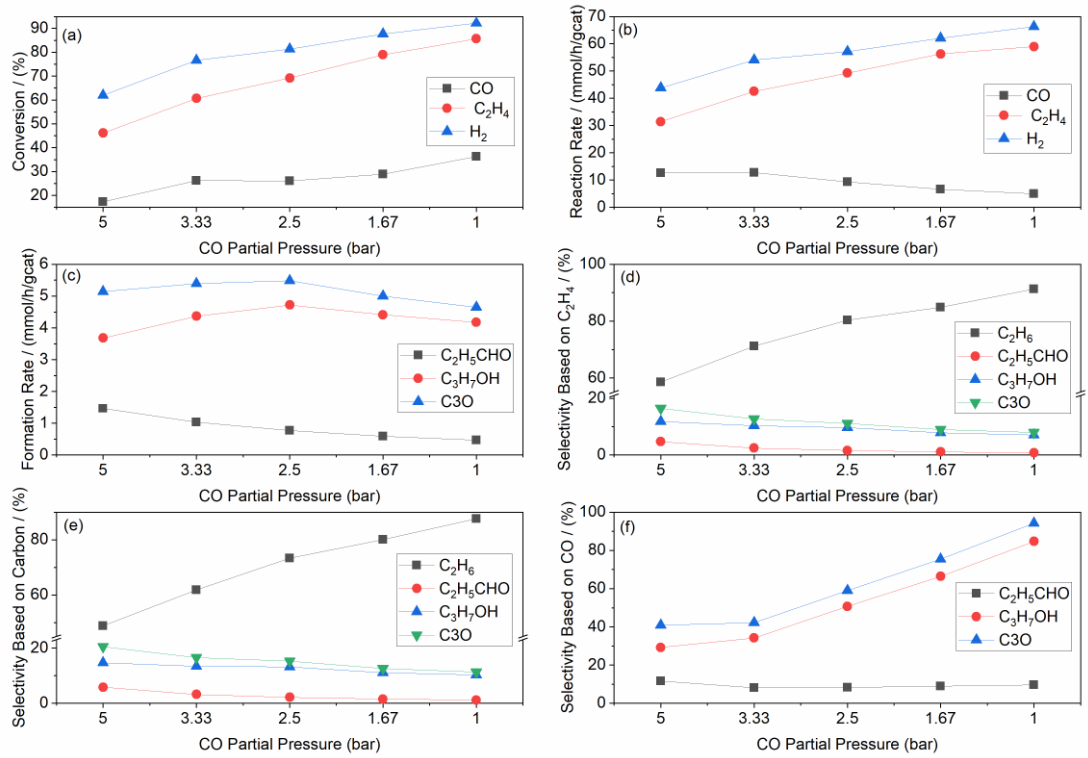

Figure 6.3 Catalytic activity and selectivity as a function of C_2H_4 partial pressure for EH. Reaction conditions: P = 20 bar, T = 250 ℃, GHSV = 1200 h^{-1} with a feed-gas mixture of CO/C_2H_4/H_2/N_2/Ar. (The partial pressure of H_2 and C_2H_4 are mentioned at a constant pressure of 5 bar each.)

Figure 6.3 shows the effect of CO partial pressure on the performance of EH when using a 0.5%Rh-20%Co/RGO catalyst. The reaction conditions are listed in Group C in Table 6.1. Figure 6.3 (a) shows that the conversion of all the reactants increased with a decrease in the CO ratio in the feed-gas. Figure 6.3 (b) shows that a decrease in the CO ratio in the feed-gas led to the reaction rate of H_2 and C_2H_4 increasing, while the conversion of CO decreased. Figure 6.3 (c) shows that the formation rate of C_3H_7OH increased slightly and then decreased with a decrease in the ratio of CO in the feed. The formation rate of C_2H_5CHO declined with a decrease in the CO ratio in the feed-gas. Because the formation rate of C_3H_7OH was much higher than that of C_2H_5CHO, the trend for the total C_3 oxygenates was the same as the trend for C_3H_7OH. Figure 6.3 (d) shows that the selectivity of converted C_2H_4 to C_2H_6 increased dramatically - from 58.58% to 91.27% - with a decrease in the CO ratio of the feed-gas. In contrast, the selectivity of converted C_2H_4 to C_3 oxygenates decreased from 16.39% to 7.88%. Therefore, a high CO partial pressure has a strong effect on inhibiting EH. A low CO partial pressure can increase the selectivity of C_3 oxygenates to the converted CO up to 94.28%, as shown in Figure 6.3 (f). Considering the selectivity based on the converted carbon shown in Figure 6.3 (e), a high CO partial pressure is preferred for EH.

To summarize: a higher partial pressure of CO could significantly inhibit the reaction of C_2H_4 hydrogenation and enhance the reaction of hydroformylation. In order to obtain a high selectivity to C_3 oxygenates and low selectivity to C_2H_6, a high CO partial pressure in the feed-gas is preferred.

6.3.4 Optimal reaction conditions for hydroformylation.

Table 6.2 Results of EH under optimal feed-gas ratios. P = 20 bar, T = 250 ℃, GHSV = 1200 h^{-1}

$CO:C_2H_4:H_2$	Formation Rate (mmol/h/gcat)			Reaction Rate (mmol/h/gcat)			Conversion (%)			Selectivity based on Converted C_2H_4(%)				Selectivity based on Converted C(%)				Selectivity based on Converted CO(%)		
	C_2H_5CHO	C_3H_7OH	C_3O	CO	C_2H_4	H_2	CO	C_2H_4	H_2	C_2H_6	C_2H_5CHO	C_3H_7OH	C_3O	C_2H_6	C_2H_5CHO	C_3H_7OH	C_3O	C_2H_5CHO	C_3H_7OH	C_3O
1:1:1	1.61	4.23	5.85	8.06	29.22	36.98	11.42	42.21	52.66	70.78	5.52	14.50	20.02	62.20	7.28	19.11	26.40	20.05	52.69	72.74
2:1:1	2.16	4.59	6.75	7.80	15.11	20.01	6.88	27.58	35.78	52.41	14.41	30.73	45.14	41.62	17.16	36.61	53.77	27.86	59.44	87.30
4:2:1	2.15	3.40	5.55	7.55	9.73	10.34	6.60	17.53	37.13	45.76	21.83	33.91	55.74	33.12	23.94	37.76	61.70	28.55	45.13	73.67

The highest selectivity may not be obtained by feeding the reaction gas according to the stoichiometric ratio. From 3.1 to 3.3, a higher CO partial pressure can increase C_3 oxygenates selectivity and when CO/C_2H_4 ratio at 2:1 is more appropriate. Based the conclusion from the partial pressure effects on the EH performance, two optimized feed-gas ratios were tested and evaluated. Table 6.2 provides a summary of the results of EH under the optimized feed-gas ratio. The results of EH under stoichiometric ratios are also provided for comparison purposes. When the CO partial pressure increased from 1 to 2 ($CO:C_2H_4:H_2$ = 2:1:1), the selectivity of converted C_2H_4 to C_3 oxygenates increased from 20.02% to 45.14%, while the selectivity of total converted carbon to C_3 oxygenates increased from 26.40% to 53.77%. Furthermore, the partial pressure of CO and C_2H_4 retained and a lower H_2 partial pressure was tested ($CO:C_2H_4:H_2$ = 4:2:1). The selectivity of C_3 oxygenates to converted C_2H_4 then increased to 55.74%, and the selectivity of C_3 oxygenates to converted carbon increased to 61.70%.

6.4 Conclusion

0.5%Rh-20%Co/rGO performs well in terms of EH. The partial pressure of H_2 and CO have more influence than C_2H_4 on the selectivity to oxygenates, while a lower H_2 ratio and a higher CO ratio in feed-gas can lead to high selectivity to oxygenates. The highest selectivity to oxygenates (61.70%) was obtained at a feed-gas ratio of $CO:C_2H_4:H_2$ = 4:2:1.

References

[1] R. Franke, D. Selent, A. Borner, Applied hydroformylation, Chem. Rev. 112 (2012) 5675–5732. https://doi.org/10.1021/cr3001803.

[2] H.-W. Bohnen, B. Cornils, Hydroformylation of alkenes: An industrial view of the status and importance, Adv. Catal. 17 (2002) 1–64. https://doi.org/10.1016/S0360-0564(02)47005-8.

[3] C. Li, W. Wang, L. Yan, Y. Ding, A mini review on strategies for heterogenization of rhodium-based hydroformylation catalysts (2017). https://doi.org/https://doi.org/10.1007/s11705-017-1672-9.

[4] K. Wiese, D. Obst, Hydroformylation, Catal. Carbonylation React. 18 (2006) 1–33. https://doi.org/10.1007/3418_015.

[5] Â.C.B. Neves, M.J.F. Calvete, T.M.V.D. Pinho E Melo, M.M. Pereira, Immobilized catalysts for hydroformylation reactions: A versatile tool for aldehyde synthesis, European J. Org. Chem. (2012) 6309–6320. https://doi.org/10.1002/ejoc.201200709.

[6] V.A. Likholobov, B.L. Moroz, Hydroformylation on solid catalysts, Handb. Heterog. Catal. (2008). https://doi.org/10.1002/9783527610044.hetcat0189.

[7] V.I. Zapirtan, B.L. Mojet, J.G. van Ommen, J. Spitzer, L. Lefferts, Gas phase hydroformylation of ethylene using organometalic Rh-complexes as heterogeneous catalysts, Catal. Letters. 101 (2005) 43–47. https://doi.org/10.1007/s10562-004-3747-8.

[8] L. Yan, Y.J. Ding, H.J. Zhu, J.M. Xiong, T. Wang, Z.D. Pan, L.W. Lin, Ligand modified real heterogeneous catalysts for fixed-bed hydroformylation of propylene, J. Mol. Catal. A Chem. 234 (2005) 1–7. https://doi.org/10.1016/j.molcata.2005.01.047.

[9] S.C.C.H.U.A.N.G. Steven, S. Pien, Enhancement of ethylene hydroformylation over Ni/SiO 2

through sulfur promotion, Catal. Letters. 6 (1990) 389–394.

[10] M. Jiang, L. Yan, Y. Ding, Q. Sun, J. Liu, H. Zhu, R. Lin, F. Xiao, Z. Jiang, J. Liu, Ultrastable 3V-PPh3 polymers supported single Rh sites for fixed-bed hydroformylation of olefins, J. Mol. Catal. A Chem. 404–405 (2015) 211–217. https://doi.org/10.1016/j.molcata.2015.05.008.

[11] L. Huang, Y. Xu, W. Guo, A. Liu, D. Li, X. Guo, Study on catalysis by carbonyl cluster-derived SiO2-supported rhodium for ethylene hydroformylation, Catal. Letters. 32 (1995) 61–81. https://doi.org/10.1007/BF00806102.

[12] T.A. Kainulainen, M.K. Niemelä, A.O.I. Krause, Rh/C catalysts in ethene hydroformylation: The effect of different supports and pretreatments, J. Mol. Catal. A Chem. 140 (1999) 173–184. https://doi.org/10.1016/S1381-1169(98)00223-4.

[13] X. Song, Y. Ding, W. Chen, W. Dong, Y. Pei, J. Zang, L. Yan, Y. Lu, Formation of 3-pentanone via ethylene hydroformylation over Co/activated carbon catalyst, Appl. Catal. A Gen. 452 (2013) 155–162. https://doi.org/10.1016/j.apcata.2012.11.006.

[14] T.A. Zeelie, A. Root, A.O.I. Krause, Rh/fibre catalyst for ethene hydroformylation: Catalytic activity and characterisation, Appl. Catal. A Gen. 285 (2005) 96–109. https://doi.org/10.1016/j.apcata.2005.02.010.

[15] K. Tomishige, I. Furikado, T. Yamagishi, S.I. Ito, K. Kunimori, Promoting effect of Mo on alcohol formation in hydroformylation of propylene and ethylene on Mo-Rh/SiO2, Catal. Letters. 103 (2005) 15–21. https://doi.org/10.1007/s10562-005-6497-3.

[16] T.A. Kainulainen, M.K. Niemelä, A.O.I. Krause, Ethene hydroformylation on Co/SiO2 catalysts, Catal. Letters. 53 (1998) 97–101. https://doi.org/10.1023/a:1019053805618.

[17] G.G. Stanley, Hydroformylation (OXO) catalysis, Kirk-Othmer Encycl. Chem. Technol. 1 (2017) 1–19. https://doi.org/10.1002/0471238961.1524150209121.a01.pub2.

[18] N. Navidi, J.W. Thybaut, G.B. Marin, Experimental investigation of ethylene hydroformylation to propanal on Rh and Co based catalysts, Appl. Catal. A Gen. 469 (2014) 357–366.

https://doi.org/10.1016/j.apcata.2013.10.019.

[19] R. Gao, C.D. Tan, R.T.K. Baker, Ethylene hydroformylation on graphite nanofiber supported rhodium catalysts, Catal. Today. 65 (2001) 19–29. https://doi.org/10.1016/S0920-5861(00)00541-1.

[20] L.A. Rupflin, J. Mormul, M. Lejkowski, S. Titlbach, R. Papp, R. Gläser, M. Dimitrakopoulou, X. Huang, A. Trunschke, M.G. Willinger, R. Schloegl, F. Rosowski, S.A. Schunk, Platinum group metal phosphides as heterogeneous catalysts for the gas-phase hydroformylation of small olefins, (2017). https://doi.org/10.1021/acscatal.7b00499.

Chapter 7: Influence of the reaction conditions on the performance of ethene hydroformylation using a Rh-Co bimetallic catalyst supported on reduced graphene oxide

Abstract

The influence of pressure, space velocity and temperature on ethene hydroformylation (EH) over a Rh-Co bimetallic catalyst supported by reduced graphene oxide (RGO) was investigated in a tubular fixed bed reactor (TFBR). All the reactions were carried out at the stoichiometrical reactant ratio of CO : C_2H_4 : H_2 = 1 : 1 : 1. The operating conditions - such as pressure, space velocity and temperature – have a significant effect on the performance of EH when using a 0.5%Rh-20%Co/RGO catalyst. High total pressure can limit the ethene hydrogenation side reaction and promote the formation of C_3 oxygenates. The highest selectivity of CO to C_3 oxygenates was obtained at 1 MPa, namely 83.24%. A different GHSV has a minor effect on the EH side reaction, but a significant promoting effect on the formation of C_3 oxygenates. GHSV = 960 h^{-1} is the optimized space velocity for EH when using a 0.5%Rh-20%Co/RGO catalyst. The temperature has a significant effect on EH performance in terms of conversion, reaction rate and selectivity. Different selectivity rates to C_2H_5CHO and C_3H_7OH can be tuned by changing the reaction temperature. A low temperature can inhibit hydrogenation of ethene to ethane. 210 °C to 230 °C is the optimized temperature range for EH when using a 0.5%Rh-20%Co/RGO catalyst. Through the calculation of apparent activation, conclusions can be drawn, i.e.: H_2 is the most difficult reactant to activate and CO is the easiest to activate; activating C_2H_4 is a little more difficult than activating CO, which is easier than activating H_2; the apparent order of activation for products is $E_{a\ C3H7OH}$ > $E_{a\ C2H6}$ > $E_{a\ C2H5CHO}$; EH displayed a lower apparent activation energy than ethene hydrogenation.

7.1 Introduction

Hydroformylation is one of the most important homogeneous industrial processes used to produce value-added aldehydes and much efforts has been devoted to the heterogenization of this process to

overcome the disadvantages of the homogeneous process, e.g. catalyst recovery, product separation and high pressure.[1,2,3]

In the previous chapter, cobalt supported on RGO was shown to be highly active for heterogeneous EH. The major side reaction in EH is hydrogenation.[4] In order to achieve high selectivity to oxygenates, the influence of the feed-gas ratio on EH over a Rh-Co bimetallic catalyst supported by RGO was investigated using a TFBR. This was reported on in the previous chapter. As heterogeneous EH is a gas phase reaction, the pressure, space velocity and temperature could have an effect on catalysis performance. Therefore, the influence of pressure, space velocity and temperature was investigated to optimise the process parameters in pursuit of achieving high selectivity to the target product and lowering the operating cost. This is reported on in this chapter.

7.2 Experimental Method

7.2.1 Catalyst preparation

The preparation of graphene oxide (GO) and 0.5%Rh-20%Co/rGO was done using the same procedure as that detailed in Chapter 4.

7.2.2 Catalytic performance

The performance of the catalysts was evaluated using a fixed-bed reactor with an internal diameter of 8 mm and a length of 380 mm. 0.5 g of a 0.5%-20%Co/RGO catalyst was loaded into the reactor and reduced with H_2 (AFROX - 99.999%) at 330 °C, 1 bar, 30 ml/min for 20 h. N_2 was used as the internal standard for mass balance calculations. All the gas flow rates were controlled using a Brooks 5850 instrument. All the feed-gas, calibration gas and products were analyzed using an online Agilent 7890B GC. The oxygenates and hydrocarbons were separated by a CP-Sil 5CB (25m x 0.15mm x 2.0 µm) column and analyzed using a flame ionization detector (FID). The other gases were analyzed using a thermal conductivity detector (TCD).

Table 7.1 Reaction conditions

Group	Run	$CO:C_2H_4:H_2$	T (℃)	Total P (bar)	Flow rate (ml(NTP/mi)
A	1	1:1:1	250	0	60
	2	1:1:1	250	5	60
	3	1:1:1	250	10	60
	4	1:1:1	250	15	60
	5	1:1:1	250	20	60
B	6	1:1:1	250	20	60
	7	1:1:1	250	20	48
	8	1:1:1	250	20	36
	9	1:1:1	250	20	24
C	10	1:1:1	140	20	60
	11	1:1:1	160	20	60
	12	1:1:1	170	20	60
	13	1:1:1	180	20	60
	14	1:1:1	190	20	60
	15	1:1:1	200	20	60
	16	1:1:1	210	20	60
	17	1:1:1	220	20	60
	18	1:1:1	230	20	60
	19	1:1:1	240	20	60
	20	1:1:1	250	20	60
	21	1:1:1	270	20	60
	22	1:1:1	290	20	60

7.2.3 Calculations

The calculations used are those provided in Chapter 6.

7.3 Results and Discussion

7.3.1 Effect of pressure

Figure 7.1 shows the influence of total pressure on EH performance using 0.5%Rh-20%Co/rGO as the catalyst under the following conditions: T = 250 °C, GHSV = 1200 h^{-1}, N_2:CO:C_2H_4:H_2 = 1:1:1:1. It displayed an increasing trend with an increase in total pressure – in both the conversion rate and the reaction rate for all reactants, including CO, C_2H_4 and H_2. (See Figure 7.1 (a) and (b).)

Figure 7.1 (c) shows that: the formation rate of C_3H_7OH increased nearly four times (from 0.64 mmol/h/gcat to 3.17 mmol/h/gcat) with a total pressure increase from 0 to 1 MPa; the formation rate of C_2H_5CHO more than doubled - from 0.18 mmol/h/gcat to 0.54 mmol/h/gcat - with a total pressure increase from 0 to 1 MPa (increase from ambient pressure to 1 MPa). With the increase in total pressure from 1 to 2 MPa, the change in the formation rate of the C_2H_5CHO, C_3H_7OH and C_3 oxygenates was very small, which indicate that the formation of C3 oxygenates is not sensitive to the total pressure when the it above 1 MPa.

The selectivity of ethene hydrogenation to ethane decreased from 83.72% to 67.06% with an increase in total pressure from 0 to 2 MPa (increase from ambient pressure to 1 MPa). (See Figure 7.1 (d).) The highest selectivity for C_3 oxygenates was obtained at 1 MPa. The same result was shown in the selectivity calculated based on total converted carbon, as per Figure 7.1 (e). Therefore, total pressure can influence the ethene hydrogenation side reaction and change the formation of C_3 oxygenates. The highest selectivity of CO to C_3 oxygenates was obtained at 1 MPa, namely 83.24%. When combining the results based on the formation rate and selectivity of C_3 oxygenates, 1 MPa could be the optimal total pressure for EH when using a 0.5%Rh-20%Co/RGO catalyst at 250 °C, GHSV = 1200 h^{-1}, N_2:CO:C_2H_4:H_2 = 1:1:1:1.

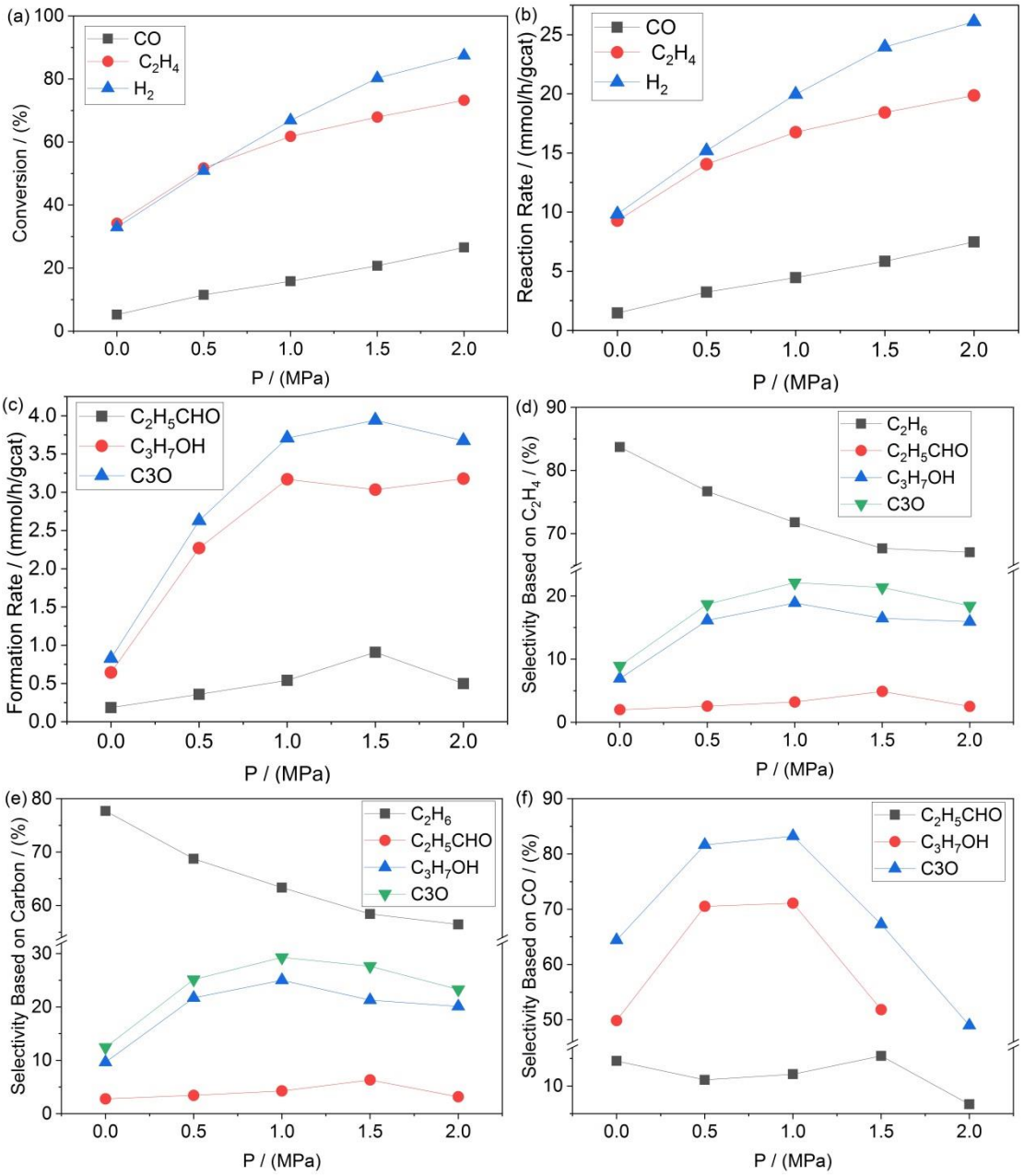

Figure 7.1 Reaction results of EH at different pressure. T = 250 °C, GHSV = 1200 h^{-1}, N_2:CO:C_2H_4:H_2 = 1:1:1:1.

7.3.2 Effect of space velocity

Figure 7.2 shows the effect of space velocity on the performance of EH using a 0.5%Rh-20%Co/RGO catalyst. Figure 7.2 (a) shows that the conversion of all the reactants decreased as the GHSV increased. However, the reaction rate of all the reactants increased with an increase in the GHSV, except for the CO reaction rate at GHSV = 1200 h^{-1}, which dropped compared with the data for GHSV = 960 h^{-1}. At GHSV = 960 h^{-1}, the CO reaction rate reached the highest point. Figure 7.2 (c) shows an increase in the formation rate of C_2H_5CHO as the GHSV increases. There was no regular trend in the

formation rate of C_3H_7OH, and the highest formation rate of C_3H_7OH was obtained at GHSV = 960 h^{-1}.

The selectivity of ethane, based on ethene consumption, decreased slightly from 67.06% to 62.60% with an increase in GHSV. (See Figure 7.2 (d).) The selectivity of C_2H_5CHO showed an increasing trend with an increase in GHSV. However, there was a fluctuating trend in the selectivity of C_3H_7OH and C_3O. The highest selectivity for C_3 oxygenates was obtained at GHSV = 960 h^{-1}. Figure 7.2 (e) shows that the selectivity calculated based on total converted carbon was presented: the selectivity of ethene to ethane did not change much; the selectivity of the C_3H_7OH fluctuated and achieved the highest value at GHSV = 960 h^{-1}, while the selectivity of C_2H_5CHO increased with an increase in GHSV. In Figure 7.2 (f), it can be seen that the selectivity of CO to C_3 oxygenates increased from 48.98% to 75.19% as the GHSV increased from 480 to 1200, except for the point at GHSV = 720 h^{-1}.

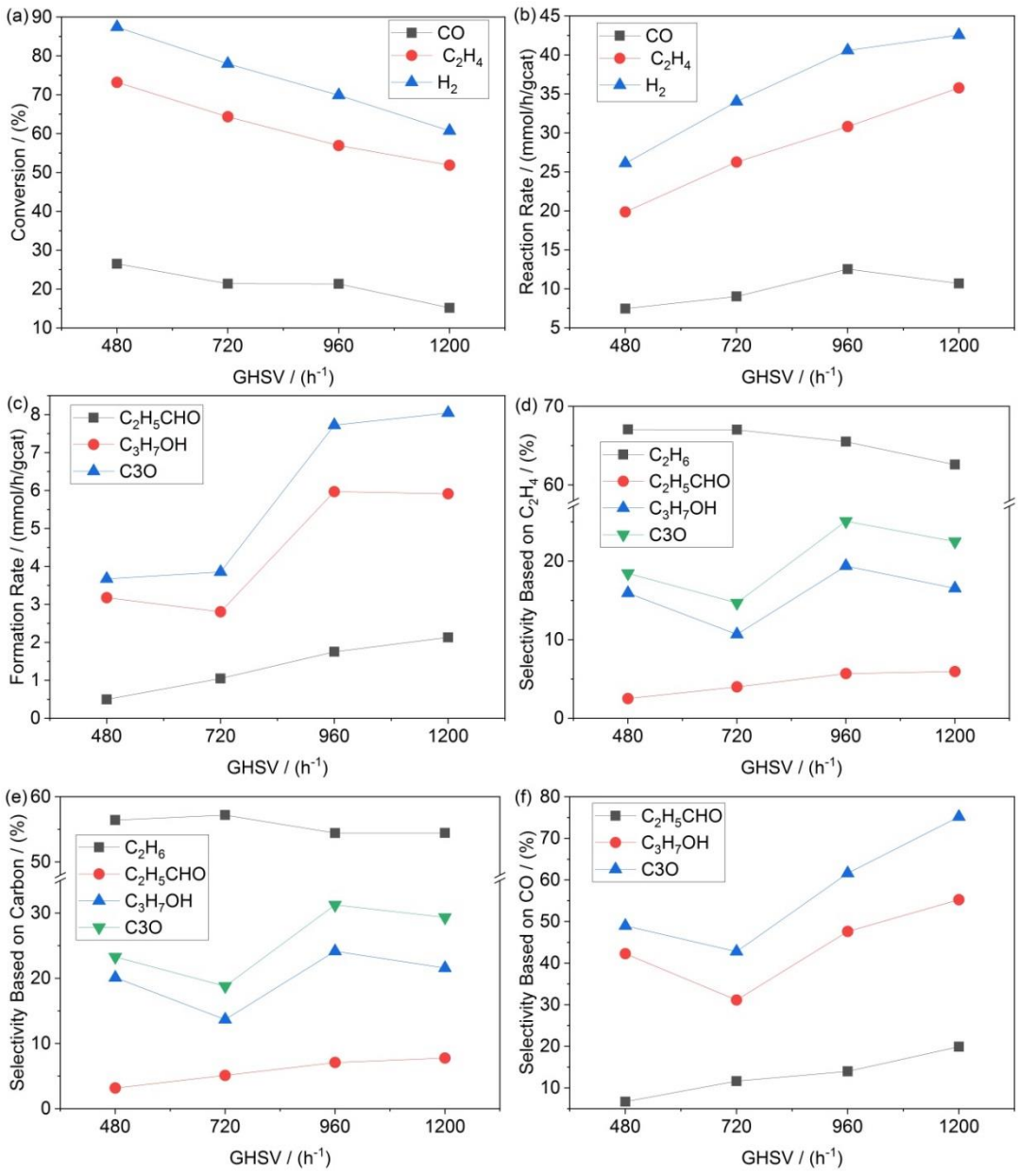

Figure 7.2 Reaction results of EH at different GHSV points. T = 250 °C, P = 2 MPa, N_2:CO:C_2H_4:H_2 = 1:1:1:1.

In summary, different GHSVs have a minor effect on the ethene hydrogenation side reaction, but a significant promoting effect on the formation of C_3 oxygenates. When combining the results based on the formation rate and selectivity of C_3 oxygenates, a higher flow rate is preferred for EH when using a 0.5%Rh-20%Co/RGO catalyst, especially for the formation of C_2H_5CHO.

7.3.3 Effect of temperature

Figure 7.3 shows the effect of temperature on the performance of EH when using an 0.5%Rh-20%Co/RGO catalyst. The reactions were carried out at temperatures of 140 °C to 290 °C. Figure 7.3

(a-b) shows that the conversion rate and reaction rate of each reactant was very low when the reaction temperature was below 210 °C.

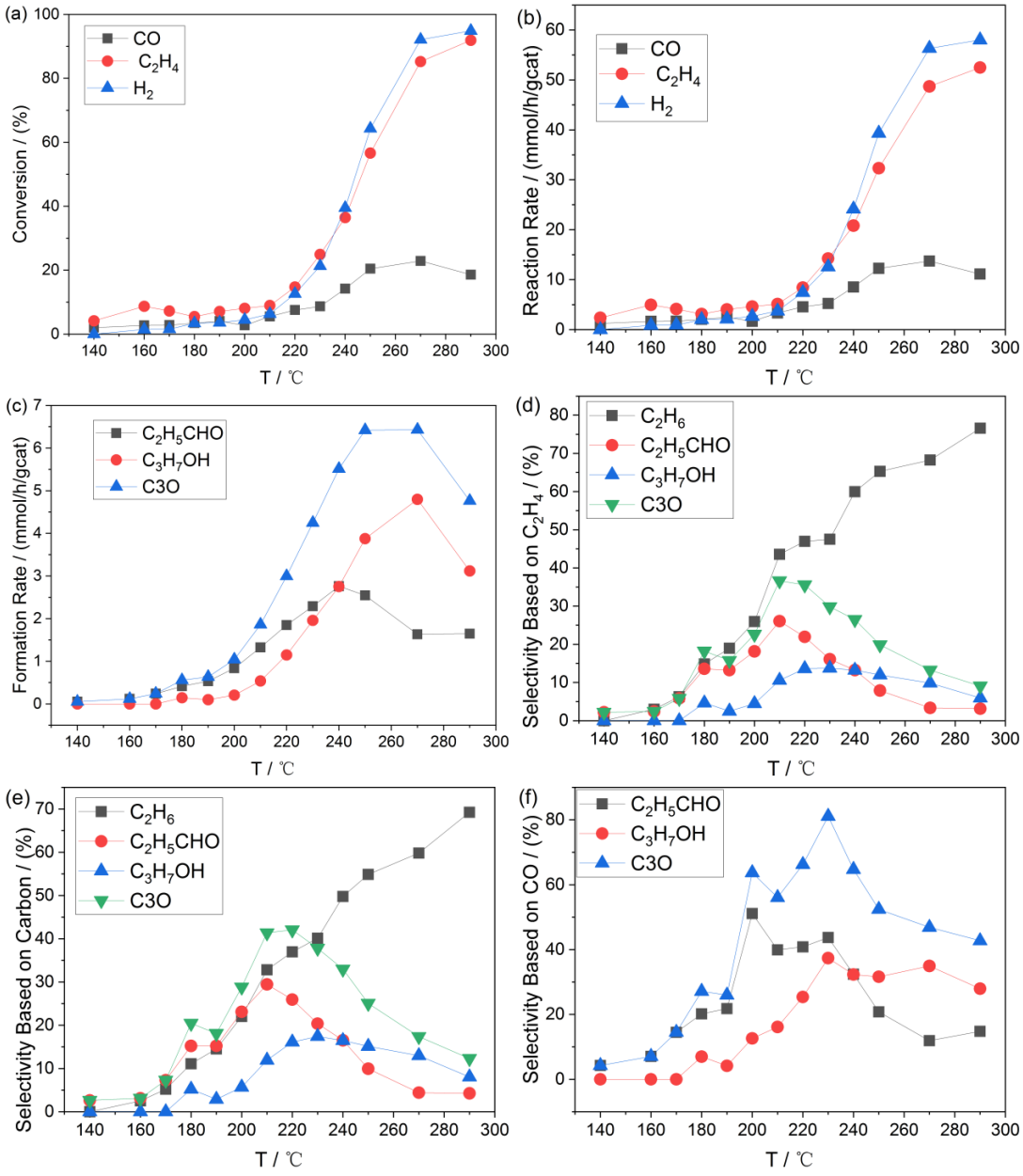

Figure 7.3 Reaction results of EH at different temperature levels. GHSV = 1200 h^{-1}, P = 2 MPa, N_2:CO:C_2H_4:H_2 = 1:1:1:1.

When the temperature increased from 220 °C to 270 °C: the conversion of C_2H_4, H_2 and CO increased dramatically, i.e. up to 85.25%, 92.10% and 22.90%, respectively; and the reaction rate of C_2H_4, H_2 and CO also increased significantly. The results indicate that EH reactivity increased explosively in the temperature range 220 °C to 270 °C. But with a further increase in temperature to 290 °C, the conversion rate and reaction rate of C_2H_4 and H_2 increased slightly, while the conversion and reaction

rate of CO decreased slightly. Figure 7.3 (c) shows that the formation rate of C_2H_5CHO increased to the highest rate at 240 °C and then decreased with an increase in temperature. A similar trend was observed with formation rates between C_2H_5CHO and C_3H_7OH. The only difference was that the highest formation rate was seen with C_3H_7OH is at 270 °C.

Below 240 °C, the formation rate of C_2H_5CHO was higher than that of C_3H_7OH. When the temperature was higher than 240 °C, the formation rate of C_2H_5CHO was lower. The formation rates of C_2H_5CHO and C_3H_7OH were almost the same at 240 °C. This data provided a strategy to tune the selectivity to C_2H_5CHO or C_3H_7OH by changing the reaction temperature. The highest formation rate for C_3 oxygenates was achieved at temperatures of 250 °C to 270 °C. Figure 7.3 (d) shows that the highest selectivity of C_2H_4 to C_3 oxygenates was achieved at 210 °C. When increasing the temperature from 230 to 290 °C, the selectivity of C_2H_4 to C_2H_6 increased dramatically. The selectivity was calculated based on total converted carbon - see Figure 7.3 (e) - and the selectivity of the C_3 oxygenates was higher than that for ethane when the temperature was below 240 °C. () The selectivity was calculated based on CO consumption - Figure 7.3 (f) - and the highest selectivity of CO to C_3 oxygenates was achieved at 230 °C.

Therefore, temperature has a significant effect on the activity and selectivity of EH. The selectivity of EH products can be tuned by changing the reaction temperature: a lower temperature is required for the formation of C_2H_5CHO, while a higher temperature is required for the production of C_3H_7OH. A low temperature can inhibit hydrogenation of ethene to ethane.

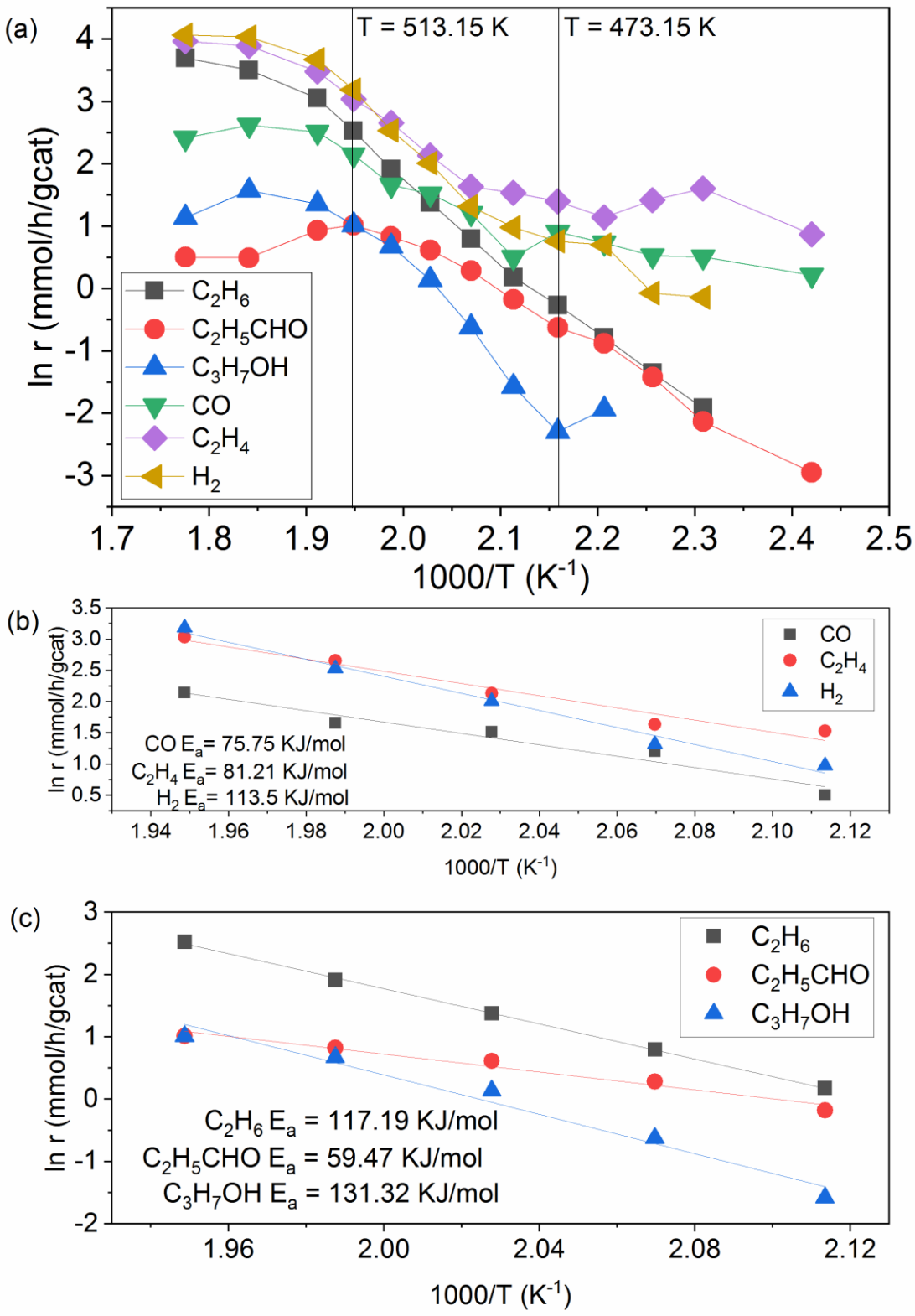

Figure 7.4 (a) Plots (ln r (mmol/h/gcat)) versus (1000/T) from 413.15 K to 563.15 K. (b) Arrhenius plots of reactants from 473.15 K to 513.15 K. (c) Arrhenius plots of products from 473.15 K to 513.15 K.

The Arrhenius equation can be used to describe the governing thermal relations in the different equations over time and temperature domains for non-isothermal kinetics.[5] The activation energy can be calculated using experimental data.[6] The plots for (ln r (mmol/h/gcat)) versus (1000/T) for

C_2H_6, C_2H_5CHO, C_3H_7OH and the reactants are shown in Figure 7.4 (a). It shows that (ln r (mmol/h/gcat)) versus (1000/T) exhibited a linear correlation from 473.15 K to 513.15 K in all the plots. (See Figure 7.4 (a).) Therefore, the Arrhenius plots were fitted for C_2H_6, C_2H_5CHO, C_3H_7OH (Figure 4 (c)) and the reactants (Figure 7.4 (c)). The apparent activation energy of each component was calculated, as shown in Figure 7.4 (b) and (c). The apparent activation of energy of CO, C_2H_4 and H_2 was 75.75 KJ/mol, 81.21 KJ/mol and 113.50 KJ/mol, respectively. (See Figure 7.4 (b).)

It can be concluded that, on the surface of the catalyst, H_2 is the most difficult reactant to activate and CO is the easiest to activate. Activation of C_2H_4 is a little more difficult than activation of CO, which is in turn easier than activation of H_2. The order of apparent activation energy for reactants explains the order of apparent activation for products: $E_{a\ C3H7OH}$ (131.32 KJ/mol) > $E_{a\ C2H6}$ (117.19 KJ/mol) > $E_{a\ C2H5CHO}$ (59.47 KJ/mol). (See Figure 7.4 (c).) The formation of C_3H_7OH was the most difficult because it needs to activate one CO molecule, one C_2H_4 molecule and two H_2 molecules. Although the formation of C_2H_6 is the simplest, the apparent activation energy of C_2H_6 was still much higher than that of C_2H_5CHO, probably because of the high activation energy of H_2. The apparent activation energy of C_2H_5CHO was the lowest due to the low activation energy of CO and C_2H_4. This is also a possible explanation for the high selectivity of C_2H_6 and C_3H_7OH at a high temperature, because the formation of C_2H_6 and C_3H_7OH requires more energy.

It is can be concluded that EH has a lower apparent activation energy than ethene hydrogenation, which coincides with the conclusions in the literature.[7–10] Moreover, the apparent activation energy of EH on a 0.5%Rh-20%Co/RGO catalyst is lower than that of a SiO_2 supported rhodium catalyst (19.2 KCAL/mol ≈ 80.4 KJ/mol), as previously reported.[8]

7.4 Conclusion

Operating conditions such as pressure, space velocity and temperature have a significant effect on the performance of EH when using a 0.5%Rh-20%Co/RGO catalyst. High total pressure can limit the EH side reaction and promote the formation of C_3 oxygenates. The highest selectivity of CO to C_3 oxygenates was obtained at 1 MPa, namely 83.24%. Different GHSVs have a minor effect on the

ethene hydrogenation side reaction, but a significant promoting effect on the formation of C_3 oxygenates. GHSV = 960 h^{-1} is the optimized space velocity for EH when using a 0.5%Rh-20%Co/RGO catalyst. The temperature has a significant effect on EH performance in terms of the conversion, reaction rate and selectivity. Different selectivity rates to C_2H_5CHO and C_3H_7OH can be tuned by changing the reaction temperature. A low temperature can inhibit the hydrogenation of ethene to ethane. 210 °C to 230 °C is the optimized temperature range for the EH when using a 0.5%Rh-20%Co/RGO catalyst. By calculating the apparent activation, conclusions can be drawn, i.e.: H_2 is the most difficult reactant to activate and CO is the easiest to activate; the activation of C_2H_4 is a little more difficult than that of CO, which is also much easier than the activation of H_2; the order of apparent activation for products is $E_{a\ C3H7OH} > E_{a\ C2H6} > E_{a\ C2H5CHO}$; EH displayed a lower apparent activation energy than ethene hydrogenation.

References

[1] C. Li, W. Wang, L. Yan, Y. Ding, A mini review on strategies for heterogenization of rhodium-based hydroformylation catalysts, Front. Chem. Sci. Eng. (12)1(2017)113-123. https://doi.org/https://doi.org/10.1007/s11705-017-1672-9.

[2] X. Wang, Recent advances in continuous rhodium-catalyzed hydroformylation, J. Flow Chem. 5 (2015) 125–132. https://doi.org/10.1556/1846.2015.00003.

[3] A.C.B. Neves, M.J.F. Calvete, T.M.V.D. Pinho E Melo, M.M. Pereira, Immobilized catalysts for hydroformylation reactions: A versatile tool for aldehyde synthesis, European J. Org. Chem. (2012) 6309–6320. https://doi.org/10.1002/ejoc.201200709.

[4] G.G. Stanley, Hydroformylation (OXO) catalysis, Kirk-Othmer Encycl. Chem. Technol. 1 (2017) 1–19. https://doi.org/10.1002/0471238961.1524150209121.a01.pub2.

[5] A.E.T. Elgendy, A.H. Abdel-Aty, A.A. Youssef, M.A.A. Khder, K. Lotfy, S. Owyed, Exact solution of Arrhenius equation for non-isothermal kinetics at constant heating rate and n-th order of reaction, J. Math. Chem. 58 (2020) 922–938. https://doi.org/10.1007/s10910-019-01056-7.

[6] F. Jensen, Activation energies and the Arrhenius equation, Qual. Reliab. Eng. Int. 1 (1985) 13–17. https://doi.org/10.1002/qre.4680010104.

[7] M.A. Brundage, S.S.C. Chuang, Experimental and modeling study of hydrogenation using deuterium step transient response during ethylene hydroformylation, J. Catal. 164 (1996) 94–108. https://doi.org/10.1006/jcat.1996.0366.

[8] T. Hanaoka, H. Arakawa, T. Matsuzaki, Y. Sugi, K. Kanno, Y. Abe, Ethylene hydroformylation and carbon monoxide hydrogenation over modified and unmodified silica supported rhodium catalysts, Catal. Today. 58 (2000) 271–280. https://doi.org/10.1016/S0920-5861(00)00261-3.

[9] M. Lenarda, R. Ganzerla, L. Storaro, R. Zanoni, Catalysis by the Rh/B system Part 1. Vapour-

phase hydroformylation of ethylene at atmospheric pressure on Rh/B on silica, J. Mol. Catal. 78 (1993) 339–350. https://doi.org/10.1016/0304-5102(93)87063-E.

[10] N. Takahashi, M. Kobayashi, Comparison of ethylene with propylene hydroformylation over a Rh-Y zeolite catalyst under atmospheric pressure, J. Catal. 85 (1984) 89–97. https://doi.org/10.1016/0021-9517(84)90112-X.

Chapter 8: C-C formation and C-H formation on a CO non-dissociation catalyst with $CO/C_2H_4/H_2$ feed-gas: Mechanisms and reaction pathways for ethene hydroformylation and Fischer-Tropsch Synthesis

Abstract

Mechanistic studies on the reaction of $CO/C_2H_4/H_2$ on a CO non-dissociation catalyst are, to the best of our knowledge, scarce. In this work, a rhodium-promoted cobalt carbide supported by reduced graphene (0.5%Rh-20%Co/RGO), which suppressed CO direct dissociation, was used for the reactions of both C_2H_4 hydroformylation and Fischer-Tropsch synthesis (FTS). The reaction pathways to form oxygenates and hydrocarbons was confirmed by the formation sequence of products at different temperatures. Different types of interaction between CO and C_2H_4 determined the reaction directions in the $CO/C_2H_4/H_2$ system. C-C bond formation between CO and C_2H_4 was the easiest elementary step to achieve in this system – and even easier than C-H bond formation for C_2H_4 hydrogenation. At a low reaction temperature (140-190 °C), C_2H_4 induced the reaction of CO and C_2H_4 to form C-C coupling with an intermediate of $*C_2H_4CO$, which could then react with H_2 to form oxygenates and hydrocarbons. With an increase in temperature (210-290 °C), CO induced the formation of ethylidyne ($\equiv C\text{-}CH_3$), which triggered the chain growth reaction and produced more hydrocarbons.

8.1 Introduction

C-C bond formation is a key elementary step in the FTS reaction that produces long chain hydrocarbons.[1] C-H bond formation is another key elementary step for CO dissociation and to form intermediates for chain growth - as reported in various studies on FTS mechanisms [2–5] - and for the termination of chain growth.[1] C-C bond formation and C-H bond formation are also involved in ethene hydroformylation (EH), which was discovered olefins co-feeding to FTS. [6–8] It was considered as a secondary reaction of ethene during FTS.[5,9,10] The reaction of $CO/C_2H_4/H_2$ is still receiving much attention, in order to understand and elucidate the mechanisms of hydroformylation [11,12] and FTS[5,9,10,13–20].

A great deal of work on the reaction of $CO/C_2H_4/H_2$ during FTS over cobalt-based catalysts has been reported, in order to investigate the product distribution and reaction pathways. Co-feeding ethene to FTS leads to a decrease in methane selectivity,[21] an increase in selectivity of C_{5-6} products [21] and an increase in the O/P ratio of C_{3-6} hydrocarbons.[9] In terms of the mechanism aspect, through isotopic labelled experiments, it was found that C_1 species can be generated from ethene to form methane and long chain hydrocarbons.[9,14] Recently, surface reactions of chemisorbed ethene on Co(0001) with CO spectators were studied by Weststrate et al. through near-ambient pressure XPS, and an alkylidyne (R-C≡) intermediates mechanism was proposed for FTS chain growth.[1,22] However, all these findings were observed on metallic cobalt, on which CO can be dissociated directly or with the assistance of H. Although the alkylidyne intermediates mechanism provides a compelling explanation for FTS chain growth, there is still a lack of information on the mechanisms for propionaldehyde and alcohols.

This study involved a reversed experiment - similar to the discovery of EH from FTS - was designed to determine if FTS could be found when the EH reaction is carried out under heterogeneous FTS conditions. In this work, a CO non-dissociation cobalt catalyst was used for EH under FTS conditions at different temperatures, in order to study the mechanisms and reaction pathways for EH and FTS. Based on the detection sequence of different products, the reaction pathways were proposed. A different interaction between carbon monoxide and ethene beyond the alkylidyne chain growth

mechanism was observed, which can rationalize the mechanistic insight to the secondary reaction of ethene: EH.

8.2 Materials and Methods

The RCG catalyst used in this chapter is the same catalyst used in Chapter 4.

8.2.1 Preparation of GO

10 g of graphite was added to 230 mL of 95% H_2SO_4 and the mixture was stirred for 30 min in an ice-water bath. Then, 50 g of $KmnO_4$ was slowly added to the mixture over 2 hours and the mixture was stirred for 1 h. After the ice-water was removed, the mixture was settled at room temperature for about 16 h. The mixture was then put into ice obtained from an H_2O_2 aqueous solution (5ml 30% H_2O_2 in 100ml DI water). The colour of the mixture then changed to bright yellow. To remove the residual metal ions, the mixture was centrifuged and washed with DDI water until the pH value of the supernatant was neutral (pH 7), as a result of removing the remaining sulfuric acid. The concentration of obtained graphene oxide (GO) was 13.86 mg/ml.

8.2.2 Preparation of 0.5%Rh-20%Co/RGO (RCG)

346 ml GO solution (4.77g GO) was treated by ultrasound for 30 min. A 10ml solution of 5.06 g $Co(Ac)_2 \cdot 4H_2O$ and 0.08 g $RhCl_3 \cdot 3H_2O$ was then added to the GO solution. After the solution was treated by ultrasound for 30 min, the pH value of the mixture was adjusted to 10, and 2 ml hydrazine hydrate was then added. Thereafter, the solution was treated by ultrasound for 30min, and the solution was moved to Teflon-lined stainless-steel autoclave. The GO was reduced using a hydro-thermal method at 180 ℃ for 15 h. The obtained sample was dried at 80 ℃ and calcined at 400 ℃ for 5 h under an N_2 atmosphere.

8.2.3 Catalytic performance

The performance of the catalysts was evaluated using a fixed-bed reactor (FBR) with an internal diameter of 8 mm and a length of 380 mm. 0.5 g of a 0.5%Rh-20%Co/RGO catalyst was loaded into the reactor and reduced with H_2 (AFROX (African Oxygen) Ltd.- 99.999%) at 350 °C, 1 bar, 30ml/min for 20 h. EH experiments were then done using different temperatures (from 140 °C to 290 °C) under

the following conditions: 2 MPa; total flow rate = 60 ml/min; feed-gas molar ratio: N_2:CO:C_2H_4:H_2 = 1:1:1:1; GHSV = 1000 h^{-1}. The test for FTS was after EH reaction under the following conditions: 2 MPa; total flow rate = 60 ml/min; feed-gas molar ratio: N_2:CO:H_2 = 1:3:6; GHSV = 1000 h^{-1}. N_2 was used as the internal standard gas for the calculations. All the feed-gas, calibration gas and products were analyzed by means of an online Agilent 7890B GC. Oxygenates and hydrocarbons were separated by a CP-Sil 5CB (25 m x 0.15 mm x 2.0 μm) column and analyzed using a flame ionization detector (FID). The other gases were analyzed by two thermal conductivity detectors (TCDs). Finally, the used catalyst was unloaded for further characterization.

8.3 Results and Discussion

The reaction was carried out under a typical regime of heterogeneous EH over rhodium-promoted cobalt carbide supported by reduced graphene 0.5%Rh-20%Co/RGO (RCG). The prepared RCG catalyst was experimentally improved to ensure good selectivity for the production of oxygenates under FTS reaction conditions. Part of the research results are reported on in Chapter 4 and Chapter 5 of this thesis. Briefly, when feeding CO : C_2H_4 : H_2 into the reactor with the RCG catalyst, the main reaction is EH, which produces propionaldehyde This can be further hydrogenated to propanol. However, as the reaction was carried out in a heterogeneous system, some side reactions also occurred. The possible side reactions are:

- Ethene hydrogenation.
- CO hydrogenation and chain growth to long chain hydrocarbons (FTS).
- CO methanation.
- Ethene dimerization and olimerization.
- Dehydrogenation of formed alcohols to olefins.

Catalyst characterization was reported on in Chapter 5. Based on the powder X-ray diffraction (XRD) characterization, there was cobalt oxide (CoO) in the fresh catalyst and cobalt carbide (Co_2C) in the spent catalyst. More details are provided in Chapter 5.

The experiments done in this work were to investigate the products detected by an online (GC) when using different temperatures (between 140 °C and 290 °C). The other operating conditions were: 0.5g catalyst, 2 MPa, total flow rate = 60 ml/min, feed-gas molar ratio: N_2 : CO : C_2H_4 : H_2 = 1 : 1 : 1 : 1, GHSV = 1000 h^{-1}. With an increase in temperature, the reaction path of the whole system can be inferred from the elementary reaction steps of the new product at each temperature level.

8.3.1 Products detected by GC at different temperature levels and their possible formation routes

T (℃)	Products Distribution at Different Temperatures															
140	C_2H_5CHO	C_2H_6														
160	C_2H_5CHO	C_2H_6														
170	C_2H_5CHO	C_2H_6														
180	C_2H_5CHO	C_2H_6	C_3H_7OH													
190	C_2H_5CHO	C_2H_6	C_3H_7OH	C_3H_6												
200	C_2H_5CHO	C_2H_6	C_3H_7OH	C_3H_6												
210	C_2H_5CHO	C_2H_6	C_3H_7OH	C_3H_6	CH_4	iso-C_4H_{10}										
220	C_2H_5CHO	C_2H_6	C_3H_7OH	C_3H_6	CH_4	iso-C_4H_{10}	C_3H_8	n-C_4H_8	tran-2-C_4H_8	C6						
230	C_2H_5CHO	C_2H_6	C_3H_7OH	C_3H_6	CH_4	iso-C_4H_{10}	C_3H_8	n-C_4H_8	tran-2-C_4H_8	C6	C5					
240	C_2H_5CHO	C_2H_6	C_3H_7OH	C_3H_6	CH_4	iso-C_4H_{10}	C_3H_8	n-C_4H_8	tran-2-C_4H_8	C6	C5	CH_3OH	n-C_4H_{10}			
250	C_2H_5CHO	C_2H_6	C_3H_7OH	C_3H_6	CH_4	iso-C_4H_{10}	C_3H_8	n-C_4H_8	tran-2-C_4H_8	C6	C5	CH_3OH	n-C_4H_{10}	cis-2-C_4H_8	CO_2	C7+
270	C_2H_5CHO	C_2H_6	C_3H_7OH	C_3H_6	CH_4	iso-C_4H_{10}	C_3H_8	n-C_4H_8	tran-2-C_4H_8	C6	C5	CH_3OH	n-C_4H_{10}	cis-2-C_4H_8	CO_2	C7+
290	C_2H_5CHO	C_2H_6	C_3H_7OH	C_3H_6	CH_4	iso-C_4H_{10}	C_3H_8	n-C_4H_8	tran-2-C_4H_8	C6	C5	CH_3OH	n-C_4H_{10}	cis-2-C_4H_8	CO_2	C7+

Figure 8.1 Product distribution at different temperature levels. (Reaction conditions: 2 MPa, total flow rate = 60 ml/min, feed-gas molar ratio: N_2:CO:C_2H_4:H_2 = 1:1:1:1, GHSV = 1000 h^{-1}).

Figure 8.1 details the products detected by an online GC under different reaction temperatures. It is clear that the higher the reaction temperature, the more kinds of products are produced, which indicates that more reactions are involved at a higher temperature. This distribution was useful to describe the formation and desorption order for the products when the reaction temperature was increasing. At each temperature, the new product produced was labelled, for example, C_3H_7OH at 180 °C.

At 140 °C, C_2H_5CHO and C_2H_6 were the only products detected by GC. Scheme 8.1 provides two possible formation pathways for C_2H_5CHO. In Pathway 1, the coupling of $*C_2H_4$ and *CO to an intermediate $*C_2H_4CO$ is prior to further formation of C-H to C_2H_5CHO. In Pathway 2, the formation of C-H on $*C_2H_4$ to $*C_2H_5$ and the formation of C-H on *CO to formyl group *CHO occur prior to the coupling of the C-C bond between $*C_2H_4$ and *CO.

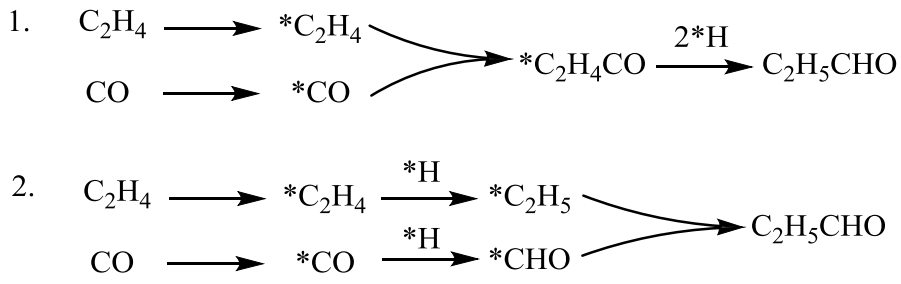

Scheme 8.1 Two possible formation pathways for C_2H_5CHO

At 140 °C, the formation of $*C_2H_5$ was confirmed by the production of C_2H_6. Whether or not Pathway 2 in Scheme 8.1 occurred depends on the formation of *CHO occurring. If *CHO is formed at 140 °C, CH_3OH or HCHO should be formed after further hydrogenation. The formation of the C-H bond between *CO and *H occurred by the formation of C_2H_5CHO at 140 °C; the formation of the C-H bond between *CHO and *H was indicated by the production of C_3H_7OH at 180 °C. (See Scheme 8.2.) However, no HCHO was detected at 140 °C to 230 °C, but the formation of *CHO was confirmed by the production of CH_3OH at 240 °C. (See Scheme 8.3.) Therefore, the formation pathway of C_2H_5CHO was confirmed as being Pathway 1 in Scheme 8.1: first the C-C bond coupling occurs between $*C_2H_4$ and *CO to form an intermediate $*C_2H_4CO$ and then $*C_2H_4CO$ is hydrogenated to C_2H_5CHO.

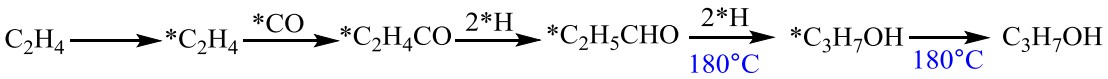

Scheme 8. 2 The formation pathway of C_3H_7OH

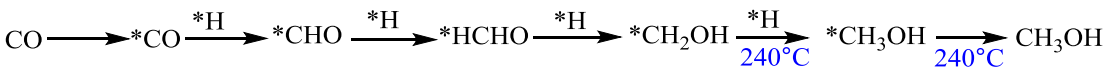

Scheme 8.3 The formation pathway of CH_3OH

As the formation of C_3H_7OH proposed that the C-H bond can form between *CHO and *H at 180 °C, if *CHO is formed at 180 °C then CH_3OH or HCHO should be detected at 180 °C. However, no CH_3OH formed below 240 °C. Therefore, it can be concluded that *CHO started to form at 240 °C. So Pathway 2 in Scheme 8.1 did not happen at 160 °C and probably competed with Pathway 1 in Scheme 8.1 and occurred starting at 240 °C.

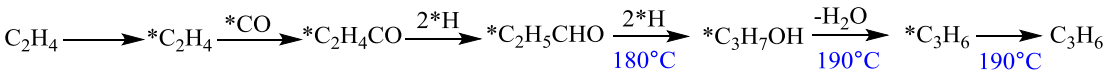

Scheme 8.4 The formation pathway of C_3H_6

CO on the surface of the catalyst can be deduced based on the conclusions detailed above. As there is no CH_4 or long chain hydrocarbons produced at 140 °C and 160 °C, *CO was neither directly dissociated nor H-assisted dissociated to form the monomer $*CH_x$ to initial the hydrocarbon chain growth but can be coupled with $*C_2H_4$ to form an intermediate $*C_2H_4CO$. It should also be questioned if CO can be chemisorbed (C≡O→*C=O) on the surface of the catalyst at 140 °C and 160 °C, because *CHO was not formed at 140 °C and 160 °C. Therefore, CO was probably physically adsorbed on the surface of the catalyst at 140 °C and 160 °C. Based on the confirmed formation pathway of C_2H_5CHO at 140 °C and 160 °C, the formation of the intermediate $*C_2H_4CO$ and the formyl group in C_2H_5CHO showed that CO can be chemisorbed to form the CHO group with the assistance of $*C_2H_4$. It can be deduced that $*C_2H_4$ induced the CO insertion mechanism on the surface of the catalyst and formed the intermediate $*C_2H_4CO$. With further hydrogenation of $*C_2H_4CO$, C_2H_5CHO (Pathway 1 in Scheme 8.1) and C_3H_7OH (Scheme 8.2) were formed. It is worth noting that only two hydrocarbon products were produced at 190 °C: C_2H_6 was obtained by C_2H_4 hydrogenation; C_3H_6. The formation of C_3H_6 was started at 190 °C and Scheme 8.4 presents its formation pathway. It is posited that C_3H_6 was produced by dehydration of C_3H_7OH at 190 °C.

The production of C_3H_6 (C_3 is an odd number olefin) indicates that CO was completely dissociated and hydrogenated from -C≡O to $=CH_2$ in hydrocarbon without any other long chain hydrocarbons or CH_4, except for C_2H_6 generated by hydrogenation of C_2H_4. Therefore, C_2H_4 induced C≡O dissociation, and hydrogenation to hydrocarbon presented at 190 °C. In fact, $*C_2H_4$ is an initiator that reacts with CO and H_2 to form C_3H_6.

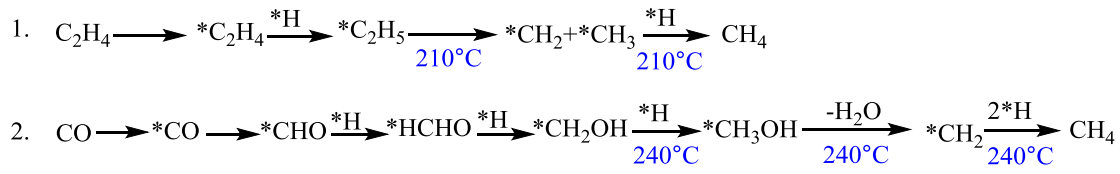

Scheme 8.5 Two possible formation pathways of CH_4 at 210 °C

CH_4 started to form at 210 °C. It is clear that the formation of $*CH_x$ is essential for the formation of CH_4 and $*CH_x$ must come from either C_2H_4 or CO. Scheme 8.5 shows two possible formation pathways for the production of CH_4. Pathway 1 is based on a C_2H_4 hydrocracking mechanism that forms $*CH_2$ and $*CH_3$, which was also reported by other researchers [23,9]. Pathway 2 is the H-assisted CO dissociation mechanism that forms $*CH_3$, which has been well studied in relation to FTS. However, the formation of CH_3OH started at 240 °C, which means it is very difficult to form $*CH_3$ at 210 °C. Therefore, at 210 °C, Pathway 2 may not activate. But at a temperature of 240 °C and higher, two pathways in Scheme 8.5 were possibly occurring at the same time and competing. As C_2H_5CHO, C_2H_6, C_3H_7OH, C_3H_6, CH_4 and iso-C_4H_{10} were the only products formed at 210 °C, FTS chain growth was not initiated by the formation of $*CH_2$ or $*CH_3$, which is generally thought to be the monomer for forming long chain hydrocarbons in FTS.

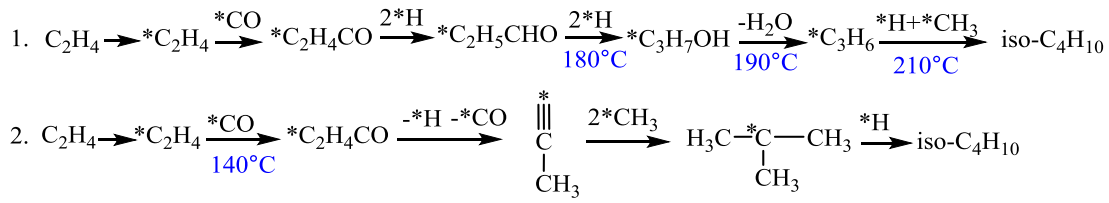

Scheme 8.6 Two possible formation pathways of iso-C_4H_{10}

iso-C_4H_{10} also started to form at 210 °C. Scheme 8.6 shows two possible formation pathways for iso-C_4H_{10}. In Pathway 1, the iso-C_4H_{10} was produced via an additional reaction of C_3H_6 with *H and $*CH_3$ that formed from C_2H_4 hydrocracking at a temperature of 210 °C. Pathway 2 is proposed based on the work reported recently by Weststrate.[1] It was reported that CO-induced formation of ethylidyne (≡C-CH_3) is a facile reaction that occurs on Co(0001), which increases the reactivity of ethylidyne dimerization to form 2-butyne (H_3C-C≡C-CH_3).[1] In the experiments done in this study, ethylidyne (≡C-CH_3) was probably produced from the intermediate $*C_2H_4CO$ eliminating *H and *CO and then participating in the formation of iso-C_4H_{10} via the additional reaction of triple bonds in ethylidyne with *H and $*CH_3$ (Pathway 2 in Scheme 8.6).

It is hard to ensure Pathway 1 in Scheme 6 because there is no more evidence to confirm the addition mechanism of C_3H_6 to form iso-C_4H_{10}. However, more proof of the ethylidyne mechanism (Pathway 2 in Scheme 8.6) was indicated by the formation of trans-2-butene, which was one of new products

detected at 220 °C. (See Figure 8.1.) The formation of ethylidyne (≡C-CH_3) explains the mechanism of ethene dimerization and the production trans-2-butene (H_3C-C=C-CH_3).[1] The formation pathway of trans-2-butene is shown in Scheme 8.7. As two adsorbed carbon atoms with triple bonds in ethylidyne (≡C-CH_3) combined to form 2-butyne (H_3C-C≡C-CH_3), methyls should be distributed at the same side of the triple bonds in 2-butyne (marked in red in Scheme 8.7). After further hydrogenation of the triple bonds, methyls were kept at the same side of the double bonds generated, while two hydrogen atoms were added on the other side of the double bonds to terminate the reaction and eliminate cis-2-butene. However, cis-2-butene is not stable at 220 °C and quickly isomerizes to trans-2-butene. Thus, trans-2-butene is produced through ethene dimerization. (The formation of cis-2-butene started at 250 °C, as it needs a higher temperature to retain the cis-2-butene due to the higher entropy of its structure.)

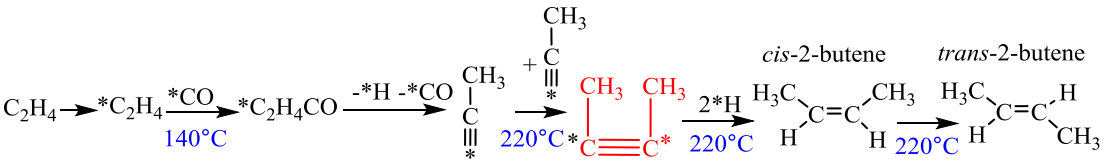

Scheme 8. 7 The formation pathway of trans-2-butene

As the formation of ethylidyne (≡C-CH_3) was confirmed by the formation of trans-2-ethene, another pathway of C_2H_4 hydrocracking was proposed, as shown in Scheme 8.8.

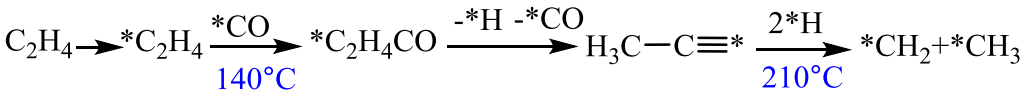

Scheme 8.8 Another pathway of C_2H_4 hydrocracking via ethylidyne intermediate

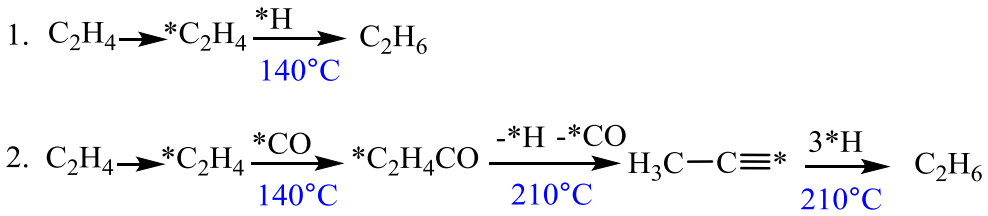

Scheme 8.9 Two possible formation pathways of C_2H_6

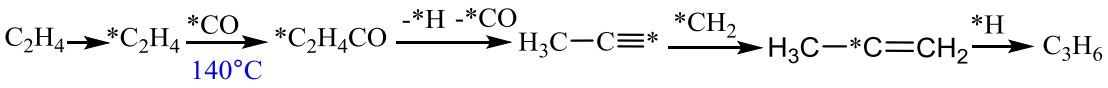

Scheme 8.10 The formation pathway of C_3H_6 via the ethylidyne intermediate

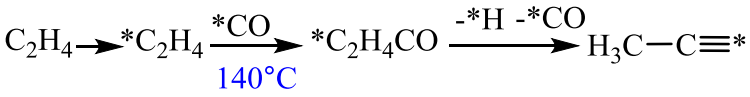

Scheme 8.11 The formation pathway of the ethylidyne intermediate

The temperature at which ethylidyne formation starts was considered to be lower than 210 °C in this reaction system because iso-C_4H_{10} and trans-2-butene - the formation of which can be explained through the mechanism based on ethylidyne as the intermediate - were detected from 210 °C and 220 °C, respectively. But what if ethylidyne can be formed at lower temperatures? Is it possible to explain the formation pathways of products at a lower temperature reasonably and without the considering the reaction barriers? Below 210 °C, the products are C_2H_5CHO, C_2H_6, C_3H_7OH and C_3H_6. Pathway 2 in Scheme 8.8 was the proposed formation pathway of C_2H_6 via the ethylidyne intermediate. Scheme 8.9 shows the formation pathway of C_3H_6 via the ethylidyne intermediate. It is still reasonable to suggest that the formation of C_2H_6 and C_3H_6 occurred via the ethylidyne intermediate, regardless of the reaction barriers. However, it is impossible to explain the formation of C_2H_5CHO and C_3H_7OH via the ethylidyne intermediate. The formation of C_2H_5CHO and C_3H_7OH needs $*C_2H_4$ and *CO to be kept coupled together until the reaction termination (Scheme 8.1 and 8.2), while the formation of ethylidyne (≡C-CH_3) needs *CO and *H to be eliminated from $*C_2H_4CO$. Therefore, the conclusion that can be drawn is that CO-induced formation of ethylidyne (≡C-CH_3) could not happen in this reaction system below 210 °C. Furthermore, the interaction between C_2H_4 and CO in our experiments revealed that, below 210 °C, the adsorbed $*C_2H_4$ induced CO dissociation and hydrogenation step-by-step to form C_2H_4CHO, C_3H_7OH and C_3H_6. Above 210 °C, CO induced the formation of ethylidyne (≡C-CH_3) from adsorbed $*C_2H_4$ to initiate ethene dimerization and more hydrocarbons.

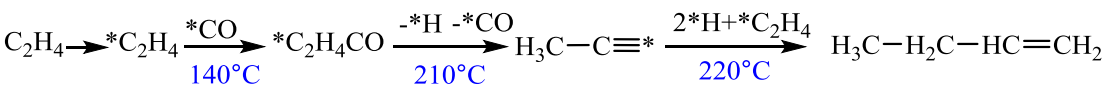

Scheme 8.12 The formation pathway of n-C_4H_8

The other products that started to form at 220 °C were C_3H_8, n-C_4H_8 and C6 hydrocarbon. It is obvious that C_3H_8 was produced by the hydrogenation of C_3H_6. The formation of n-C_4H_8 can be explained by ethylidyne (≡C-CH_3), as described in Scheme 8.12. With C6 hydrocarbon, it is difficult to identify the proper structure for each product by GC, as there are a lot of isomers among the C6 hydrocarbons. Therefore, it is difficult to propose a detailed formation pathway for C6 hydrocarbon; but, C_2H_4 oligomerization could be one of the possible formation pathways. Meanwhile, an intermediate *CH_2 produced by C_2H_4 hydrocracking should not be ignored, i.e. the monomer for FTS chain growth. So there is a possible FTS chain growth formation mechanism based on *CH_2 for all the hydrocarbons produced when the reaction temperature is above 210 °C, as the *CH_2 from C_2H_4 hydrocracking started at 210 °C. (See Scheme 8.5.)

C5 hydrocarbon started to form at 230 °C. Similar to the situation of C6 hydrocarbons, the detailed formation pathways of C5 were also not discussed here. The possible formation pathways of C5 are: coupling of C2 and C_3 species, coupling of C1 and C4 species, and/or FTS chain growth from *CH_2. At 240 °C, CH_3OH and n-C_4H_{10} started to form. (See Figure 8.1.) The formation pathway of CH_3OH has been mentioned above (Scheme 8.3). It is easy to explain the formation of n-C_4H_{10} by the hydrogenation of n-C_4H_8. At 250 °C, cis-2-butene, CO_2 and C_{7+} hydrocarbons started to form. The formation of cis-2-butene was explained in Scheme 8.7. C7+ hydrocarbons were formed through coupling of lower carbon species or FTS chain growth. CO_2 was formed via water gas shift reaction as shown in Scheme 8.13. At 270 °C and 290 °C, the products distribution remained the same with the distribution at 250 °C.

$$CO \longrightarrow *CO \xrightarrow[250°C]{H_2O} *CO_2+*H_2 \xrightarrow{250°C} CO_2+H_2$$

Scheme 8.13 The formation pathway of CO_2 via water gas shift reaction

8.3.2 Discussion

Based on the experimental results, the catalyst 0.5%Rh-20%Co/RGO (RCG) suppressed CO direct dissociation, which resulted in very low CH_4 and hydrocarbon production, especially at the lower

operating temperatures. Nevertheless, CO inversion was promoted by this catalyst, with the absorbed CO being reacted with the absorbed C_2H_4 to form oxygenates, even at a very low temperature of 140 °C.

Based on the results discussed above, the confirmed pathways and most probable pathways for the reaction of CO, C_2H_4 and H_2 at various temperatures from 140 °C to 250 °C were determined and are provided in Scheme 8.14.

8.3.2.1 Initiation of the reaction of CO/C_2H_4/CO by C-C coupling between CO and C_2H_4

The CO non-dissociation adsorption on the catalyst was confirmed by the results of the FTS reaction with syngas (CO:H_2 = 1:2) at 250 °C under 20 bar and a feed-gas flow rate = 60 ml/min. (See Chapter 4.) During FTS, the CO conversion was only 0.05%, which indicates that CO could not be activated on the catalyst, even at 250 °C by H_2. For C_2H_4, hydrogenation to C_2H_6 did not occur at 140 °C, which means that C_2H_4 could not be activated by H_2 at 140 °C. So, neither CO nor C_2H_4 could be activated directly by H_2 at 140 °C. However, after C-C bond coupling between CO and C_2H_4, the H atom was added to the carbon atom with both CO and C_2H_4 and formed C_2H_5CHO at 140 °C. Therefore, the coupling of CO and C_2H_4 (C_2H_4CO*) induced hydrogenation of the intermediate to form the C-H bond. It can be concluded that C-C coupling occurs prior to CO dissociation, and it could initiate the reaction of CO/C_2H_4/CO at a low temperature under the reaction system used in the experiments.

8.3.2.2 Different interactions between CO and C_2H_4 determined the reaction direction

It seems that the different intermediates produced by different interactions between C_2H_4 and CO at different temperatures determined different reaction directions. At 140 °C, the prior reaction is C-C coupling between CO and C_2H_4, which induced partial hydrogenation of C_2H_4CO* to form C_2H_5CHO, namely EH. Without C_2H_4, no reaction happened, even when the reaction temperature reached 250 °C. Figure 8.1 shows that C_2H_5CHO and C_2H_6 were detected at 140 °C, and then C_3H_7O at 180 °C. The apparent activation energy for the formation of C_2H_6, C_2H_5CHO and C_3H_7OH were calculated using the Arrhenius equation, and plotted as per Figure 8.2. Therefore, the order of difficulty of the formation of C_2H_6, C_2H_5CHO and C_3H_7OH is C_2H_5CHO <C_2H_6<C_3H_7OH. This means that the order of difficulty for the hydrogenation of *C_2H_4CO, C_2H_4 and C_2H_5CHO is *C_2H_4< C_2H_4<C_2H_5CHO.

With further dehydration of C_3H_7OH, C_3H_6 was produced at 190 °C, which marked the complete dissociation of CO. Without C_2H_4 co-feeding, it was difficult to ensure CO reacted with H_2 to form long chain hydrocarbons on a CO non-dissociation catalyst, even at 250 °C. Nevertheless, C_2H_4 could induce C-C coupling via the CO insertion mechanism; and the -C≡O band was dissociated step-by-step via EH, C_2H_5CHO hydrogenation to C_3H_7OH and C_3H_7OH dehydration to C_3H_6. However, the chain growth from CO itself to long chain hydrocarbons was not initiated at or below 190 °C.

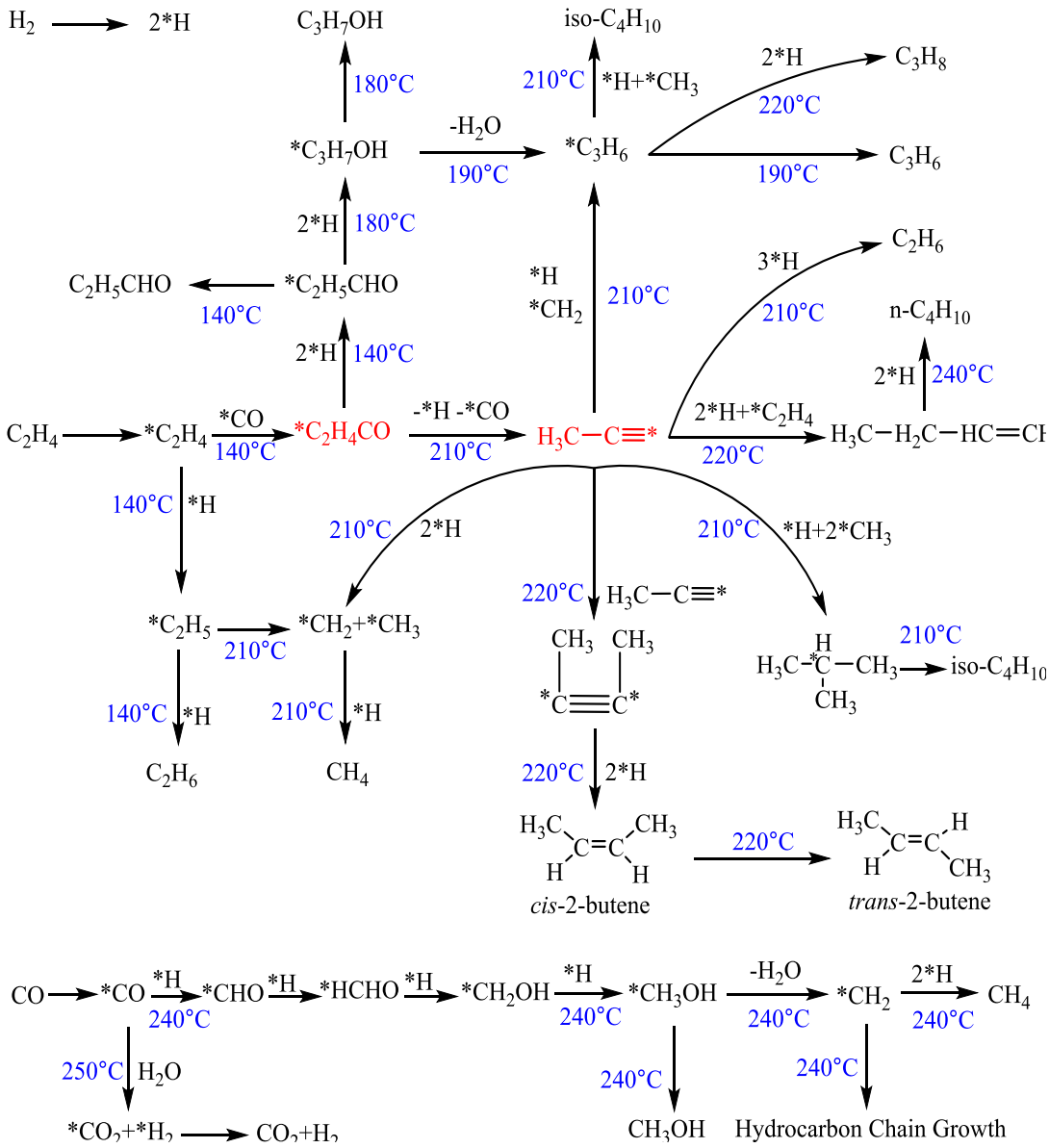

Scheme 8.14 Reaction pathways of CO/C_2H_4/CO at different temperatures

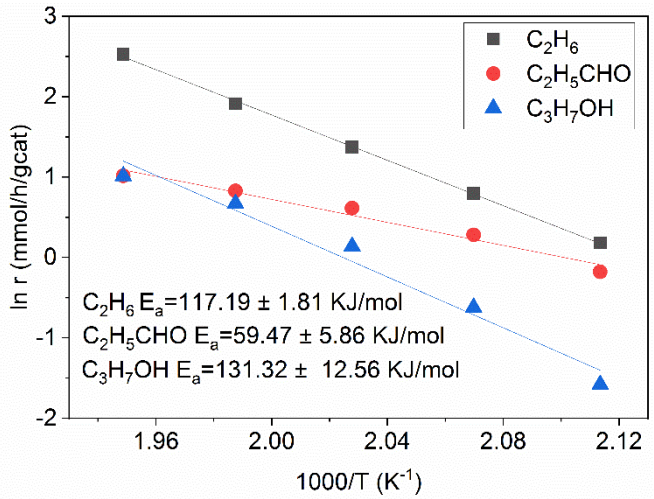

Figure 8.2 The apparent activation energy for the formation of C_2H_6, C_2H_5CHO and C_3H_7OH.

From 210 °C, the interaction between CO and C_2H_4 changed. At 210 °C, CO induced the formation of intermediate ethylidyne from C_2H_4 to initiate the formation of C4 hydrocarbon and CH_4 via C_2H_4 hydrocracking. Above 210 °C, the intermediate ethylidyne, boosted the reaction of CO/C_2H_4/CO and more reactions occurred, such as ethene dimerization, ethene oligomerization and FTS chain growth.

8.3.2.3 Role of hydrogenation activity of catalyst in the reaction of CO/C_2H_4/CO

It should be noticed that the olefin and paraffin with same carbon number were formed at different temperatures. C_3H_6 started to form at 190 °C while C_3H_8 started to form at 220 °C. n-C_4H_8 and trans-2-butene started to form at 220 °C while n-C_4H_{10} started to form at 240 °C. These phenomena are different compared with the conventional FTS, which the olefin and paraffin with same carbon number normally were produced at a same temperature.

8.4 Conclusion

The reactions of CO/C_2H_4/CO on a CO non-dissociation catalyst (0.5%Rh-20%Co/RGO) were performed under the reaction conditions: 0.5g catalyst; T= 140 °C ~ 290 °C; 2 MPa, total flow rate = 60 ml/min; feed-gas molar ratio: N_2 : CO : C_2H_4 : H_2 = 1 : 1 : 1 : 1; GHSV = 1000 h^{-1}. Different interactions between CO and C_2H_4 were observed at different temperatures. The interaction between CO and C_2H_4 below 210 °C could lead to complete dissociation of CO to form C_3H_6 via hydroformylation and dehydration. When increasing the temperature to 210 °C or above, an

intermediate ethylidyne was formed, which triggered FTS chain growth to higher hydrocarbons. Therefore, FTS can be initiated through an ethylidyne mechanism on a CO non-dissociation catalyst under a feed mixture of $CO/C_2H_4/CO$. The mechanisms and reaction pathways for EH and FTS were proposed. The findings support understanding the unknown mechanisms of EH under FTS conditions through an ethylidyne intermediate produced by ethene under CO induction.

References

[1] C.J.K. Weststrate, D. Sharma, D.G. Rodriguez, M.A. Gleeson, H.O.A. Fredriksson, J.W.H. Niemantsverdriet, Mechanistic insight into carbon-carbon bond formation on cobalt under simulated Fischer-Tropsch synthesis conditions, Nat. Commun. (2020). https://doi.org/10.1038/s41467-020-14613-5.

[2] M. Claeys, E. van Steen, Basic studies, Elsevier B.V., 2004. https://doi.org/10.1016/S0167-2991(04)80465-8.

[3] C.J.W.D. Sharma, D.G. Rodriguez, M.A. Gleeson, H.O.A. Fredriksson, J.W. Niemantsverdriet, Reactivity of $-C_3H_x$ adsorbates in presence of Co^- adsorbed CO and hydrogen: Testing Fischer–Tropsch chain growth mechanisms, Top. Catal. (2020). https://doi.org/10.1007/s11244-020-01306-y.

[4] M.M.G. R. A. van Santen, I. M. Ciobica, E. van Steen, Mechanistic issues in Fischer–Tropsch catalysis, 2011. https://doi.org/10.1016/B978-0-12-387772-7.00003-4.

[5] Y. Zhang, Y. Yao, J. Chang, X. Lu, X. Liu, D. Hildebrandt, Fischer–Tropsch synthesis with ethene co-feeding: Experimental evidence of the CO-insertion mechanism at low temperature, AIChE J. n/a (2020) e17029. https://doi.org/10.1002/aic.17029.

[6] O. Roelen, United States Patent Office 2327,066, (1943).

[7] F.E. Paulik, Recent developments in hydroformylation catalysis, Catal. Rev. 6 (1972) 49-.

https://doi.org/10.1080/01614947208078691.

[8] K. Wiese, D. Obst, Hydroformylation, Catal. Carbonylation React. 18 (2006) 1–33. https://doi.org/10.1007/3418_015.

[9] J. Yang, C. Ledesma Rodriguez, Y. Qi, H. Ma, A. Holmen, D. Chen, The effect of co-feeding ethene on Fischer-Tropsch synthesis to olefins over Co-based catalysts, Appl. Catal. A Gen. 598 (2020) 117564. https://doi.org/10.1016/j.apcata.2020.117564.

[10] L. Espinoza, Secondary reactions of primary products of the Fischer-Tropsch synthesis part 1. the role of ethene, J. Mol. Catal. 43 (1987) 237–247.

[11] R. Franke, D. Selent, A. Borner, Applied hydroformylation, Chem. Rev. 112 (2012) 5675–5732. https://doi.org/10.1021/cr3001803.

[12] W. Dong, J. Liu, H. Zhu, Y. Ding, Y. Pei, J. Liu, H. Du, M. Jiang, T. Liu, H. Su, W. Li, Co–Co 2 C and Co–Co 2 C/AC catalysts for hydroformylation of 1-hexene under low pressure: Experimental and theoretical studies, J. Phys. Chem. C. 118 (2014) 19114–19122. https://doi.org/10.1021/jp504215y.

[13] Y. Zhang, Y. Yao, J. Shen, J. Chang, J. Gorimbo, X. Liu, D. Hildebrandt, Effect of ethylene co-feeding in Fischer-Tropsch synthesis: A study of reaction equilibrium and competition, Fuel. 302 (2021) 121146. https://doi.org/10.1016/j.fuel.2021.121146.

[14] G.J. Hutchings, R.G. Copperthwaite, M. van der Riet, Low methane selectivity using Co/MnO catalysts for the Fischer-Tropsch reaction: Effect of increasing pressure and Co-feeding ethene, Top. Catal. 2 (1995) 163–172. https://doi.org/10.1007/BF01491964.

[15] E.S.P.B. V, J.H. Boelee, K. van der Wiele, Influence of reaction conditions on the effect of co-feeding ethene in the Fischer-Tropsch Synthesis on a fused-iron catalyst in the liquid phase, Appl. Catal. 53 (1989) 1–13.

[16] T. SUZUKI, Enhancement of propene formation by co-feeding ethene and synthesis gas on Co / SiO_2 Catalyst, Transaction of the Materials Research Society of Japan, 390 (2009) 387–390.

[17] R.R. Hudgins, P.L. Silveston, Effect of ethene addition during the Fischer- Tropsch reaction, Applied Catalysis, 62 (1990) 295–308.

[18] Y. Zhang, M. Tshwaku, Y. Yao, J. Chang, X. Lu, X. Liu, D. Hildebrandt, Reaction of ethylene over a typical Fischer-Tropsch synthesis Co/TiO2 catalyst, Eng. Reports. 2 (2020) e12232. https://doi.org/https://doi.org/10.1002/eng2.12232.

[19] Y. Zhang, Y. Yao, J. Chang, X. Lu, X. Liu, D. Hildebrandt, Fischer–Tropsch synthesis with ethene co-feeding: Experimental evidence of the CO-insertion mechanism at low temperature, AIChE J. 66 (2020) e17029. https://doi.org/https://doi.org/10.1002/aic.17029.

[20] Y. Zhang, Y. Yao, J. Chang, J. Gorimbo, X. Liu, D. Hildebrandt, The interaction of CO, H2 and ethylene over a typical cobalt-based Fischer-Tropsch synthesis catalyst, Appl. Catal. A Gen. 614 (2021) 118024. https://doi.org/https://doi.org/10.1016/j.apcata.2021.118024.

[21] A.I. McNab, A.J. McCue, D. Dionisi, J.A. Anderson, Combined quantitative FTIR and online GC study of Fischer-Tropsch synthesis involving co-fed ethylene, J. Catal. 362 (2018) 10–17. https://doi.org/10.1016/j.jcat.2018.03.026.

[22] C.J. Weststrate, J.W. Niemantsverdriet, CO as a promoting spectator species of CxHy conversions relevant for Fischer–Tropsch chain growth on cobalt: Evidence from temperature-programmed reaction and reflection absorption infrared spectroscopy, ACS Catal. 8 (2018) 10826–10835. https://doi.org/10.1021/acscatal.8b02743.

Chapter 9: Conclusions and Perspectives

Both heterogeneous ethene hydroformylation (EH) reaction and Fischer-Tropsch synthesis (FTS) reaction were studied over reduced graphene oxide (RGO) supported cobalt-based catalysts with and without rhodium (Co/RGO (CG) and Rh-Co/RGO (RCG)), and under different reaction conditions. This work provides a framework for investigating: the relationship between FTS and hydroformylation; the role of Co_2C and Co-Co_2C; the metal support interaction between cobalt species and RGO; and the mechanisms of FTS chain propagation and oxygenate formation.

9.1 Concluding Remarks

9.1.1 Catalysis of reduced graphene-supported cobalt catalysts

Metallic Co (Co^0) formed after H_2 reduction of a CG catalyst, while Co_2C was detected in the Rh promoted catalyst (RCG). These results indicate that, under Rh promotion, the carbon of Co_2C is provided by the RGO support. The characterization results showed that a multi-phase of Co-Co_2C formed for the CG catalyst under an atmosphere of syngas or syngas co-feeding with ethene. Moreover, this multi-phase of Co-Co_2C exhibited low Fischer-Tropsch (FT) activity with the main products being short chain hydrocarbons and oxygenates. However, a pure Co_2C phase was formed for the RCG catalyst (Rh promoted catalyst), and it was completely inactive for FTS. These results indicate that the existence of Rh promotes the formation of the Co_2C phase. Nevertheless, when exposing both the Co-Co_2C/RGO and Rh-Co_2C/RGO to a feed mixture of $CO/C_2H_4/H_2$, the C_3 oxygenates were produced with very high selectivity, especially with the Rh-Co2C/RGO catalyst, which indicated that Co_2C was highly active for EH. It was experimentally proved that Co_2C can suppress CO from attending the chain growth reaction, but promotes CO insertion to form aldehyde or alcohols.

9.1.2 Metal support interaction (MSI) of reduced graphene supported cobalt catalysts

The geometric morphologies and the reducibility of cobalt nanoparticles were different for the catalysts with and those without Rh promotion: (1) For the fresh catalyst after calcination, CoO nanorods was

present in Rh promoted catalyst (RGC), while only CoO nano-particles were formed in the catalyst without Rh promotion (CG).; (2) After H_2 activation, a higher reducibility was obtained for the catalyst promoted with Rh.; (3) After catalyst evaluation under a feed of $CO/C_2H_4/H_2$, pure Co_2C that grew to a large flat plane structure was formed in spent RCG, while a mixture of Co and CoO with smaller nanoparticles were present in spent CG. It was concluded that the addition of a small amount of Rh tunes the interaction between cobalt species and RGO, which enhances the catalytic performance of a reduced graphene-supported cobalt-based catalyst for EH. The results provided a powerful strategy for tuning the interaction between graphene and metals to enhance catalytic performance. A new heterogeneous EH process was also developed in this work, which shows potential for use in industry.

9.1.3 Optimization of conditions for EH on a Rh-Co/RGO catalyst

Rh-Co/RGO has good performance for EH. Its activity is affected by the operating conditions, such as pressure, temperature, space velocity and feed ratio. When increasing the total pressure from 0 to 1 MPa, C_3 oxygenates increased, while the C_2H_4 hydrogenation side reaction was suppressed. However, a further increase in pressure from 1MPa to 2 MPa, showed that the yield of C_3 oxygenates production was fairly constant. The highest selectivity of CO to C_3 oxygenates was obtained at 1 MPa with a selectivity of 83.24%. Although the effect of the GHSV on C_2H_4 hydrogenation was weak, it significantly affected the production of C_3 oxygenates, with GHSV= 960 h^{-1} being the optimal space velocity for EH.

The operating temperature affected the performance of hydroformylation reaction significantly. When increasing the temperature from 140 °C to 290 °C, the reaction rate of the C_3 oxygenates first increased, then reached a maximum and then decreased. Temperatures of 210 °C to 230 °C are the optimal region for EH.

Different ratios of the feed mixture $CO/H_2/C_2H_4$ were used for EH. The experimental results showed that the partial pressure of H_2 and CO play a significant role in the production of C_3 oxygenates, while the effect of the partial pressure of C_2H_4 was not that obvious. A lower H_2 partial pressure and a higher CO partial pressure may contribute to higher selectivity of the C_3 oxygenates.

9.1.4 Insight into the C-C and C-H formation mechanism on cobalt carbide

As stated above, the RCG catalyst (rhodium promoted cobalt catalyst supported RGO) with a Co_2C phase suppressed the FT chain growth reaction and promoted the EH reaction. By tracing the product spectrum from GC at different reaction temperatures, the formation sequence of the products were determined, which reflects the reaction behavior of CO and C_2H_4 and directs the reaction pathways. When increasing the temperature from 140 °C to 290 °C, the products identified at different temperature levels were: C_2H_5CHO at T ≥140 °C; C_2H_6 at T ≥140 °C; C_3H_7OH at T ≥180 °C; C_3H_6 at T ≥190 °C; CH_4 and iso-C_4H_{10} at T ≥210 °C; C_3H_8, n-C_4H_8 and tran-2-C_4H_8; C_6 at T ≥220 °C; C_5 at T ≥230 °C; CH_3OH and n-C_4H_{10} at T ≥240 °C; cis-2-C_4H_8, C_7; CO_2 at T ≥250 °C.

At a low reaction temperature (140-190 °C), C_2H_4 assisted the reaction of CO and C_2H_4 to form an intermediate of *C_2H_4CO with C-C band coupling, which could then use the step-by-step hydrogenation path to form oxygenates and hydrocarbons. When increasing the temperature from 210 to 290 °C, the formation of the ethylidyne (≡C-CH_3) intermediate that is induced by adsorbed CO could explain the formation of the tran-2-C_4H_8 and cis-2-C_4H_8 hydrocarbon products. In addition, the formation of ethylidyne triggered the chain growth reaction to produce longer hydrocarbon products.

9.2 Perspectives

Co^0 is commonly used for FT chain growth reaction to produce long chain olefin and paraffins. Co_2C is very active for olefin hydroformylation, and it can be used for the OXO synthesis process. Based on the research that was done, it was shown that different atmosphere treatments (such as H_2, syngas or ethene cofeeding with syngas) can change the nature of the active sites, which tune the catalytic performance of the catalysts. The multi-phase of Co-Co_2C can be synthesised on the support of the catalyst under syngas or ethene co-feeding syngas treatment, which ensures the active phase (Co^0) for chain growth reaction and the active phase of Co_2C for olefin hydroformylation. The interphase of Co-Co_2C has the potential to synergistically catalyze the production of long chain oxygenates from syngas, by configuring the FT reaction and hydroformylation reaction. Therefore, investigation of the multi-phase of Co-Co_2C for one-step long chain oxygenate production is highly recommended.

A small amount of Rh (0.5%) can result in significant variations in the geometry of the cobalt nanoparticles and change the interaction between cobalt and RGO. Consequently, it promotes the formation of Co_2C. Rh-Co_2C/RGO derived from RCG is active for heterogeneous EH and offers potential for use in industrial hydroformylation processes. More research work needs to be done to investigate the structure-activity relationship and the stability of the catalyst.